NASA
CR
2901
c.1
v.1

TECH LIBRARY KAFB, NM
0061737

LOAN COPY: RETUR
AFWL TECHNICAL L
KIRTLAND AFB, N. ....

NASA Contractor Report 2900

Computation of Unsteady Transonic Flows Through Rotating and Stationary Cascades

I - Method of Analysis

John I. Erdos and Edgar Alzner

CONTRACT NAS3-16807
DECEMBER 1977

25 APR 1978
Technical Library
AF Weapons Laboratory

NASA

TECH LIBRARY KAFB, NM

0061737

NASA Contractor Report 2900

Computation of Unsteady Transonic Flows Through Rotating and Stationary Cascades

I - Method of Analysis

John I. Erdos and Edgar Alzner
Advanced Technology Laboratories, Inc.
Westbury, New York

Prepared for
Lewis Research Center
under Contract NAS3-16807

NASA
National Aeronautics
and Space Administration

Scientific and Technical
Information Office

1977

TABLE OF CONTENTS

	Page
INTRODUCTION	1
INVISCID FLOW ANALYSIS	4
FUNDAMENTAL SYSTEM OF EQUATIONS	4
ABSOLUTE STREAM SURFACE EQUATIONS	6
RELATIVE STREAM SURFACE EQUATIONS	8
DESCRIPTION OF THE COMPUTATIONAL DOMAIN	10
TRANSFORMATION OF VARIABLES TO COMPUTATIONAL DOMAINS	12
INTERIOR POINT SOLUTION ALGORITHM	16
INLET AND DISCHARGE BOUNDARY CONDITIONS AND BOUNDARY POINT SOLUTION ALGORITHM	21
BLADE SURFACE AND SLIPSTREAM BOUNDARY CONDITIONS AND SOLUTION ALGORITHM	33
PERIODICITY CONDITION	46
INITIAL CONDITIONS	51
BOUNDARY LAYER AND WAKE ANALYSIS	54
MOTIVATION AND APPROACH	54
QUASI-STEADY APPROXIMATIONS	55
BLADE BOUNDARY LAYER DISPLACEMENT THICKNESS AND SHEAR STRESS	56
BLADE WAKES	61
GOVERNING EQUATIONS AND BOUNDARY CONDITIONS	62
ANALYSIS OF INDEPENDENT WAKES	65
ANALYSIS OF MERGED WAKES	72
EDDY VISCOSITY LAW AND VELOCITY PROFILE REPRESENTATIONS	74
COMPOSITE SOLUTION	77

TABLE OF CONTENTS (Continued)

	Page
RESULTS	79
SUMMARY AND RECOMMENDATIONS	91
APPENDIX - TREATMENT OF VIRTUAL BOUNDARIES	96
PERIODIC BOUNDARY CONDITIONS	96
HORIZONTAL BOUNDARIES	112
ENTRANCE AND EXIT BOUNDARIES	115
REFERENCES	119

LIST OF FIGURES

		Page
FIG. 1	SCHEMATIC OF BLADE ROW INTERSECTION WITH A STREAM SURFACE, AND COORDINATE SYSTEMS	3
FIG. 2	DETAIL OF STREAM SURFACE COORDINATE SYSTEM WITH FINITE THICKNESS STREAM SHEET	7
FIG. 3	BLADE-TO-BLADE COORDINATE SYSTEM AND GRID NETWORK	11
FIG. 4	SCHEMATIC REPRESENTATION OF PHYSICAL AND COMPUTATIONAL DOMAINS	14
FIG. 5	GRID ROW ORDERING IN VICINITY OF BLADES AND SLIPSTREAMS	18
FIG. 6	CHARACTERISTIC LINES AND GRID POINTS AT INLET AND DISCHARGE STATIONS	23
FIG. 7	CHARACTERISTIC CONSTRUCTION AT A SLIPSTREAM POINT	35
FIG. 8	COMPARISON OF BLADE AND SLIPSTREAM CHARACTERISTIC SYSTEM	41
FIG. 9	SCHEMATIC OF LEADING AND TRAILING EDGE CONFIGURATIONS	43
FIG. 10a	ILLUSTRATION OF CYCLIC ALGORITHM FOR STAGE WITH EQUAL NUMBER OF BLADES IN STATOR AND ROTOR (N_1=3, N_2=3)	48
FIG. 10b	ILLUSTRATION OF CYCLIC ALGORITHM FOR STAGE WITH UNEQUAL NUMBER OF BLADES IN STATOR AND ROTOR (N_1=3, N_2=4)	50
FIG. 11	SCHEMATIC OF WAKE COORDINATE SYSTEM	63
FIG. 12	NON-DIMENSIONAL TURBULENT WAKE VELOCITY PROFILE	76
FIG. 13	STATOR BLADE TIP SECTION GEOMETRY AND COMPARISON OF SURFACE MACH NUMBER DISTRIBUTIONS	81
FIG. 14a	CALCULATED STATIC PRESSURE CONTOURS AT ROTOR TIP	83
FIG. 14b	MEASURED STATIC PRESSURE CONTOURS AT ROTOR TIP (READING 137 FROM REFERENCE 27)	84
FIG. 15	PRESSURE DISTRIBUTIONS ON ROTOR BLADE TIP SURFACES (READING 137)	85

LIST OF FIGURES (Continued)

		Page
FIG. 16	COMPUTED ISOBARS FOR READING 128 OF REFERENCE (28) M_∞=1.6 AND PRESSURE RATIO = 1.5	86
FIG. 17	COMPUTED ISOBARS FOR READING 126 of REFERENCE (28) M_∞=1.6 AND PRESSURE RATIO = 1.7	88
FIG. 18	COMPUTED ISOBARS FOR READING 106 OF REFERENCE (28) M_∞=1.4 AND PRESSURE RATIO = 1.5	89
FIG. 19	STATOR MID-CHORD PRESSURE DIFFERENTIAL DURING QUARTER REVOLUTION OF ROTOR	92
FIG. 20	PRESSURE VARIATIONS AT ROTOR MID-CHORD AND AT INLET DURING QUARTER REVOLUTION	93

LIST OF SYMBOLS

Note: Symbols denoting dimensional variables are accompanied by the appropriate units in the International System (SI). All other variables are non-dimensional. The terms "relative" and "absolute" distinguish variables defined in a frame of reference rotating with a moving blade row from variables in a non-rotating frame.

English

a	speed of sound $(\gamma p/\rho)^{\frac{1}{2}}$; m/sec
A	displacement thickness gradient coefficient
$A,B,C,..,Q$	position of characteristic and stream path locations (see subscripts)
b	stream surface thickness; m
B	displacement thickness gradient exponent
c	chord length; m
C_v	specific heat at constant volume; N•m/kg•K
e,f,g,h	non-dimensional arrays containing the dependent variables ρ, u, v and E (defined by Equations 49, 50, 51 and 52)
e	static internal energy per unit mass; N•m/kg
E	absolute total internal energy per unit mass; N•m/kg
E'	relative total internal energy per unit mass (see Equation 26); N•m/kg
f	Falkner-Skan equation dependent variable
h	static enthalpy per unit mass; N•m/kg
H	absolute total enthalpy per unit mass; N•m/kg
H'	relative total enthalpy per unit mass (see Equation 25); N•m/kg
JS	grid column corresponding to $\sigma = 1$
k	a constant, defined by the context of its usage
KS	grid row corresponding to $\nu = 1$
L	a reference length (axial chord length is used in the computer program); m
ℓ_o	wake width parameter
m	meridional distance; m
m	pressure gradient parameter
n	normal distance; m
n	turbulent boundary layer profile exponent
n'	modified turbulent boundary layer profile exponent

English

N_i	number of blades in i^{th} blade row
p	static pressure; N/m^2
q	magnitude of the velocity vector; m/sec
r	radius; m
R	radius of curvature of slipstream; m
R	gas constant; N•m/kg•K
R	Reynolds number
R_T	Townsend's turbulent Reynolds number
s	distance along stream path; m
S	entropy per unit mass; N•m/kg•K
t	time; sec
T	static temperature; K
u	meridional velocity component; m/sec
v	relative circumferential velocity component; m/sec
$\vec{V}$	absolute velocity vector; m/sec
V_m	meridional velocity component; m/sec
V_θ	absolute circumferential velocity component; m/sec
W	Cole's wake function
x	meridional distance; m
y	relative circumferential distance; m
z	axial distance; m

Greek

α	non-dimensional circumferential distance variable used to form composite solution
β	pressure gradient parameter in Falkner-Skan equation
γ	ratio of specific heats
δ	boundary layer thickness; m
δ^*	displacement thickness; m
ε	kinematic viscosity coefficient; N•m•sec/kg
ζ	normal component of vorticity vector; sec^{-1}
η	non-dimensional distance normal to a particular surface point
θ	absolute circumferential angle; radians

Greek

θ	momentum thickness; m
μ	viscosity coefficient; $N \cdot sec/m^2$
ν	normalized circumferential coordinate (either absolute or relative)
ξ	non-dimensional distance along a tangent to a particular surface point
π	3.14159 ...
ρ	static density; kg/m^3
σ	normalized axial coordinate
τ	non-dimensional time
τ	shear stress; N/m^2
ϕ	slipstream angle, measured on stream surface with respect to meridional coordinate; radians
ϕ	stream path angle at leading edge; radians
$\vec{\omega}$	vorticity vector; sec^{-1}
Ω	angular velocity of rotating blade row; radians/sec

Subscripts

a,b,c,d, e,f,o,q	evaluated at points A,B,C,D,E,F,O,Q in Figures (6) and (7)
e	evaluated at blade surface
f	evaluated at outer edge (front) of wake
i	index identifying computational domain
i	time count index
j	index identifying grid columns
k	index identifying grid rows
LE	leading edge
ℓ	lower boundary of blade-to-blade passage (i.e., the upper surface of the lower blade of a blade-to-blade passage)
m	minimum value
n	value at next time step
o	reference state
o	evaluated at a grid point under consideration

Subscripts

R	rotor
S	stator
TE	trailing edge
u	upper boundary of blade-to-blade passage (i.e., the lower surface of the upper blade of a blade-to-blade passage)
1	first blade row
2	second blade row

Superscripts

p	provisional or predictor value
-	surface-oriented coordinate system (e.g., $\bar{u}$, $\bar{v}$ are velocity components tangent and normal to the blade or slipstream surface, and $\bar{x}$, $\bar{y}$ are the corresponding coordinates)
$'$	first derivative
$''$	second derivative
$'''$	third derivative

INTRODUCTION

The flow field within advanced axial flow turbomachinery for aircraft propulsion systems, specifically high bypass ratio turbofan engines, is characterized by the presence of mixed subsonic, transonic and/or supersonic regions, multiple shock waves, shock-boundary layer interactions, and significant effects of three-dimensionality and unsteadiness of the flow. These aspects of the flow field are not easily accommodated in the conventional analytical and numerical methods available for application to turbomachinery, and the design and analysis of advanced systems has been correspondingly constrained. A fairly recent review of methods for steady cascade analysis (i.e., two-dimensional compressible flow) is presented in Reference (1). In the area of transonic and mixed subsonic-supersonic flows, the most promising approaches appear to be the relaxation method for solution of the transonic small perturbation equation developed in Reference (2) and finite-difference solution of the complete system of equations for an inviscid compressible flow, as applied to a cascade in Reference (3), for example. A steady three-dimensional transonic solution for a blade row obtained by the finite-difference method is presented in Reference (4), and a corresponding solution for a wing using the relaxation method is presented in Reference (5). Analyses of unsteady flows in turbomachinery have been limited to solutions of the small disturbance equations, usually with a view toward description of the acoustic output of turbomachinery; cf. References (6), (7) and (8). Extension of the relaxation method to solution of the transonic small disturbance equation for an oscillating airfoil is presented in Reference (9). Thus, while important advances have been made in the last few years, a considerable amount of work remains to attain a comprehensive predictive capability in the subject problem area.

The present study has been directed toward development of a numerical method of solution of the complete unsteady equations of motion for a compressible, two-dimensional flow through a blade row (either rotor or stator) or a stage (both rotor and stator) of a compressor or fan. The objective is attainment of a steady solution for a single rotor or stator blade row or a periodic solution for an interacting pair of blade rows in a stage. Either case may include mixed subsonic, transonic and/or supersonic flow containing embedded shock waves. The initial effort is described in Reference (10).

The analysis is formulated with respect to a blade-to-blade stream surface, as depicted in Figure (1) for one passage of a blade row. The inlet and discharge boundary conditions are applied at axial stations some distance upstream and downstream of the blade rows. The selected boundary conditions assume subsonic axial velocity at both stations, but admit either choked or unchoked operation of the blade row or stage. In the case of a single blade row, or the equivalent infinite cascade on a blade-to-blade stream surface, it is immediately evident that the steady solution must possess a periodicity in the circumferential direction with a fundamental period of $2\pi/N_1$, where N_1 is the number of blades in the row. (It is implicit that the inlet and discharge boundary conditions also admit this periodicity condition.) If the blade row is rotating these considerations also pertain in the rotating frame of reference. Thus the computational domain need only encompass that fraction of the flow annulus containing the flow through a single blade-to-blade passage. The locations of the boundaries of the blade-to-blade passages may be defined arbitrarily so long as their spacing corresponds to the blade pitch. Downstream of the blade row the blade slipstreams represent natural boundaries of the blade-to-blade passages, since their spacing is identically the blade pitch, and certain components of the solution may be discontinuous across the slipstreams. Upstream of the blade row the boundaries have been conveniently defined as projections of the mean camber lines.

In the case of a stage consisting of a rotating blade row and a stationary blade row, a set of blade-to-blade passages may be defined for each blade row in accord with the above considerations, but the noted circumferential periodicity condition will not apply. As has been established from considerations of the acoustic problem, cf. Reference (11), the flow pattern will rotate with an angular velocity of $N_R\Omega/(N_S-N_R)$ and have a circumferential period of $2\pi/(N_S-N_R)$. Only in the limiting case of $N_R=N_S$, which is usually avoided in practice, will identical solutions occur in each blade-to-blade passage at any instant. In the typical stage ($N_S>N_R$) the flow pattern will rotate in the opposite direction of the rotor. The solution in any particular passage at one instant can, therefore, be related to that in another passage at an earlier time. This phase lag forms the basis of a cyclic procedure developed herein for relating the conditions along the boundaries of the computational domain (which is composed of a set of blade-to-blade passages for the two blade rows)

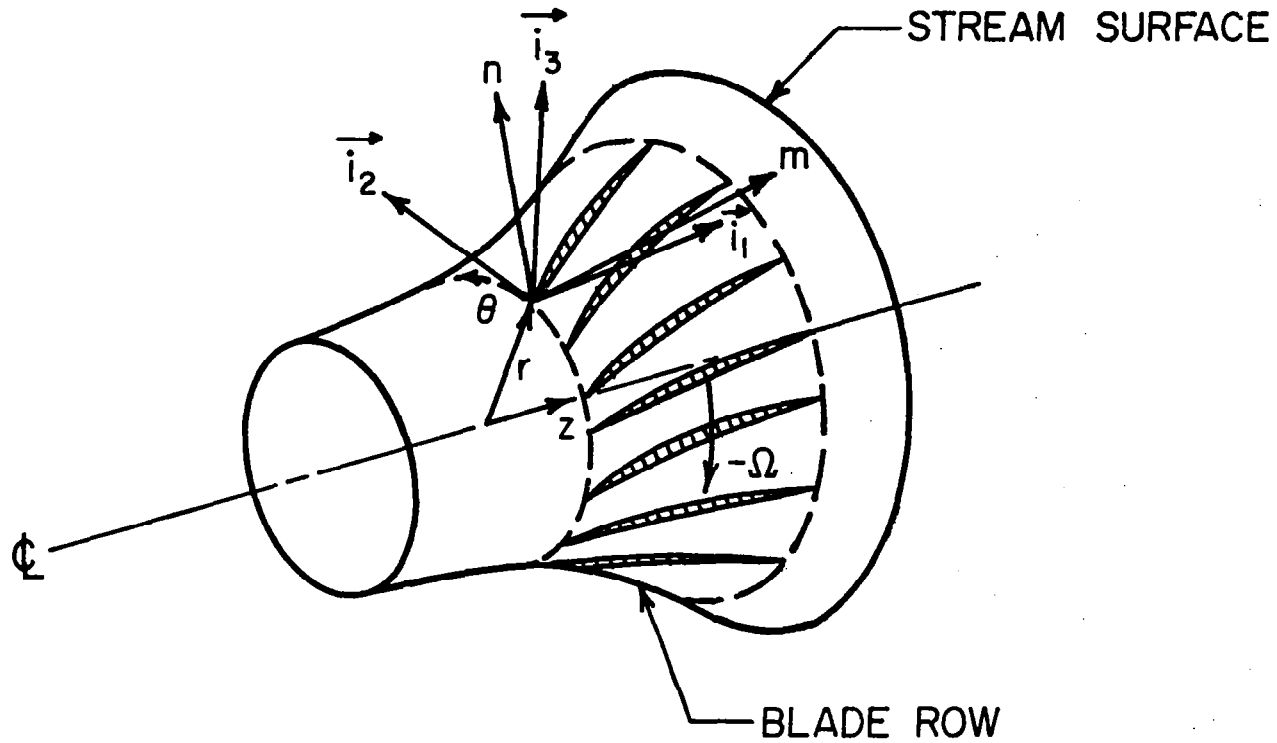

FIGURE I. SCHEMATIC OF BLADE ROW INTERSECTION WITH A STREAM SURFACE, AND COORDINATE SYSTEMS

to the solution within the domain at an earlier time. The cyclic procedure will be described in detail in a following section.

The total pressure losses due to boundary layers on the blades will be carried in the wakes of the blades. Thus, a significant contribution to the unsteady aerodynamic interaction between blade rows and resulting acoustic signals may be attributable to passage of one row through the viscous wakes of the other row. Accordingly, an approximate representation of the boundary layers on the blade surfaces and the blade wakes is also incorporated in the present model. The considered viscous effects include reduction of the blade-to-blade passage area due to the boundary layer displacement thickness and turbulent diffusion of the corresponding momentum defect (i.e., total pressure loss) in the wake.

INVISCID FLOW ANALYSIS

Fundamental System of Equations

The basic system of equations from which the present flow representation derives consists of the statements of conservation of mass;

$$\frac{\partial \rho}{\partial t} + \nabla \cdot \rho \vec{V} = 0 \tag{1}$$

conservation of momentum;

$$\frac{D\vec{V}}{Dt} + \frac{\nabla p}{\rho} = 0 \tag{2}$$

and conservation of energy;

$$\frac{De}{Dt} + p \frac{D}{Dt}\left(\frac{1}{\rho}\right) = 0 \tag{3}$$

where:

$$\frac{D}{Dt} = \frac{\partial}{\partial t} + \vec{V} \cdot \nabla \tag{4}$$

Assumption of an inviscid gas is implied by the absence of shear stress and heat conduction terms in Equations (2) and (3). In addition, a thermally and calorically perfect gas is assumed, for which:

$$p = \rho RT \tag{5}$$

$$e = \frac{p}{(\gamma-1)\rho} \tag{6}$$

The energy equation can be stated in a somewhat more convenient form through combination of Equations (1), (2) and (3);

$$\frac{\partial \rho E}{\partial t} + \nabla \cdot \rho \vec{V} H = 0 \tag{7}$$

where:

$$E = e + \frac{1}{2} V^2 \tag{8}$$

$$H = h + \frac{1}{2} V^2 \tag{9}$$

$$h = e + p/\rho \tag{10}$$

Furthermore, Equation (3) can also be written as:

$$\frac{DS}{Dt} = 0 \tag{11}$$

where:

$$p = k\rho^{\gamma} \exp(S/C_v) \tag{12}$$

An important distinction between Equations (7) and (3) or (11) should, however, be recognized. Equation (7) is in divergency or "conservation law" form, whereas Equations (3) and (11) are in a non-conservative form. The divergency or "conservation law" form of the equation may be applied across a shock wave, *but the non-conservative form can not.*

The only essential simplifications to this system of equations which are introduced in the following development of the flow model are a reduction in spatial dimensions of the problem from the general three-dimensional form used above to a particular two-dimensional form, and use of small disturbance approximations in the acoustic far-field of the machine. Derivation of the two-dimensional system is outlined below; discussion of the acoustic solution is presented in Volume III.

Absolute Stream Surface Equations

Consider a flow annulus as sketched in Figure (2). The curvilinear distance along the intersection of the mid-line of the annulus with a meridional plane is denoted by m, termed the meridional distance. The distance normal to the mid-line in a meridional plane is denoted by n. The circumferential coordinate θ is considered positive in the counter-clockwise direction when viewed down the positive z axis. The thickness of the annulus b is assumed to be small compared to the radius r; hence the n component of the velocity vector and all variations in the n direction are neglected. Accordingly, the annulus is termed a stream surface. Transformation of a system of equations of the above form to the considered two-dimensional coordinate system is outlined in Reference (12). Application of the same procedures to Equations (1), (2) and (7) yields:

$$\frac{\partial \rho}{\partial t} + \frac{\partial \rho V_m}{\partial m} + \frac{1}{r}\frac{\partial \rho V_\theta}{\partial \theta} + \frac{\rho V_m}{rb}\frac{drb}{dm} = 0 \tag{13}$$

$$\frac{\partial V_m}{\partial t} + V_m \frac{\partial V_m}{\partial m} + \frac{V_\theta}{r}\frac{\partial V_m}{\partial \theta} + \frac{1}{\rho}\frac{\partial p}{\partial m} = \frac{V_\theta^2}{r}\frac{dr}{dm} \tag{14}$$

$$\frac{\partial V_\theta}{\partial t} + V_m \frac{\partial V_\theta}{\partial m} + \frac{V_\theta}{r}\frac{\partial V_\theta}{\partial \theta} + \frac{1}{\rho r}\frac{\partial p}{\partial \theta} = -\frac{V_m V_\theta}{r}\frac{dr}{dm} \tag{15}$$

$$\frac{\partial \rho E}{\partial t} + \frac{\partial}{\partial m}(\rho V_m H) + \frac{1}{r}\frac{\partial}{\partial \theta}(\rho V_\theta H) + \frac{\rho V_m H}{rb}\frac{drb}{dm} = 0 \tag{16}$$

Equation (11) transforms to:

$$\frac{\partial S}{\partial t} + V_m \frac{\partial S}{\partial m} + \frac{V_\theta}{r}\frac{\partial S}{\partial \theta} = 0 \tag{17}$$

Equations (13) and (16) are in conservation form. Equations (14) and (15) can also be cast in this form by multiplying them by ρ and substituting Equation (13):

$$\frac{\partial \rho V_m}{\partial t} + \frac{\partial}{\partial m}(\rho V_m^2 + p) + \frac{1}{r}\frac{\partial}{\partial \theta}(\rho V_m V_\theta) + \frac{\rho V_m^2}{rb}\frac{drb}{dm} = \rho\frac{V_\theta^2}{r}\frac{dr}{dm} \tag{18}$$

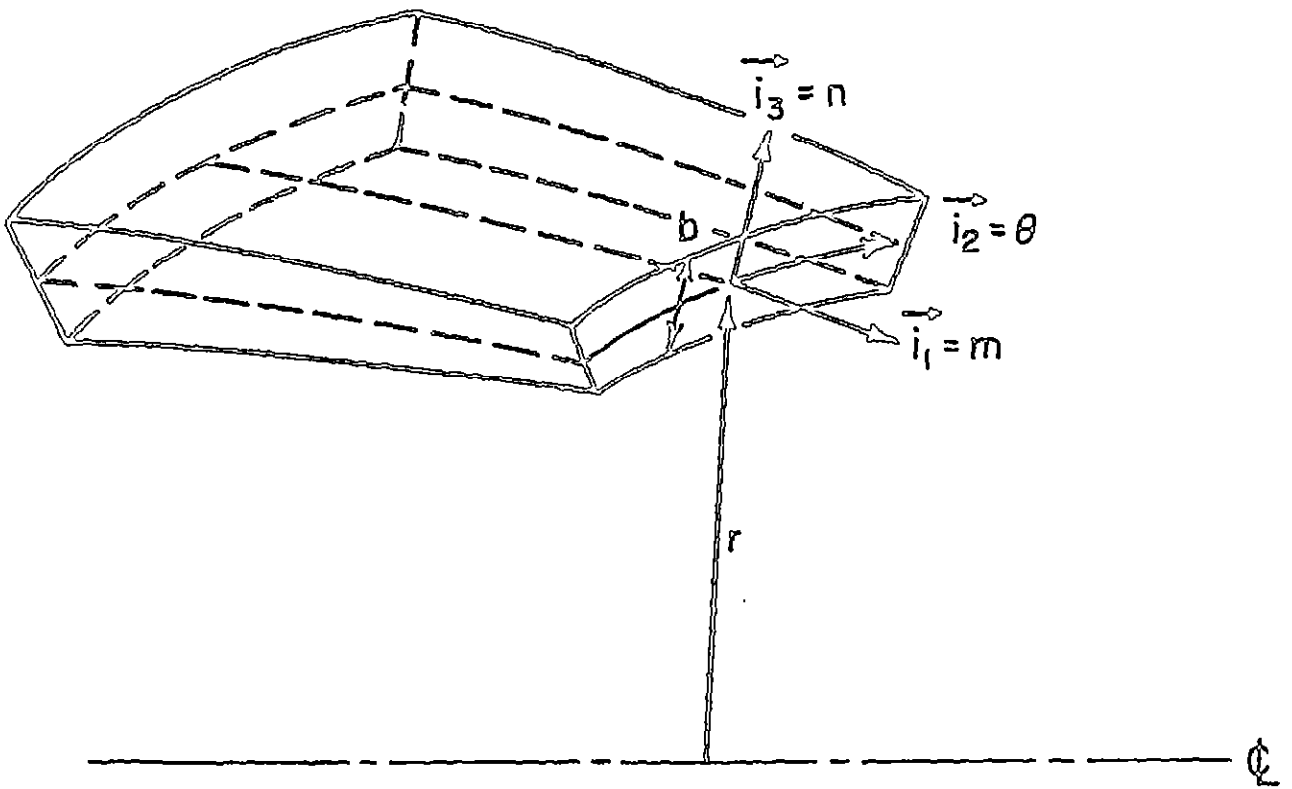

FIGURE 2. DETAIL OF STREAM SURFACE COORDINATE SYSTEM WITH FINITE THICKNESS STREAM SHEET

$$\frac{\partial \rho V_\theta}{\partial t} + \frac{\partial}{\partial m}(\rho V_m V_\theta) + \frac{1}{r}\frac{\partial}{\partial \theta}(\rho V_\theta^2 + p) + \frac{\rho V_m V_\theta}{rb}\frac{drb}{dm} = -\rho \frac{V_m V_\theta}{r}\frac{dr}{dm} \tag{19}$$

Thus, the statements of conservation of mass, momentum and energy given by Equations (13), (18), (19) and (16) constitute the conservative form of the governing system of equations, and Equations (13), (14), (15) and (17) represent the non-conservative form of the same system of equations. The conservative form will be used in the interior of the computational domain, whereas the non-conservative form will prove to be more convenient to employ at the boundaries.

Relative Stream Surface Equations

In the analysis of the flow through a rotating blade row it is advantageous to express the governing equations in a relative coordinate system which rotates with the blades. Therefore, the following additional coordinate transformation is introduced:

$$t = t \tag{20}$$

$$x = m \tag{21}$$

$$y = r\,(\theta - \Omega t) \text{ at } x=\text{constant} \tag{22}$$

and the velocity components in the x,y,t system are correspondingly defined:

$$u = V_m \tag{23}$$

$$v = V_\theta - \Omega r \tag{24}$$

A relative total enthalpy* and relative total energy are defined as:

$$H' = H - \Omega r V_\theta \tag{25}$$

---

*Note that the "relative total enthalpy" defined herein is sometimes referred to as "rothalpy" since it is <u>not</u> the total enthalpy which would be measured in the rotating frame of reference. However, it is a quantity which is conserved along streamlines in a steady rotating flow, and in this respect it is analogous to the conventional total enthalpy in an absolute frame.

$$E' = H' - p/\rho \tag{26}$$

The following system of equations, expressed in both conservative and non-conservative forms is thereby obtained:

Continuity

$$\frac{\partial \rho}{\partial t} + \frac{\partial \rho u}{\partial x} + \frac{\partial \rho v}{\partial y} = - \frac{\rho u}{rb} \frac{drb}{dx} \tag{27}$$

Streamwise Momentum

$$\frac{\partial \rho u}{\partial t} + \frac{\partial (\rho u^2 + p)}{\partial x} + \frac{\partial \rho u v}{\partial y} = - \frac{\rho u^2}{rb} \frac{drb}{dx} + \rho (v + \Omega r)^2 \frac{1}{r} \frac{dr}{dx} \tag{28a}$$

or,

$$\frac{\partial u}{\partial t} + u \frac{\partial u}{\partial x} + v \frac{\partial u}{\partial y} = - \frac{1}{\rho} \frac{\partial p}{\partial x} + (v + \Omega r)^2 \frac{1}{r} \frac{dr}{dx} \tag{28b}$$

Circumferential (Angular) Momentum

$$\frac{\partial \rho v}{\partial t} + \frac{\partial \rho u v}{\partial x} + \frac{\partial (\rho v^2 + p)}{\partial y} = - \frac{\rho u v}{rb} \frac{drb}{dx} - \rho u (v + 2\Omega r) \frac{1}{r} \frac{dr}{dx} \tag{29a}$$

or,

$$\frac{\partial v}{\partial t} + u \frac{\partial v}{\partial x} + v \frac{\partial v}{\partial y} = - \frac{1}{\rho} \frac{\partial p}{\partial y} - u (v + 2\Omega r) \frac{1}{r} \frac{dr}{dx} \tag{29b}$$

Energy

$$\frac{\partial \rho E'}{\partial t} + \frac{\partial \rho u H'}{\partial x} + \frac{\partial \rho v H'}{\partial y} = - \frac{\rho u H'}{rb} \frac{drb}{dx} \tag{30a}$$

or,

$$\frac{\partial S}{\partial t} + u \frac{\partial S}{\partial x} + v \frac{\partial S}{\partial y} = 0 \tag{30b}$$

It is pointed out parenthetically that the above system of equations can be applied in the relative (rotating) frame as stated, or in an absolute (stationary) frame by setting $\Omega=0$ and dropping the prime superscript on H and E. In addition, the standard two-dimensional equations of motion are recovered

when r and t are constant.

Solution of the above system of equations within the blade rows and in the near-field is therefore carried out numerically. In this connection it is necessary to define the selected computational domain, the boundary conditions pertaining thereto, the solution algorithm, and the initial conditions.

Description of the Computational Domain

As shown in Figure (3), the region in which the computation is carried out consists of up to seven (7) domains, which contain the two blade rows and segments of the stream surface extending upstream and downstream of the rows. However, it is not necessary to include both blade rows or all seven domains in every case. Although the conventional configuration consisting of a rotor followed by a stator is depicted in this figure, either row can be selected as the rotating cascade.* It is assumed in the formulation that the second row always has an equal or greater number of blades compared to the first row, this conforms to standard compressor design procedure. The frame of reference of domains 1 through 4 is attached to the first blade row and that of domains 5 through 7 is attached to the second row. The solution in each domain is correspondingly carried out in a relative or absolute frame of reference.

As indicated in Figure (3), the lateral extent of the computational domains encompasses a single blade-to-blade passage. The lateral boundaries of domains 1 and 2 are straight line projections of the mean camber line at the leading edge of the first blade row. The lateral boundaries of domains 3 and 5 are the blade surfaces, $f_u(m)$ and $f_\ell(m)$.**

---

*A restriction on the relative motion of the two blade rows, namely $\Omega_1 - \Omega_2 = 0$, applies in the computer code (see Volume 2). However, this restriction is easily circumvented by reversing the angular coordinates of the blades, i.e., $\theta \to -\theta$.

**Note that f_ℓ denotes the upper boundary of the computational domain which includes within it the lower surface of the blade. Similarly, f_u refers to the lower boundary of the domain, which includes the upper blade surface.

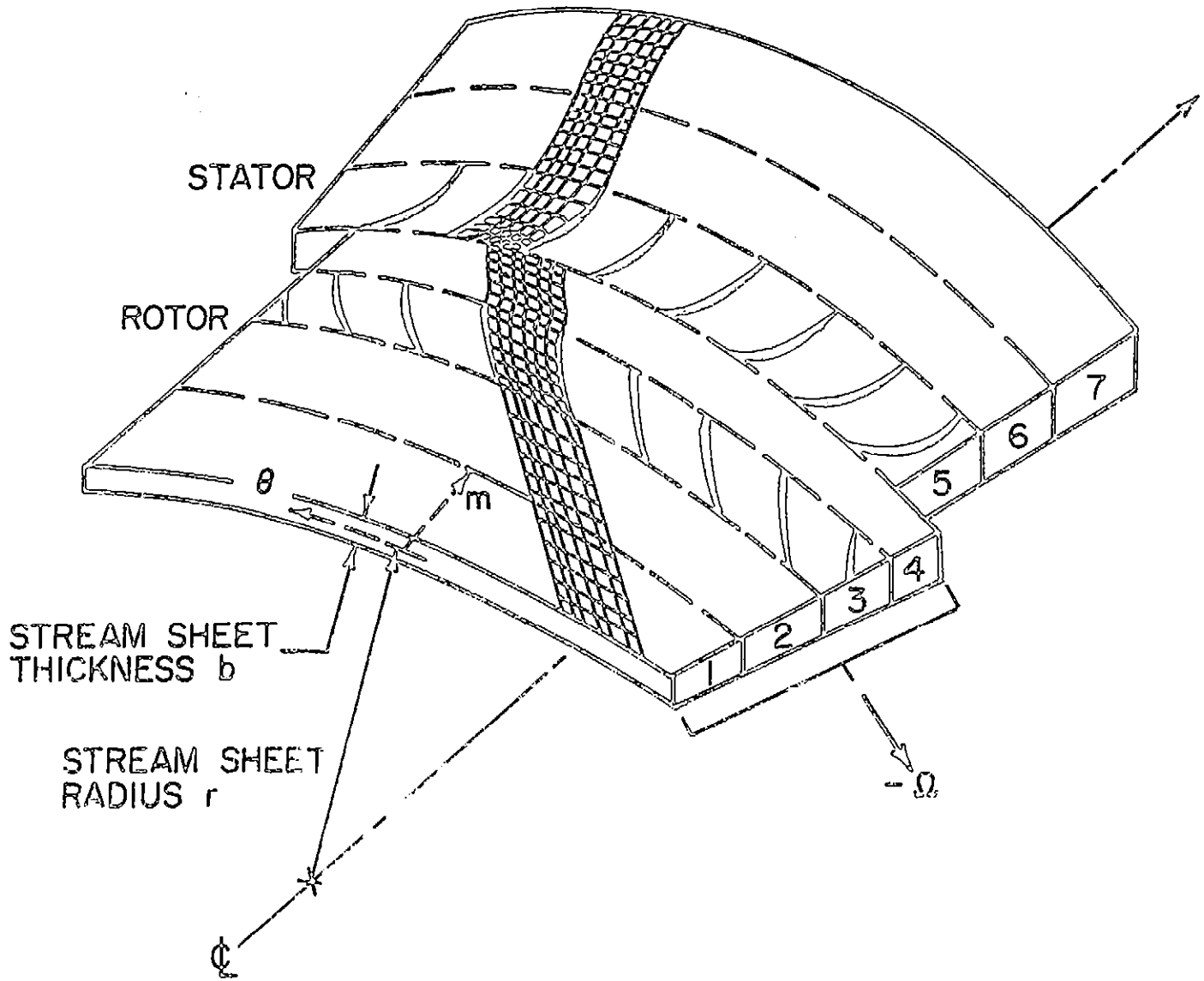

FIGURE 3. BLADE-TO-BLADE COORDINATE SYSTEM AND GRID NETWORK

The lateral boundaries of domains 4, 6 and 7 are the instantaneous locations of the blade slipstreams, $\theta_s(m,t)$. Each domain is mapped from its shape in physical space into a unit square by defining stretched meridional and circumferential coordinates, σ and ν, given (in an absolute reference frame) by:

$$\sigma = \frac{m-m_i}{m_{i+1}-m_i} \qquad \text{(in the } i^{th} \text{ domain)} \tag{31}$$

$$\nu = \frac{\theta-\theta_\ell}{\theta_u-\theta_\ell} \tag{32}$$

where m_i refers to the location of the upstream boundary of the ith domain, as measured on the stream surface from an arbitrary axial station. The location of the upstream boundary of domain 1, m_1, and the location of the downstream boundary of domain 7, m_8, can be selected arbitrarily. However, m_3, m_4, m_5 and m_6 are necessarily the planes of the leading and trailing edges of the first and second blade rows. The locations m_2 and m_7 are defined to lie one chord length upstream and downstream of the first and second blade rows, respectively:

$$m_2 = 2m_3 - m_4 \tag{33}$$

$$m_7 = 2m_6 - m_5 \tag{34}$$

If m_2 and m_7 are selected as the inlet and discharge stations at which the boundary conditions are to be applied, domains 1 and 7 are not used. Otherwise m_1 and m_8 represent the inlet and discharge stations, respectively.

Transformation of Variables to Computational Domains

The relative upper and lower boundaries of the domains, y_u and y_ℓ, are functions of meridional distance, x, and may be functions of time, as well, in domains 4, 6 and 7 where they represent the instantaneous slipstream contours. Thus, the final transformation from physical space (x,y,t) (relative or absolute) to computational space (σ,ν,τ) is defined by:

$$\tau = t\, a_o/L \tag{35}$$

$$\sigma = \frac{x-x_i}{x_{i+1}-x_i} \tag{36}$$

$$\nu = \frac{y-y_\ell}{y_u-y_\ell} \tag{37}$$

$$\frac{\partial}{\partial t} = \frac{\partial\tau}{\partial t}\frac{\partial}{\partial\tau} + \frac{\partial\nu}{\partial t}\frac{\partial}{\partial\nu} = \frac{a_o}{L}\left[\frac{\partial}{\partial\tau} - \frac{y_\tau}{y_\nu}\frac{\partial}{\partial\nu}\right] \tag{38}$$

$$\frac{\partial}{\partial x} = \frac{\partial\sigma}{\partial x}\frac{\partial}{\partial\sigma} + \frac{\partial\nu}{\partial x}\frac{\partial}{\partial\nu} = \frac{1}{x_\sigma}\left[\frac{\partial}{\partial\sigma} - \frac{y_\sigma}{y_\nu}\frac{\partial}{\partial\nu}\right] \tag{39}$$

$$\frac{\partial}{\partial y} = \frac{\partial\nu}{\partial y}\frac{\partial}{\partial\nu} = \frac{1}{y_\nu}\frac{\partial}{\partial\nu} \tag{40}$$

where:

$$y_\tau = \nu\frac{\partial y_u}{\partial\tau} + (1-\nu)\frac{\partial y_\ell}{\partial\tau} \tag{41}$$

$$y_\nu = (y_u-y_\ell) \tag{42}$$

$$x_\sigma = (x_{i+1}-x_i) \tag{43}$$

$$y_\sigma = \nu\frac{\partial y_u}{\partial\sigma} + (1-\nu)\frac{\partial y_\ell}{\partial\sigma} \tag{44}$$

and:

$$x_i = m_i \tag{45}$$

$$y_u = r\,\theta_u \quad \text{at } x=\text{constant} \tag{46}$$

$$y_\ell = r\,\theta_\ell \quad \text{at } x=\text{constant} \tag{47}$$

L is an arbitrary reference length and a_o is a reference speed of sound. In addition, a reference pressure p_o will be introduced below to complete the non-dimensionalization of variables. Particular values for L, a_o and p_o will be assigned later. It should be noted that σ and ν are non-orthogonal coordinates. The transformation is non-singular for $x_\sigma y_\nu \neq 0$.

The correspondence between the physical and computational domains is indicated schematically in Figure (4). Within the computational domain Equations

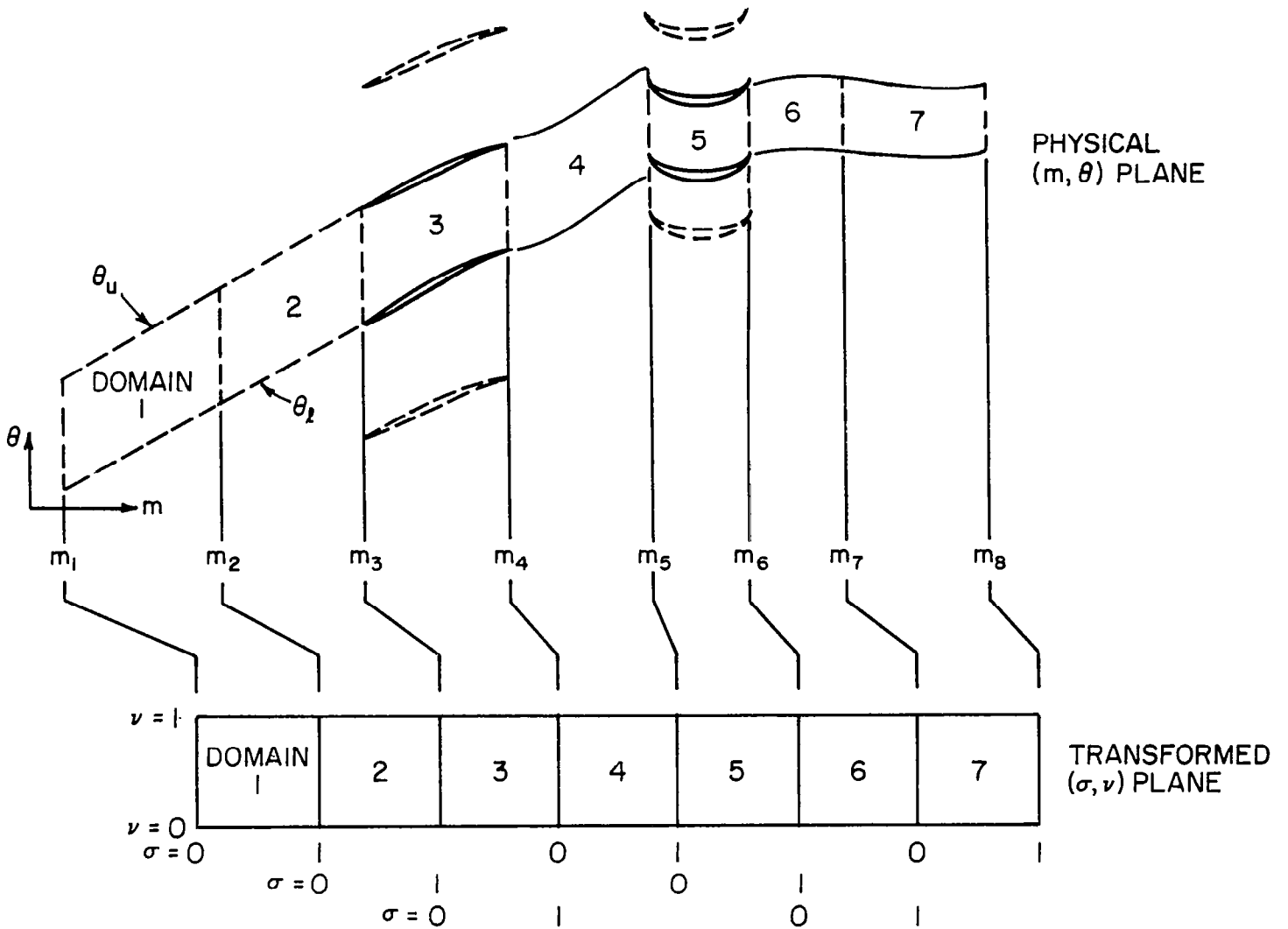

FIGURE 4. SCHEMATIC REPRESENTATION OF PHYSICAL AND COMPUTATIONAL DOMAINS

(27), (28a), (29a) and (30a) are expressed concisely by:

$$\frac{\partial e}{\partial \tau} = - \left(A \frac{\partial e}{\partial \nu} + B \frac{\partial f}{\partial \sigma} + C \frac{\partial f}{\partial \nu} + D \frac{\partial g}{\partial \nu}\right) + h \tag{48}$$

where

$$e = \rho \frac{a_o^2}{p_o} \times \begin{vmatrix} 1 \\ u/a_o \\ v/a_o \\ E'/a_o^2 \end{vmatrix} \tag{49}$$

$$f = \rho \frac{u a_o}{p_o} \times \begin{vmatrix} 1 \\ (u+p/\rho u)/a_o \\ v/a_o \\ H'/a_o^2 \end{vmatrix} \tag{50}$$

$$g = \rho \frac{v a_o}{p_o} \times \begin{vmatrix} 1 \\ (u/a_o) \\ (v+p/\rho v)/a_o \\ H'/a_o^2 \end{vmatrix} \tag{51}$$

$$h = - \frac{\rho u a_o L}{p_o} \left(\frac{1}{rb} \frac{drb}{dx}\right) \times \begin{vmatrix} 1 \\ u/a_o \\ v/a_o \\ H'/a_o^2 \end{vmatrix} + \frac{\rho}{r} \frac{dr}{dx} \frac{a_o^2 L}{p_o} \times \begin{vmatrix} 0 \\ (v+\Omega r)^2/a_o^2 \\ -u(v+2\Omega r)/a_o^2 \\ 0 \end{vmatrix} \tag{52}$$

and

$$A = - \frac{y_\tau}{y_\nu} \tag{53}$$

$$B = \frac{L}{x_\sigma} \tag{54}$$

$$C = -\frac{L}{x_\sigma}\frac{y_\sigma}{y_\nu} \tag{55}$$

$$D = \frac{L}{y_\nu} \tag{56}$$

Note that $f=f(e)$, $g=g(e)$ and $h=h(e,r,b,\Omega)$ thus f, g, and h are known functions of the basic dependent variables contained in e.

The above form of the governing equations is used at all interior grid points, as will be outlined in the following section. The non-conservative form, i.e., Equations (27), (28b), (29b) and (30b), is employed at the boundary points in local orthogonal coordinate systems which will be discussed in connection with the boundary conditions and boundary point solution algorithms.

Interior Point Solution Algorithm

Each of the seven (7) computational domains is spanned by a rectangular grid network, having a mesh size of $\Delta\sigma$ by $\Delta\nu$:

$$\Delta\sigma = 1/(JS-2) \tag{57}$$

$$\Delta\nu = 1/(KS-4) \tag{58}$$

The coordinates of the grid points are given by:

$$\sigma_j = (j-2)\ \Delta\sigma \qquad j = 1,2,3\ldots JS,\ JS+1 \tag{59}$$

$$\nu_k = (k-4)\ \Delta\nu \qquad k = 4,5,6\ldots KS \tag{60}$$

In addition, time is advanced in increments of $\Delta\tau$:

$$\tau_i = (i-1)\ \Delta\tau \qquad i = 1,2,3\ldots\infty \tag{61}$$

where the value of $\Delta\tau$ is determined by a combination of stability and geometric constraints which will be discussed later. The upper limit on the time counter i is not generally known a priori, but it should be sufficiently large that an asymptotic solution is attained.

The same values of JS and KS are used in all seven domains. The grid columns j=2 and JS correspond to the axial boundaries $m=m_i$ and m_{i+1}. The columns j=1 and JS+1 overlap into the adjacent domains and are used to patch the solutions together. At the inlet station (which may be either m_1 or m_2) the grid column j=2 is composed of boundary points (to be discussed later) and the column j=1 is unused. Correspondingly, at the discharge station (either m_7 or m_8) the grid column j=JS is composed of boundary points and the column JS+1 is unused.

The grid rows k=4 and KS correspond to the circumferential boundaries of the blade-to-blade passage $\theta=\theta_\ell$ and θ_u. The grid rows k = 1,2 and 3 and k = KS+1, KS+2 and KS+3 are exterior to the computational domain and are reserved for the solution in portions of the adjacent blade-to-blade passages given by:

$$\nu_k = (k-3) \quad \Delta\nu \qquad k = 1,2 \text{ and } 3 \tag{62}$$

$$\nu_k = (k-5) \quad \Delta\nu \qquad k = KS+1,\ KS+2 \text{ and } KS+3 \tag{63}$$

Thus, it can be seen in Figure (5) that the rows k=3 and 4 occupy the same locations on the transformed boundary $\nu=0$. The rows k = KS and KS+1 correspondingly occupy the same boundary $\nu=1$. On the slipstreams these points also occupy the same physical locations. This convention was adopted in view of the anticipated double-valued solutions which will pertain to each side of the blade slipstreams which form the circumferential boundaries of domains 4, 6 and 7. On the blades, the row k=3 occupies a position corresponding to k=KS, and 4 to KS+1, as indicated in Figure (5).

The finite-difference algorithm developed by MacCormack[13] is employed to carry out the solution at the interior grid points. This algorithm is based on the following second-order approximation to the time derivative

$$e_{i+1,j,k} = e_{i,j,k} + \frac{1}{2}\left(\left(\frac{\partial e}{\partial \tau}\right)^p_{i+1,j,k} + \left(\frac{\partial e}{\partial \tau}\right)_{i,j,k}\right) \Delta\tau \tag{64}$$

where the subscripts i,j,k refer to the discrete values of τ, σ, and ν defined by Equations (59), (60) and (61), and the superscript p indicates a

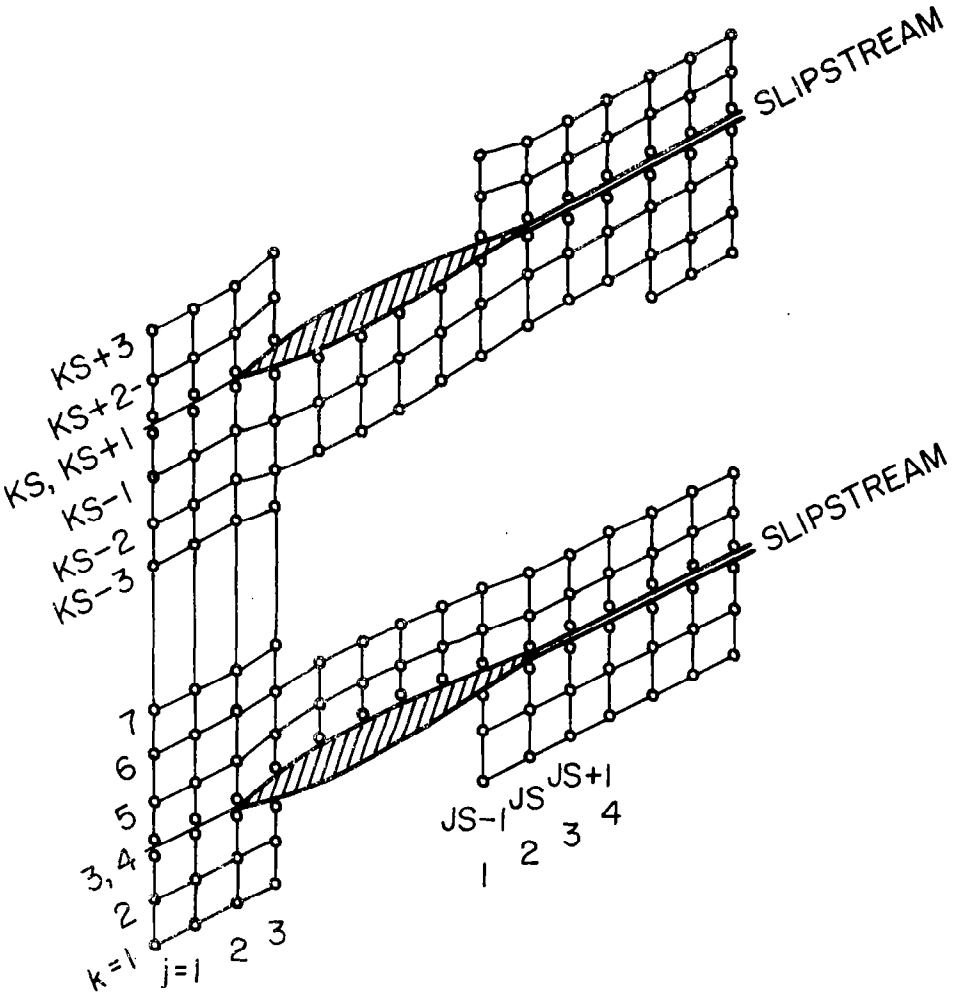

FIGURE 5. GRID ROW ORDERING IN VICINITY OF BLADES AND SLIPSTREAMS

"provisional" (or "predictor") value. The "provisional" values a
in a first or "predictor" step:

$$e^{p}_{i+1,j,k} = e_{i,j,k} + \left(\frac{\partial e}{\partial \tau}\right)_{i,j,k} \Delta\tau$$

Thus Equation (64) can be rewritten as:

$$e_{i+1,j,k} = \frac{1}{2}\left(e_{i,j,k} + e^{p}_{i+1,j,k} + \left(\frac{\partial e}{\partial \tau}\right)^{p}_{i+1,j,k} \Delta\tau\right)$$

which constitutes the second or "corrector" step.

It should be noted that the first or "predictor" step given
(65) can be carried out consistently with the initial value chara
interior point solution, i.e., it only involves the known values
and spatial derivatives thereof at time τ_i as given by Equation (
the second or "corrector" step, Equation (66), requires knowledge
ary point values at time τ_{i+1} to complete the evaluation of the s
tives at the points adjacent to the boundaries at time τ_{i+1}. The
practice, the interior point solution cannot be completed by this
analogous two-step type algorithms without first completing the b
solutions, which will be discussed subsequently. It will be show
boundary point algorithms used herein can be carried out entirely
the known solution at τ_i and therefore, in fact, are executed pri
terior point algorithm.

The MacCormack algorithm achieves satisfactory stability wit
tion of artificial damping terms or numerical filtering procedure
of first-order, non-centered finite-difference approximations to
derivatives which alternate direction between the first and secor
resulting solution is, however, considered to be second-order acc
space and time due to the combination of alternating direction di
in the second or "corrector" step[13]. For example, on the "predic
spatial derivative may be approximated by:

$$\left(\frac{\partial f}{\partial \sigma}\right)_{i,j,k} = \frac{f_{i,j,k} - f_{i,j-1,k}}{\Delta\sigma}$$

Then on the corrector step

$$\left(\frac{\partial f}{\partial \sigma}\right)^{p}_{i+1,j,k} = \frac{f^{p}_{i+1,j+1,k} - f^{p}_{i+1,j,k}}{\Delta\sigma} \tag{67b}$$

must be used. The same procedure applies to the ν derivatives. Since the order in which the direction of the differences is evaluated is arbitrary, it may be cyclically rotated to avoid imposing a preferential bias in the solution. The rotation algorithm is illustrated in Table I. The central grid

TABLE I

ROTATION ALGORITHM FOR SPATIAL DERIVATIVE EVALUATION

Time Step	Iterate	σ Derivative Indices	ν Derivative Indices
.			
.			
.			
i	1	j+1, j	k+1, k
i	2	j, j-1	k, k-1
i+1	1	j+1, j	k, k-1
i+1	2	j, j-1	k+1, k
i+2	1	j, j-1	k, k-1
i+2	2	j+1, j	k+1, k
i+3	1	j, j-1	k+1, k
i+3	2	j+1, j	k, k-1
.			
.			
.			

point is the j,k point in all cases; thus the circumferential position index maintained in evaluation of the σ derivative is understood to be k, and the streamwise position index maintained in evaluation of the ν derivative is understood to be j. Note that during any time step, combination of the first and second iterates produces a time-split central difference, e.g.:

$$\frac{1}{2}\left(\left(\frac{\partial f}{\partial \sigma}\right)_{i,j,k} + \left(\frac{\partial f}{\partial \sigma}\right)^{p}_{i+1,j,k}\right) = \frac{f^{p}_{i+1,j+1,k} - f^{p}_{i+1,j,k} + f_{i,j,k} - f_{i,j-1,k}}{2\Delta\sigma} \tag{68}$$

MacCormack[14] has indicated that cyclic rotation should enhance the stability of the system. However, in the authors experience it has also been found to amplify numerical oscillations in the vicinity of a shock wave (i.e., pressure undershoots and overshoots). The latter phenomenon is not an instability in the usual numerical sense, but rather amplification of oscillations associated with representation of a discontinuity by a continuous function. For this reason, the option to <u>not</u> use the combinations shown in Table I for steps i+1, i+2 and i+3 has been retained in the computer code, at the discretion of the user.

In reference to convergence and stability, the CFL criteria places an upper limit on the permissible time step:

$$\Delta\tau \leq \min\left[\left(\frac{\Delta\sigma}{u+a}\right) \times \left(\frac{a_o(x_{i+1} - x_i)}{L}\right), \left(\frac{\Delta\nu}{v+a}\right) \times \left(\frac{a_o(y_u - y_\ell)}{L}\right)\right] \tag{69}$$

The application of boundary conditions in the case of unequal numbers of blades in the two blade rows (which will be discussed later) is based on a phase lag in time. Implementation of the phase relations requires a constant value of $\Delta\tau$; therefore an estimate of the maximum anticipated values of u+a and v+a must be made to determine the allowable step size $\Delta\tau$. In addition, the value must then be reduced such that the time for one blade of the second row to cross a single passage of the first row is an integer number of time steps. (The latter constraint obviously does not apply when only a single row is considered.)

Inlet and Discharge Boundary Conditions and Boundary Point Solution Algorithm

The present formulation assumes that the periodicity of the flow field results entirely from the interaction of the rotor and stator blade rows. Accordingly, any nonuniformity, either spatial or timewise, of the properties of the flow crossing the inlet or discharge station attributable to inward travelling waves or inward convection must be ruled out, since its existence would add unsteady components to the flow which are not accounted for by the blade row interaction model. Identification of the flow properties which propagate by convection and by wave motion is facilitated by recasting the

system of equations in characteristic form.

The characteristic surfaces formed by the hyperbolic system of partial differential equations given by Equations (27) through (30) consist of a conoid with its base on the x,y plane and within it a stream path which intersects the conoid at its vertex. If the vertex is placed at a grid point at time $t+\Delta t$, the base covers the domain of dependence of the point at time t. A particularly useful approximation to the true characteristic form is obtained by stating the system of equations in a reference plane coordinate system which reduces the problem to a more tractable two-dimensional (i.e., time and distance) form. If the reference plane is normal to both the x,y plane (t=constant) and the inlet station (x=constant) and is allowed to translate in the y direction at the same velocity as the circumferential component of gas velocity, v, then (as will be shown) the system of characteristic lines illustrated in Figure (6) is obtained. The lines AO and CO approximate the intersection of the reference plane and the true characteristic conoid, and can be interpreted as paths of downstream and upstream travelling waves. The line BO is the stream path, which also lies in the reference plane.

It is also pointed out parenthetically that translation of the reference plane at the velocity v in effect transforms a rotating frame of reference back to an absolute frame. Thus, the inlet and discharge station solutions are effectively carried out in an absolute frame regardless of the relative motion of the computational domains, and the numerical results are entirely independent of this transformation.

Those characteristic lines which originate outside the computational domain at time t and intersect a boundary point at time $t+\Delta t$ each represent at least one equation which must be replaced by a boundary condition to render a determinate solution at the boundary point. Obviously, a subsonic axial Mach number, i.e., $(u-a) < 0$, has been assumed in the construction of line CO in Figure (6). Should the axial Mach number at the inlet be supersonic, all characteristics would originate outside the computational domain, and accordingly the complete solution at this boundary could be specified as a boundary condition. Correspondingly, a supersonic axial Mach number at the discharge station would imply that no characteristics originate outside the computational

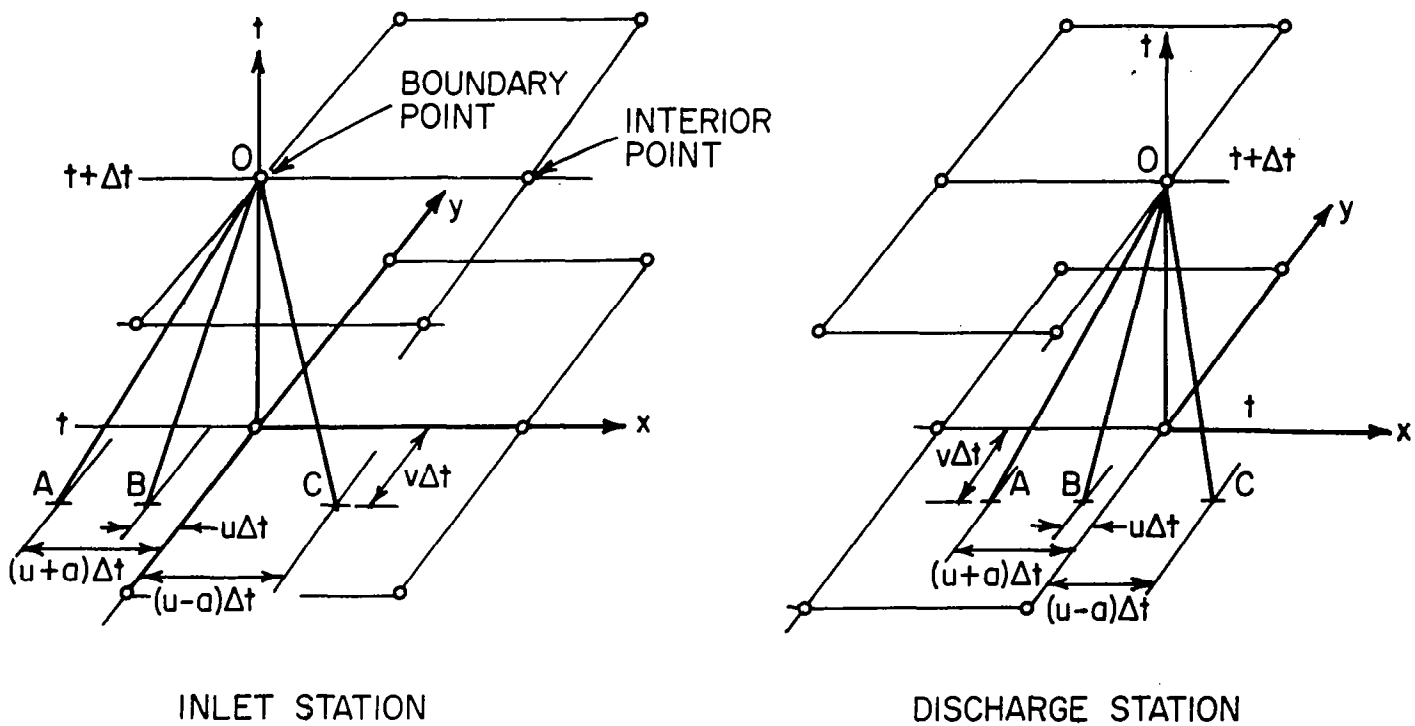

FIGURE 6. CHARACTERISTIC LINES AND GRID POINTS AT INLET AND DISCHARGE STATIONS

domain and, therefore, no boundary condition can be specified. The present analysis is formulated with respect to subsonic axial Mach numbers, but consideration of supersonic axial flow clearly requires only a minor variation of the solution algorithm. In this case, specification of three (3) boundary conditions at the inlet will be required (one to replace the wave motion characteristic AO and two to replace stream path characteristics on BO). At the discharge station one (1) boundary condition will be required to replace the wave motion characteristic on CO. Derivation and discussion of the characteristic relations and boundary point solution algorithms follows.

(a) Stream Path Characteristics - The energy equation as given by Equation (11) is already in characteristic form; it can be integrated to yield (in terms of the two-dimensional system given by Equations 20 to 24):

$$S = \text{constant} \quad \text{on} \quad \frac{dx}{u} = \frac{dy}{v} = dt \tag{70}$$

Equation (70) states the well known fact that in unsteady flows entropy is convected on stream paths. It is evident that the entropy convects inward (assuming $u > 0$) across the inlet station and outward across the discharge station. The condition S = constant everywhere upstream of the inlet station forms the first boundary condition to be applied at the inlet.*

The momentum equation, Equation (2), can be rewritten in terms of the gradients of total enthalpy and entropy rather than pressure:

$$\frac{\partial \vec{V}}{\partial t} = - \nabla H + \vec{V} \times \nabla \times \vec{V} + T\nabla S \tag{71}$$

If $\nabla S = 0$, as at the inlet, then the curl of Equation (71) gives the vorticity transport equation:

$$\frac{\partial \vec{\omega}}{\partial t} + \nabla \times (\vec{\omega} \times \vec{V}) = 0 \tag{72}$$

*The value of the entropy at the inlet could, of course, be increased by upstream travelling shock waves. However, it is assumed that any shock waves reaching the inlet station are sufficiently weak to be considered isentropic.

where the vorticity vector is defined by $\vec{\omega} = \nabla x \vec{V}$.

Equation (72) can be expanded and combined with the continuity equation, Equation (1), to obtain:

$$\frac{D}{Dt}\left(\frac{\vec{\omega}}{\rho}\right) = \frac{\vec{\omega}}{\rho} \cdot \nabla\vec{V} \tag{73}$$

In terms of the presently considered two-dimensional system given by Equations (20) through (24), the only non-zero component of vorticity is the normal component $\zeta = (\partial v/\partial x - \partial u/\partial y)$. Accordingly, Equation (73) reduces to:

$$\frac{D}{Dt}\left(\frac{\zeta}{\rho}\right) = 0 \tag{74}$$

or

$$\frac{\zeta}{\rho} = \text{constant} \quad \text{on} \quad \frac{dx}{u} = \frac{dy}{v} = dt \tag{75}$$

Thus, it can be seen that the ratio of vorticity to density also convects on stream paths.* The condition $\zeta = 0$ upstream of the inlet station is taken as the second boundary condition to be applied at the inlet station.

To summarize, Equations (70) through (75) apply on the stream path characteristic, line BO in Figure (6), and have been replaced by the boundary condition S = constant and $\zeta = 0$.

(b) Wave Motion Characteristics - The equation of state, Equation (12) can be differentiated with respect to time using the convective operator:

$$\frac{1}{p}\frac{Dp}{Dt} = \frac{\gamma}{\rho}\frac{D\rho}{Dt} + \frac{1}{C_v}\frac{DS}{Dt} \tag{76}$$

---

*In the present context this result is restricted to conditions for which $\partial S/\partial y = 0$, e.g., at the inlet station. It can also be proven for barotropic and constant density fluids.

The continuity equation, Equation (27), and the energy equation, Equation (30b), can be substituted into the above relation, and the streamwise momentum equation, Equation (28b), then added to and subtracted from the result to obtain:

$$\frac{a}{\gamma p}\left[\frac{\partial p}{\partial t} + (u \pm a)\frac{\partial p}{\partial x} + v\frac{\partial p}{\partial y}\right] \pm \left[\frac{\partial u}{\partial t} + (u \pm a)\frac{\partial u}{\partial x} + v\frac{\partial u}{\partial y}\right]$$
$$= -a\left(\frac{\partial v}{\partial y} + \frac{u}{rb}\frac{drb}{dx}\right) \pm (v+\Omega r)^2 \frac{1}{r}\frac{dr}{dx} \tag{77}$$

or

$$\frac{a}{\gamma p}\frac{dp}{dt} \pm \frac{du}{dt} = -aQ_1 \pm Q_2 \quad \text{on} \quad \frac{dx}{u \pm a} = \frac{dy}{v} = dt \tag{78}$$

where Q_1 and Q_2 are identified as the terms appearing on the right hand side of Equation (77). Equation (78) applies on the characteristic lines originating at points A and C at time t which intersect the boundary point O at time $t+\Delta t$ in Figure (6). The set of equations represented by Equation (78) are commonly referred to as the compatibility relations. The member of the set with the + sign applies on the line AO at the inlet and will be replaced by an inlet boundary condition. The member of the set with the - sign applies on the line CO at the discharge station and will also be replaced by a boundary condition. Application of the compatibility relations on line CO at the inlet station and line AO at the discharge station to complete the boundary point solution algorithms will also be outlined below.

(c) Modelling of Duct Boundary Conditions - As indicated above in connection with the stream path description, it is assumed that $S = 0$ and $\zeta = 0$ at the inlet. These conditions derive from the convective character of Equations (70) and (75) and are independent of the physical structure of the inlet duct. On the other hand, the propagation of waves across the inlet or discharge station is dependent on the configration of the duct, as is well known from acoustic theory which ascribes impedance functions to the geometric and material properties of the duct. (Since the present model neglects the radial velocity component, radial wave modes and wall impedance properties are correspondingly assumed to be absent.)

Two limiting cases have been considered to be descriptive of the duct configuration at the inlet or discharge station. One case is an infinite duct, i.e., the inlet or discharge station is located in a region of constant cross-

sectional area which extends "very far" outward from the inlet or discharge station. Consequently, all outward radiating waves should pass the inlet or discharge station without reflection in this case, and continue travelling outward "forever" on the time scale of the problem. No reflected waves from $x \to \pm \infty$ should ever reach the computational domain.

The second case represents the opposite limit in which all pressure waves are reflected at the inlet or discharge station; this case is termed an open-end duct since it corresponds to the type of reflection associated with the open-end of an organ pipe. The boundary condition is that the pressure matches the plenum pressure outside the duct, namely:

$$p_{inlet}(y,t) = p_{-\infty} \tag{79}$$

$$p_{discharge}(y,t) = p_{\infty} \tag{80}$$

where the subscripts $\pm\infty$ denote $x>x_{discharge}$ and $x<x_{inlet}$ respectively.

Modelling of the non-reflective condition for an infinite duct is somewhat more complex, particularly in regard to the swirling waves produced by a rotor-stator interaction. A precise mathematical formulation of the flow field solution upstream of the inlet station and downstream of the discharge station based on a small-perturbation analysis is described in Volume III of this report, and is herein referred to as the acoustic far-field model for an infinite duct. It accomplishes the desired objective of allowing an arbitrary transient signal to radiate outward without reflection and asymptotic attainment of a periodic solution with as many harmonic components as can be derived from the number of grid points spanning the considered boundaries. However, an approximate model of the infinite duct condition has also been developed which does not require use of the acoustic far-field analysis. In the approximate model, the infinite duct conditions are derived from the wave-motion characteristics represented by Equation (78). Consequently, the discrete acoustic modes are not explicitly identified in the approximate model, and their unimpeded transmission across the boundary cannot be guaranteed. In the approximate infinite duct model, Equation (78) is integrated to yield:

$$\frac{2a}{\gamma-1} \pm u = \int (-aQ_1 \pm Q_2)\, dt + \text{constant}$$

$$\text{on } \frac{dx}{u \pm a} = \frac{dy}{v} = dt \tag{81}$$

where S = constant along the wave path is assumed. Outside the computational domain r = constant and b = constant is assumed. The remaining term in the integrand of Equation (81), namely a $\partial v/\partial y$, accounts for the two-dimensionality of the actual wave surfaces, as compared to the one-dimensional (helical) surfaces which would result if the swirl component of velocity, v, were constant or only a function of x. If $\partial v/\partial y$ is neglected outside the computational domain, then the well-known Riemann invariants for the incoming waves are obtained from Equation (81):

$$\left(\frac{2a\ (y,t)}{\gamma-1} + u\ (y,t)\right)_{\text{inlet}} = \frac{2a_{-\infty}}{\gamma-1} + u_{-\infty} \tag{82}$$

$$\left(\frac{2a\ (y,t)}{\gamma-1} - u\ (y,t)\right)_{\text{discharge}} = \frac{2a_{\infty}}{\gamma-1} - u_{\infty} \tag{83}$$

In this case the subscripts denote the specified values for $x \to \pm\infty$, i.e., the "ends" of the infinite duct. The two-dimensionality of the outward radiating waves at the inlet or discharge station is retained by evaluating the integrand of Equation (81) numerically:

$$\frac{2a}{\gamma-1} \pm u = \left(\frac{2a}{\gamma-1} \pm u\right)_{\substack{a\\c}} + \int_{t}^{t+\Delta t} (-aQ_1 \pm Q_2)\, dt \tag{84}$$

where:

$$x_{\substack{a\\c}} = x - (u \pm a)_{\substack{a\\c}}\ \Delta t \tag{85}$$

Some distortion of the swirling waves at the inlet and discharge boundaries can be expected to result from the above model of infinite duct boundary conditions, due to the representation of the incoming waves by the Riemann invariants for a one-dimensional unsteady flow. The severity of the distortion will depend on the relative strengths of the two wave systems and, therefore, should not be serious since the outgoing waves (which produce the swirl) are described by a two-dimensional system of equations. In no event should this

model generate the standing waves associated with an open duct condition, but neither can it be expected to duplicate the perfect wave transmission of the acoustic far-field model described in Volume III of this report. Therefore, the approximate infinite duct boundary conditions are considered to offer a useful analytical tool for analysis of the aerodynamic performance of interacting blade rows without invoking the additional computational complexity of the acoustic far-field analysis.

(d) Circumferential Velocity Solution - The determination of the swirl component of velocity at the boundary points at time $t+\Delta t$ can be accomplished by use of the circumferential component of Equation (71):

$$\frac{\partial v}{\partial t} = - \frac{\partial H'}{\partial y} + T \frac{\partial S}{\partial y} - u\zeta \tag{86}$$

Equation (86) pertains to the flow normal to the reference plane in which the wave paths have been identified above. Thus, the swirl component of velocity does not exhibit a wave-like behavior in this formulation. Furthermore, Equation (86) does not involve any streamwise gradients (if ζ is known) and can, therefore, be evaluated along the inlet or discharge boundary by the same finite difference algorithm employed at the interior points. The swirl component of velocity is, of course, implicitly coupled to the axial component and to the pressure through the gradient of total enthalpy $\partial H'/\partial y$ (even when $S = \zeta = 0$).

(e) Inlet Solution Algorithm - The inlet solution algorithm consists of the stated boundary conditions, namely: $S_{-\infty}$ = constant, $\zeta_{-\infty} = 0$, and either $p_{-\infty}$ = constant (open duct) or $2a_{-\infty}/(\gamma-1) + u_{-\infty}$ = constant (infinite duct), together with the compatibility equation on the upstream wave, line CO in Figure (6), given by Equation (78) and the circumferential momentum equation given by Equation (86). (This combination of 3 boundary conditions and 2 equations may appear redundant since there are only 4 dependent variables, however, the condition $\zeta_{-\infty} = 0$ is a Neumann type boundary condition which only serves to allow solution of Equation (86) without knowledge of streamwise derivatives.)

The boundary condition $S_{-\infty}$ = constant is enforced by requiring that two thermodynamic properties of the inlet flow which define the entropy be specified, e.g., $S_{-\infty} = C_v \log (p_{-\infty}/k\rho_{-\infty}^{\gamma})$ = constant. Since the open duct condition requires specification of $p_{-\infty}$ and the infinite duct condition requires $a_{-\infty}$,

these two variables have been selected to define $S_{-\infty} = 0$ and, therefore, $k = (a_{-\infty}^2 \; p_{-\infty}^{-(\gamma-1)/\gamma} \; \gamma^{-1})^{\gamma}$, in both cases.

The solution algorithms for the open duct and for the infinite duct inlets are summarized as follows:

(1) Open-End Inlet Duct - The values of $a_{-\infty}$ and $p_{-\infty}$ are specified, and $S_{-\infty} = \zeta_{-\infty} = 0$ is implied. this combination provides the values of p, ρ and e at the inlet:

$$p = p_{-\infty} \tag{87}$$

$$\rho = \gamma p / a_{-\infty}^2 \tag{88}$$

$$e = p/((\gamma-1)\rho) \tag{89}$$

The axial velocity is obtained from the integrated form of the compatibility relation, Equation (84), on the upstream travelling wave:

$$u = u_c + \frac{2(a-a_c)}{(\gamma-1)} + (aQ_1 + Q_2)_c \, \Delta t \tag{90}$$

where the characteristic point x_c, y_c is located relative to the boundary point x,y from:

$$x_c = x - (u_c - a_c) \, \Delta t \tag{91a}$$

$$y_c = y - v_c \Delta t \tag{91b}$$

and the local sound speed is given by

$$a^2 = \gamma p / \rho \tag{92}$$

The circumferential velocity component is obtained from finite-difference solution of Equation (86), using $S_{-\infty} = \zeta_{-\infty} = 0$:

$$\frac{\partial v}{\partial t} = - \frac{\partial H'}{\partial y} \tag{93}$$

(2) Infinite Duct Inlet - The values of $a_{-\infty}$, $p_{-\infty}$ and $u_{-\infty}$ are specified, and $S_{-\infty} = \zeta_{-\infty} = 0$ is implied. In this case, the internal energy is obtained

from the speed of sound, using the compatibility relation (Equation (84)) on the upstream wave:

$$e = \left[\frac{1}{2} (a_c + a_{-\infty}) + \frac{\gamma-1}{4} (u_{-\infty} - u_c - (aQ_1 + Q_2)_c \Delta t) \right]^2 / (\gamma(\gamma-1)) \tag{94}$$

The axial velocity component is obtained from Equation (82):

$$u = \frac{2}{\gamma-1} (a_{-\infty} - a) + u_{-\infty} \tag{95}$$

The pressure and density are given by:

$$p = p_{-\infty} \left(\frac{a}{a_{-\infty}}\right)^{\frac{2\gamma}{\gamma-1}} \tag{96}$$

$$\rho = \frac{\gamma p}{a^2} \tag{97}$$

The circumferential velocity component is again obtained from Equation (93).

The pressure is a redundant member of the set of dependent variables, since it can always be obtained from the density and internal energy, i.e., $p = (\gamma-1)\rho e$; however, it is carried in the above presentation of the inlet solution statement for clarity.

The point x_c, y_c is located by iteration, using linear interpolation to determine the flow properties at the point. A change in position of 0.1% is used as the convergence criterion. In principle, the terms multiplied by Δt in Equations (90), (91a), (91b) and (94) should be replaced by the average of the values at point C and the new values at point O; however, examination of the solution a posteriori indicates that the numerical error involved is too small to warrant the additional computational complexity.

(f) Discharge Station Solution Algorithm - The considerations pertaining to formulation and statement of the discharge station boundary conditions and solution algorithms are similar to those outlined above. However, as indicated in Figure (6), points A and B originate within the computational domain, and point C falls outside. Therefore, the compatibility relation pertaining to

point C is replaced by a boundary condition given by either Equation (80) or (83). Equation (70) is evaluated on the stream path B in this case, using linear interpolation. The discharge station boundary conditions and solution algorithm are summarized by:

(1) Open-End Discharge Duct - Value of p_∞ is specified.

$$p = p_\infty \tag{98}$$

$$\rho = \rho_b \, (p/p_b)^{1/\gamma} \tag{99}$$

$$e = p/((\gamma-1)\rho) \tag{100}$$

$$u = u_a - \frac{2}{\gamma-1} (a-a_a) + (-aQ_1 + Q_2)_a \, \Delta t \tag{101}$$

(2) Infinite Discharge Duct - Values of a_∞ and u_∞ are specified.

$$e = \left[\frac{1}{2} (a_a + a_\infty) + \frac{\gamma-1}{4} (u_a - u_\infty + (-aQ_1 + Q_2)_a \, \Delta t) \right]^2 / (\gamma(\gamma-1)) \tag{102}$$

$$u = \frac{2}{\gamma-1} (a-a_\infty) + u_\infty \tag{103}$$

$$p = \left[\frac{\gamma p_b^{1/\gamma}}{\rho_b a^2} \right]^{-(\gamma/\gamma-1)} \tag{104}$$

$$\rho = \gamma p/a^2 \tag{105}$$

In both cases, the circumferential velocity component is given by:

$$\frac{\partial v}{\partial t} = - \frac{\partial H'}{\partial y} + T \frac{\partial S}{\partial y} - u\zeta \tag{106}$$

and the characteristic point x_a, y_a is located with respect to the discharge boundary point x,y from:

$$x_a = x - (u_a + a_a) \, \Delta t \tag{107}$$

$$y_a = y - v_a \Delta t \tag{108}$$

Equations (99) and (104) utilize Equation (70), i.e., $S = S_b$. Solution of Equation (106) is carried out using a first order upstream difference (i.e., j, j-1) to evaluate the σ derivatives necessary to compute ζ at the boundary points.

Blade Surface and Slipstream Boundary Conditions and Solution Algorithm

(a) Blade Surface Boundary Conditions - The boundary condition at the blade surface is simply impermeability of the surface, which requires that the component of velocity normal to the surface vanish. The blades are assumed to be thin and have sharp leading and trailing edges, as is typical of high speed compressor and fan blades. Therefore, the Kutta condition which requires the pressure to be continuous and finite at the trailing edge, is applicable. This also implies that the slipstream (i.e., vortex sheet) which emanates from the blade must originate at the trailing edge. Since the blade leading edge is sharp, and the incidence angles are not expected to be large, the streamline which wets the blade surface is assumed to intersect the leading edge. Accordingly, the leading edge pressure is also required to be finite, but not continuous.

(b) Slipstream Boundary Conditions - The boundary conditions pertaining to the slipstream are similar to those for the blade surface in that the slipstream is impermeable, but are dissimilar in that the slipstream is non-rigid. It can be shown from application of the conservation form of the governing equations at an impermeable contact surface that the pressure must be continuous across the slipstream, and that the component of velocity normal to the slipstream surface must also be continuous and equal to the surface velocity. (Thus, in a frame of reference moving with the surface the normal component of velocity must vanish at the surface.) However, the tangential component of velocity may be discontinuous across the slipstream, as well as the density or other thermodynamic properties. These jumps (discontinuities) in flow properties result from unsteady variations in the work performed by the blades, or by differences in shock-produced losses on either side of the blade under steady conditions, for example. It is emphasized that the conservation form of the

equations admit the existence of these jumps across a slipstream, but their magnitudes are not derivable from application of the conservation form of the governing equations to a surface of discontinuity. By contrast, the magnitude of the jumps across a shock wave derive from the Rankine-Hugoniot relations. Therefore, the slipstreams cannot be expected to evolve from a finite difference solution of the governing equations in the same way that shock surfaces are "captured". Consequently, if the slipstream jumps and the corresponding slipstream motion are to be resolved accurately, the slipstreams must be explicitly recognized as surfaces of discontinuity, as they are in the present formulation.

(c) Restatement of Governing Equations - The solution algorithms used at the blade surface and slipstream points are closely related and, therefore, will be derived for the more general case of the slipstream points. The result will then be specialized to the blade surface points and the leading and trailing edge points.

A surface-oriented coordinate system $(\bar{x},\bar{y},t)$, as sketched in Figure (7), is defined by:

$$\frac{\partial}{\partial x} = \cos\phi \frac{\partial}{\partial \bar{x}} - \sin\phi \frac{\partial}{\partial \bar{y}} \tag{109}$$

$$\frac{\partial}{\partial y} = \sin\phi \frac{\partial}{\partial \bar{x}} + \cos\phi \frac{\partial}{\partial \bar{y}} \tag{110}$$

where $\bar{x}$ is the curvilinear distance along the surface, $\bar{y}$ is the distance normal to the surface, and ϕ is the angle between x and $\bar{x}$. The velocity components in this system $(\bar{u},\bar{v})$ are correspondingly defined by:

$$u = \bar{u}\cos\phi - \bar{v}\sin\phi \tag{111}$$

$$v = \bar{u}\sin\phi + \bar{v}\cos\phi \tag{112}$$

In this system, Equations (27), (28b), (29b) and (30b) become:

$$\frac{\partial\rho}{\partial t} + \bar{u}\frac{\partial\rho}{\partial\bar{x}} + \bar{v}\frac{\partial\rho}{\partial\bar{y}} + \rho\left[\frac{\partial\bar{u}}{\partial\bar{x}} + \frac{\partial\bar{v}}{\partial\bar{y}} + \frac{\bar{v}}{R}\right] = -\frac{\rho u}{rb}\frac{drb}{dx} \tag{113}$$

NOTE: AT A BLADE SURFACE POINT $\bar{v}_q = 0$ AND POINTS P AND Q ARE COINCIDENT.

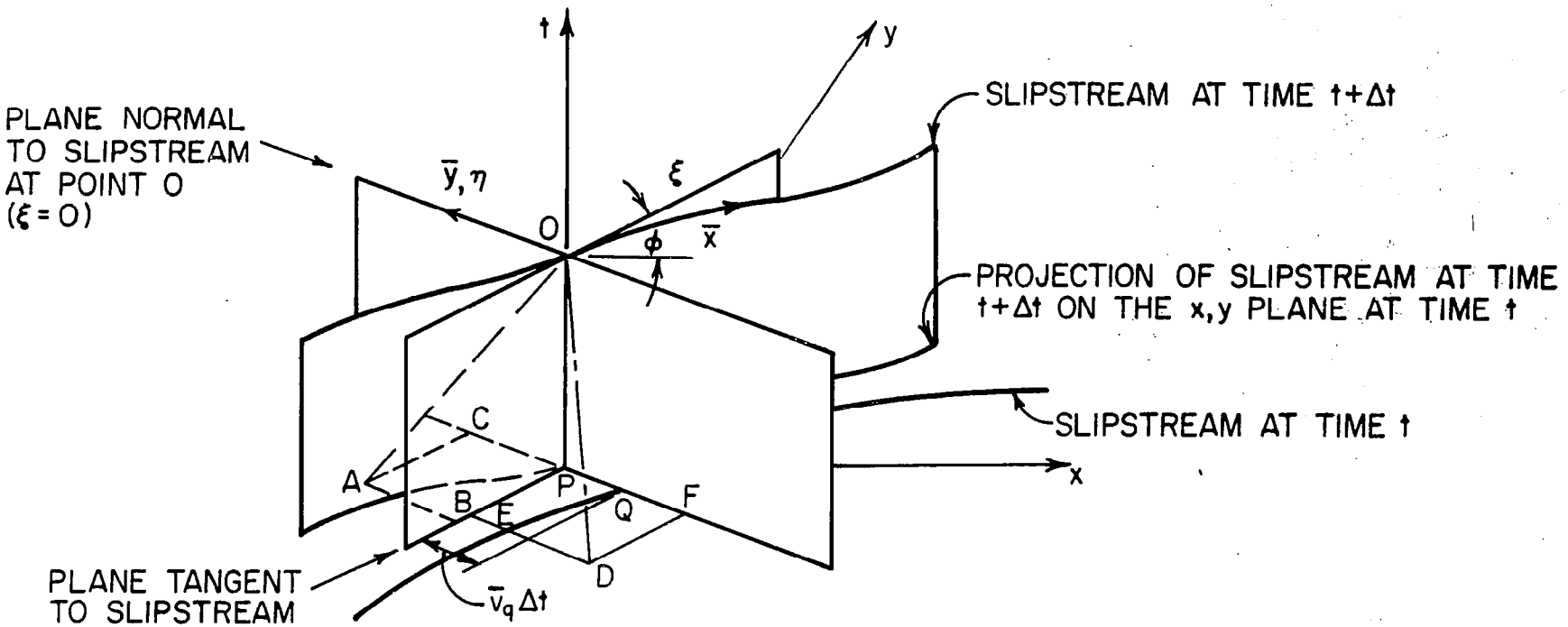

$$\xi_a = -\bar{u}_a \Delta t/L, \quad \eta_a = (a_a - (\bar{v}_a + \bar{v}_q))\Delta t/L$$

$$\xi_d = -\bar{u}_d \Delta t/L, \quad \eta_d = -(\bar{v}_d + \bar{v}_q + a_d)\Delta t/L$$

FIGURE 7. CHARACTERISTIC CONSTRUCTION AT A SLIPSTREAM POINT

$$\frac{\partial \bar{v}}{\partial t} + \bar{u}\frac{\partial \phi}{\partial t} + \bar{u}\frac{\partial \bar{v}}{\partial \bar{x}} + \bar{v}\frac{\partial \bar{v}}{\partial \bar{y}} - \frac{\bar{u}^2}{R} + \frac{1}{\rho}\frac{\partial p}{\partial \bar{y}} = -\frac{1}{r}\frac{dr}{dx}\left(u(v+2\Omega r)\cos\phi + (v+\Omega r)^2 \sin\phi\right) \tag{114}$$

$$\frac{\partial \bar{u}}{\partial t} - \bar{v}\frac{\partial \phi}{\partial t} + \bar{u}\frac{\partial \bar{u}}{\partial \bar{x}} + \bar{v}\frac{\partial \bar{u}}{\partial \bar{y}} + \frac{\bar{u}\bar{v}}{R} + \frac{1}{\rho}\frac{\partial p}{\partial \bar{x}} = -\frac{1}{r}\frac{dr}{dx}\left(u(v+2\Omega r)\sin\phi - (v+\Omega r)^2 \cos\phi\right) \tag{115}$$

$$\frac{\partial S}{\partial t} + \bar{u}\frac{\partial S}{\partial \bar{x}} + \bar{v}\frac{\partial S}{\partial \bar{y}} = 0 \tag{116}$$

where

$$R^{-1} = -\frac{\partial \phi}{\partial \bar{x}} \tag{117}$$

Combination of Equations (113) and (116) and the equation of state yields:

$$\frac{1}{\rho}\frac{\partial p}{\partial t} + \frac{\bar{u}}{\rho}\frac{\partial p}{\partial \bar{x}} + \frac{\bar{v}}{\rho}\frac{\partial p}{\partial \bar{y}} + \gamma\frac{\partial \bar{v}}{\partial \bar{y}} = -\gamma\left(\frac{\partial \bar{u}}{\partial \bar{x}} + \frac{\bar{v}}{R} + \frac{u}{rb}\frac{drb}{dx}\right) \tag{118}$$

Equations (114) and (118) can then be combined to obtain a pair of compatibility relations analogous to those previously discussed in connection with the inlet and discharge boundaries:

$$\begin{aligned}\frac{a}{\gamma p}\left(\frac{\partial p}{\partial t} + (\bar{v}\pm a)\frac{\partial p}{\partial \bar{y}} + \bar{u}\frac{\partial p}{\partial \bar{x}}\right) &\pm \left(\frac{\partial \bar{v}}{\partial t} + (\bar{v}\pm a)\frac{\partial \bar{v}}{\partial \bar{y}} + \bar{u}\frac{\partial \bar{v}}{\partial \bar{x}}\right) \\ = -a\left(\frac{\partial \bar{u}}{\partial \bar{x}} + \frac{\bar{v}}{R} + \frac{u}{rb}\frac{drb}{dx}\right) &\pm \left(\frac{\bar{u}^2}{R} - \bar{u}\frac{\partial \phi}{\partial t} - \frac{1}{r}\frac{dr}{dx}\left(u(v+2\Omega r)\cos\phi + (v+\Omega r)^2\sin\phi\right)\right)\end{aligned} \tag{119}$$

or

$$\frac{a}{\gamma p}\frac{dp}{dt} \pm \frac{d\bar{v}}{dt} = -aQ_1 \pm Q_2 \quad \text{on} \quad \frac{d\bar{x}}{\bar{u}} = \frac{d\bar{y}}{\bar{v}\pm a} = dt \tag{120}$$

The variables Q_1 and Q_2 are defined by identifying the right hand side of Equation (120) term by term with the right hand side of Equation (119).

Implementation of the numerical solution of Equation (120) is facilitated by introduction of an additional coordinate transformation from the curvilinear $(\bar{x},\bar{y})$ system to a series of local Cartesian systems (ξ,η) each of which is tangent to a grid point on the slipstream (or blade surface). The (ξ,η)

system is shown schematically in Figure (7). Note that in the (ξ,η) system, $R^{-1} = \partial\phi/\partial t = 0$. The velocity components $(\bar{u},\bar{v})$ at the grid point at which the local (ξ,η) system is defined are unchanged by this transformation; however, their values at adjacent grid points must be evaluated with respect to the angle ϕ at the subject grid point. The overall effect of these transformations is to make evaluation of Equation (120) closely approximate impingement of a one-dimensional acoustic wave on a surface which is moving at a velocity $\bar{v}$. Although all two-dimensional terms are in fact retained, they can be viewed as "corrections" to a more familiar one-dimensional solution.

The boundary point algorithm is completed by stating the streamwise momentum equation and the energy equation in the curvilinear $(\bar{x},\bar{y})$ system which follows a stream path along the moving surface. The magnitude of the velocity vector along the surface is:

$$\bar{q} = (\bar{u}^2 + \bar{v}^2)^{\frac{1}{2}} \tag{121}$$

The streamwise momentum equation is obtained by multiplying Equations (114) by $\bar{v}$ and (115) by $\bar{u}$ and adding:

$$\frac{D\bar{q}}{Dt} = -\frac{1}{\rho}\frac{\partial p}{\partial \bar{s}} + \frac{\upsilon\,(\Omega r)^2}{\bar{q}\,r}\frac{dr}{dx} \tag{122}$$

where

$$\frac{D}{Dt} = \frac{\partial}{\partial t} + \bar{u}\frac{\partial}{\partial \bar{x}} + \bar{v}\frac{\partial}{\partial \bar{y}} = \frac{\partial}{\partial t} + \bar{q}\frac{\partial}{\partial \bar{s}} \tag{123}$$

Equation (116) integrates exactly to:

$$S = \text{constant} \quad \text{on} \quad \frac{d\bar{s}}{\bar{q}} = \frac{d\bar{x}}{\bar{u}} = \frac{d\bar{y}}{\bar{v}} = dt \tag{124}$$

Equation (122) is not an exact integral, and, in contrast to the compatibility relations, i.e., Equation (120), the integrand on the right hand side of Equation (122) includes a leading term (the pressure gradient) which cannot be adequately approximated by its initial value on the path of integration. Note, however, that Equation (30a) represents a combination of the momentum and energy equations; therefore since Equation (30b) has been used to represent conservation of energy, Equation (30a) can be used to represent conservation of momentum in lieu of Equation (122). Either form should be equivalent, but it will be

seen below that Equation (30a) offers an advantageous form for numerical evaluation. Equations (27) and (30a) can be combined to yield:

$$\frac{\partial H'}{\partial t} + u \frac{\partial H'}{\partial x} + v \frac{\partial H'}{\partial y} = \frac{1}{\rho} \frac{\partial p}{\partial t} \tag{125}$$

In the present coordinate system this becomes

$$\frac{DH'}{Dt} = \frac{1}{\rho} \frac{\partial p}{\partial t} \tag{126}$$

where the convective derivative is defined above by Equation (123). In most applications for unsteady flows, Equation (126) is awkward to evaluate because the time derivative of pressure is not known a priori. However, in the present formulation, the pressure at time t_1 (point 0 in Figure 7) is determined from the solution of Equation (120), which is uncoupled from Equation (126) and, therefore, can be evaluated prior to (126). Thus, the term in question can be accurately approximated by:

$$\frac{1}{\rho} \frac{\partial p}{\partial t} = \frac{2\ (p_o - p_q)}{(\rho_o + \rho_q)\ \Delta t} \tag{127}$$

Accordingly, Equation (126) integrates to:

$$H' = \text{constant} + \frac{2\ (p_o - p_q)}{(\rho_o + \rho_q)} \tag{128}$$

$$\text{on} \quad \frac{d\bar{s}}{\bar{q}} = \frac{d\bar{x}}{\bar{u}} = \frac{d\bar{y}}{\bar{v}} = dt$$

The constants indicated in Equations (124) and (128) are determined by evaluating S and H', respectively, at a distance $\Delta\bar{s} = \bar{q}\ \Delta t$ upstream of the point Q (in Figure 7). Although neither Equations (126) or (122) are exact integrals, as is Equation (124), the time derivative of pressure along line QO (in Figure 7) can be more accurately represented than its spatial derivative at point B or E (which must be interpolated). Numerical experimentation has shown that integration of Equation (126) yields correspondingly more accurate re-

sults than integration of Equation (122).

(d) Blade Surface Solution Algorithm - Equations (120), (124) and (128) constitute the system of governing equations as applied on the blade surface and slipstream points. Therefore, with reference to the geometry indicated in Figure (7), and reverting to the subscripts ℓ and u to denote lower and upper boundary surfaces, respectively, the solution at a blade surface point 0 is given by:

$$\bar{v}_\ell = \bar{v}_u = 0 \tag{129}$$

$$\log p_\ell = \log p_a - \frac{\gamma}{a_a} (\bar{v} + (aQ_1 + Q_2)\Delta t)_a \tag{130a}$$

$$\log p_u = \log p_d + \frac{\gamma}{a_d} (\bar{v} - (aQ_1 - Q_2)\Delta t)_d \tag{130b}$$

$$S_\ell = S_b \quad \text{or} \quad \rho_\ell = \rho_b \ (p_\ell/p_b)^{1/\gamma} \tag{131a}$$

$$S_u = S_e \quad \text{or} \quad \rho_u = \rho_e \ (p_u/p_e)^{1/\gamma} \tag{131b}$$

$$H'_\ell = H'_b + \frac{2\ (p_\ell - p_{\ell_q})}{(\rho_\ell + \rho_{\ell_q})} \tag{132a}$$

$$\bar{u}_\ell = (2\ (H'_\ell - \frac{\gamma}{\gamma-1} \frac{p_\ell}{\rho_\ell}) + \Omega^2 r^2)^{\frac{1}{2}} \tag{132b}$$

$$H'_u = H'_e + \frac{2\ (p_u - p_{u_q})}{(\rho_u + \rho_{u_q})} \tag{132c}$$

$$\bar{u}_u = (2\ (H'_u - \frac{\gamma}{\gamma-1} \frac{p_u}{\rho_u}) + \Omega^2 r^2)^{\frac{1}{2}} \tag{132d}$$

Determination of the total internal energy follows from the total enthalpy, pressure and density by definition, c.f. Equation (26).

(e) Slipstream Solution Algorithm - The solution at a slipstream point is given by:

$$\log p_\ell = \log p_u = \log p = \frac{a_a \log p_a + a_d \log p_d - \gamma(\bar{v}_a - \bar{v}_d) - \gamma((aQ_1+Q_2)_a + (aQ_1-Q_2)_d)\Delta t}{(a_a+a_d)} \tag{133}$$

$$\bar{v}_\ell = \bar{v}_u = \bar{v} = \frac{1}{2}\left(\bar{v}_a + \bar{v}_d + \left(\frac{a_a - a_d}{\gamma}\right) \log p - \frac{a_a}{\gamma} \log p_a + \frac{a_d}{\gamma} \log p_d + ((aQ_1+Q_2)_a - (aQ_1-Q_2)_d)\,\Delta t\right) \tag{134}$$

$$S_\ell = S_b \quad \text{or} \quad \rho_\ell = \rho_b\,(p/p_b)^{1/\gamma} \tag{135a}$$

$$S_u = S_e \quad \text{or} \quad \rho_u = \rho_e\,(p/p_e)^{1/\gamma} \tag{135b}$$

$$H'_\ell = H'_b + \frac{2\,(p-p_q)}{(\rho_\ell + \rho_{\ell_q})} \tag{136a}$$

$$\bar{q}_\ell = \left(2\left(H'_\ell - \frac{\gamma}{\gamma-1}\,\frac{p}{\rho_\ell}\right) + \Omega^2 r^2\right)^{\frac{1}{2}} \tag{136b}$$

$$H'_u = H'_e + \frac{2\,(p-p_q)}{(\rho_u - \rho_{u_q})} \tag{136c}$$

$$\bar{q}_u = \left(2\left(H'_u - \frac{\gamma}{\gamma-1}\,\frac{p}{\rho_u}\right) + \Omega^2 r^2\right)^{\frac{1}{2}} \tag{136d}$$

$$\bar{u}_\ell = (\bar{q}_\ell^2 - \bar{v}_\ell^2)^{\frac{1}{2}} \tag{137a}$$

$$\bar{u}_u = (\bar{q}_u^2 - \bar{v}_u^2)^{\frac{1}{2}} \tag{137b}$$

The overall procedure for imposing the boundary conditions along the blade surface and slipstream points is shown schematically in Figure (8). The time axis projects vertically out of the page in this figure. The dashed lines represent the intersections of the reference planes and of the stream path with the axisymmetric stream surface (i.e., the x,y plane) during a time step Δt

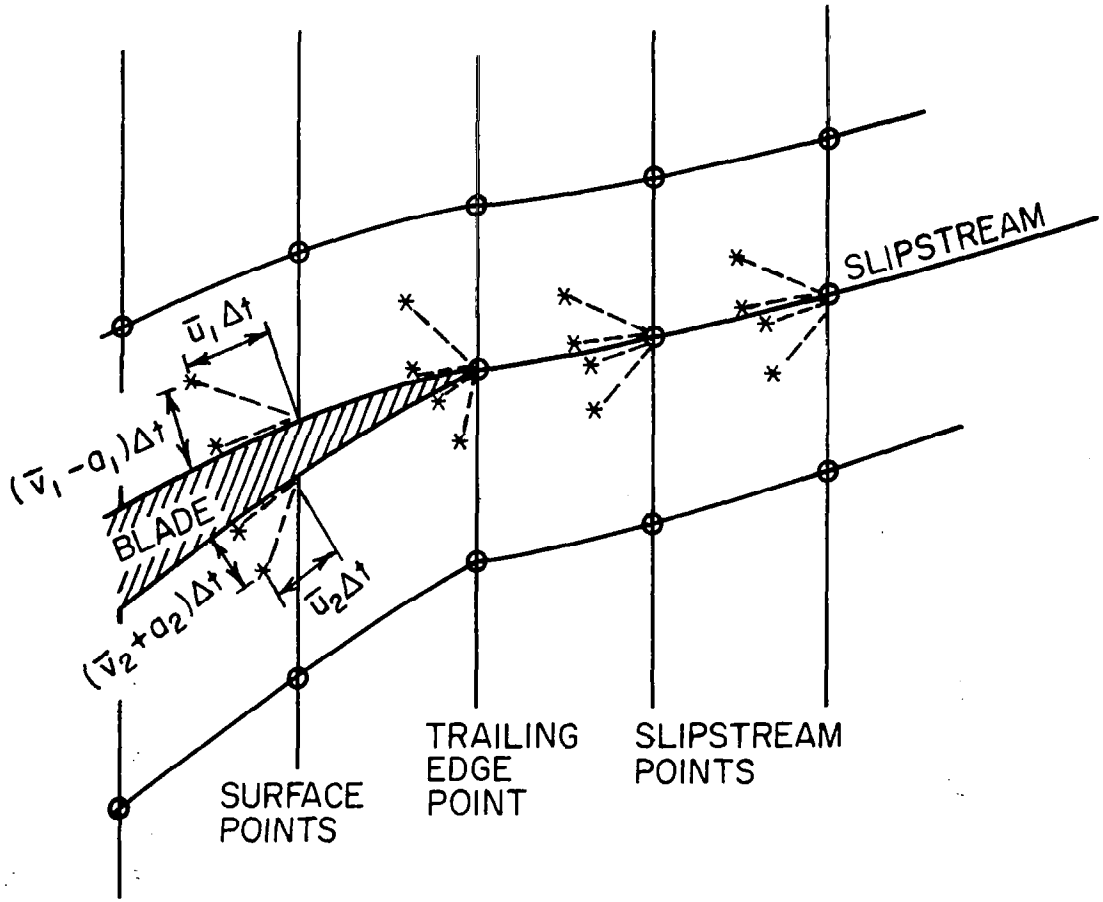

FIGURE 8. COMPARISON OF BLADE AND SLIPSTREAM CHARACTERISTIC SYSTEM

(neglecting the motion of the slipstream during the interval Δt). The values obtained for $\bar{v}$ on the slipstream are used to locate the new position of the slipstream for the next time step as follows:

$$x_n = x_o - (\bar{v}\sin\phi) \Delta t \tag{138}$$

$$y_n = y_o + (\bar{v}\cos\phi) \Delta t \tag{139}$$

where $(x_o, y_o (x_o,t))$ are the coordinates of the slipstream point at which the above described solution is obtained, and (x_n, y_n) are its new coordinates. Linear interpolation is then used to find the new y coordinate, $y_o (x_o, t+\Delta t)$ of the intersection of the slipstream and the grid column located at $x=x_o$, which gives the new coordinates of the slipstream grid point at the next time step.

(f) Trailing Edge and Leading Edge Points - At the trailing edge, the system given by Equations (129) through (132) is applicable subject to the constraint that $p_\ell=p_u$. This condition is satisfied by iterating the angle ϕ at the trailing edge, which, unlike the general blade surface and slipstream points, is not known a priori. The blade trailing edge is assumed to be sharp, but not necessarily cusped; the angle ϕ is taken as a weighted combination of the blade surface angle and the slipstream angle, as shown schematically at points A and B in Figure (9a).

$$\phi_{TE} = k_{TE}\phi_{slipstream} + (1-k_{TE}) \phi_{surface} \tag{140}$$

(Values of k_{TE} in the range $\frac{1}{2} \leq k_{TE} \leq \frac{2}{3}$ have been found to provide satisfactory accuracy and stability of the trailing edge point solutions.) Therefore, the trailing edge point solution is carried out at points A and B like any other blade surface point solution, except that the slipstream angle is deflected until equal pressures (to within an error tolerance of 0.0001% of the mean pressure) are obtained on each side of the surface. The trailing edge and the slipstream emanating from it thus can be considered as together forming a continuous deformable surface. Note, however, that one value of ϕ_{TE} will be obtained on the upper surface of the blade and a second value on the lower surface, if the trailing edge itself is not actually cusped. Therefore, the direc-

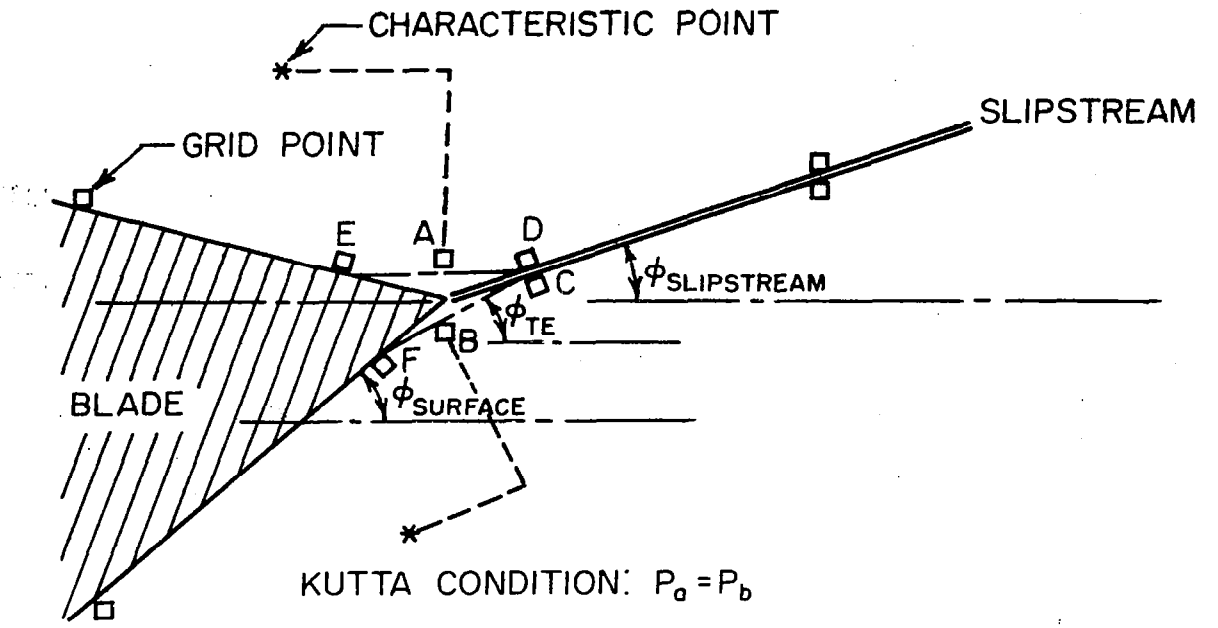

(A) DETAIL OF TRAILING EDGE

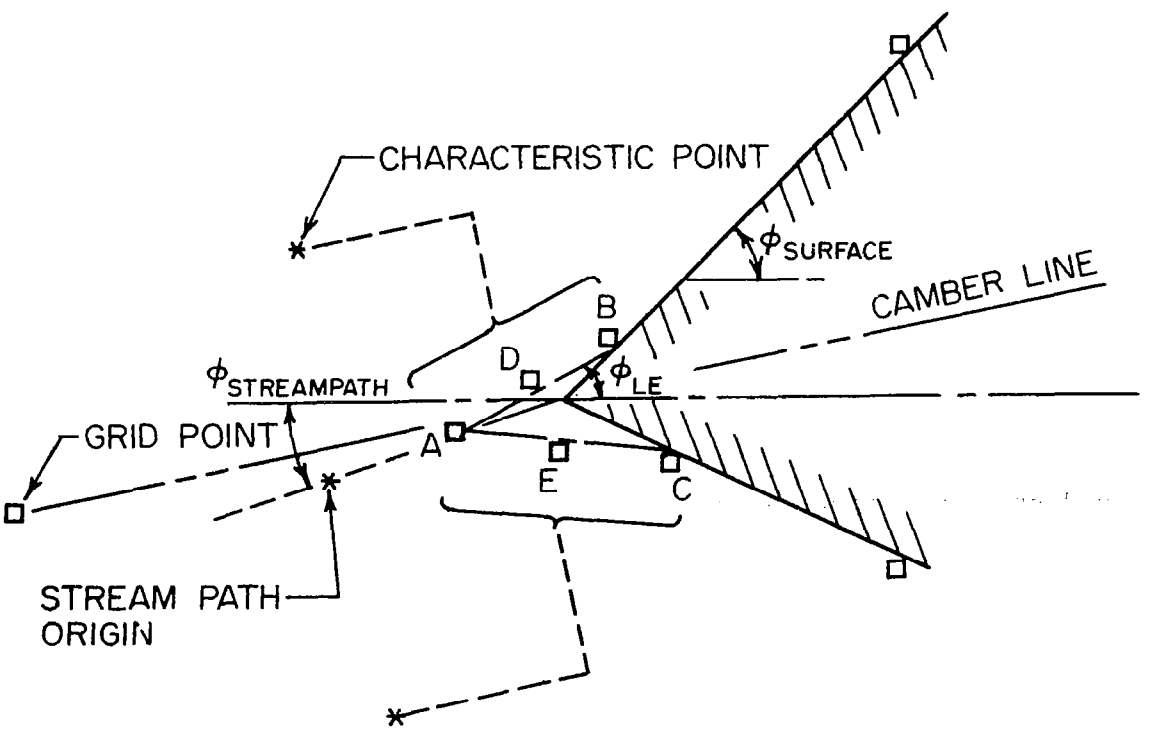

(B) DETAIL OF LEADING EDGE

FIGURE 9. SCHEMATIC OF LEADING AND TRAILING EDGE CONFIGURATIONS

tion of the velocity vector at the trailing edge is multiple-valued. Specifically, 5 values of the flow angle are identified at 6 points having a common location; the trailing edge surface angles at points E and F, the mean angles at points A and B, and the (single) slipstream angle at points C and D. Since the Kutta condition requires the pressure to be continuous at the trailing edge, the change in pressure associated with the angular differences between these 6 points is neglected. Therefore, the solution is carried out at point A as indicated above, and then solutions are defined at points D and E which only differ from that obtained at point A in the direction assigned to the velocity vector. (i.e., the pressure, density and magnitude of the velocity vector at points A, D and E are equal. The directions of the velocity vectors are parallel to the angle of each of these 3 points.) The same procedure is used to carry out the solutions at points B, C and F. Note that velocity vectors obtained at points C and D are, therefore, parallel but can differ in magnitude. The solutions at points A and B are used in the computations at interior points directly above and below the trailing edge, whereas the solutions at C and D are used to determine the slipstream point solutions downstream of the trailing edge, and those at points E and F are used to carry out solutions at the blade surface points upstream of the trailing edge.

The leading edge configuration is sketched in Figure (9b). In view of the singular character of a sharp leading edge, a somewhat more complex solution procedure than employed at the trailing edge is necessary. A total of five flow angles, and a corresponding number of solutions, are again identified at the leading edge. With reference to Figure (9b), the points A, B, C, D and E are all located at the same physical position, however, the flow angle at point A is the angle of the stream path intersecting the leading edge, and the flow angles at points B and C are a weighted combination of the surface angles of the upper and lower surfaces, respectively, and the stream path angle:

$$\phi_{LE} = k_{LE} \; \phi_{surface} + (1-k_{LE}) \; \phi_{stream\ path} \tag{141}$$

(A value of $k_{LE} = 1.0$, which makes the flow angles at points B and C tangent to the actual blade surface angles, has been found to be satisfactory for very

slender blades, but $k_{LE}<1.0$ may be appropriate for other cases). The flow angles at points D and E are the mean of ϕ_{LE} and $\phi_{stream\ path}$.

The leading edge solution procedure is begun by varying the stream path angle until the pressures at point A obtained from Equation (130a) and (130b) are matched (to within an error tolerance of 0.0001% of the mean pressure). As part of this step, the instantaneous locations of the origins of the stream path and the wave characteristics intersecting the leading edge are determined. The solution at point A is then completed using Equations (129),(131) and (132) in the same fashion as employed at any blade surface point. Note that a single-valued solution will be obtained at point A. Next, pressures at points B and C are obtained from Equations (130a) and (130b) using the specified angles at these points (from Equation 141). Since points B and C are, in fact, coincident with point A, the solutions must have the same entropies* at any instant. The total enthalpies are determined from Equations (132a) and (132c). Therefore, the densities and velocities at these points are found from the equation of state, the definition of total enthalpy and the specified angles. Finally, solutions at points D and E are obtained by averaging the pressure and magnitudes of the velocity vectors at points A and B and at points A and C, respectively. The directions of the velocity vectors are also averaged. The densities at these points are then calculated from the entropy at point A.

Summarizing, at the leading edge a single value of the entropy and total enthalpy is obtained, but five values of the pressure, density and velocity vector are determined. The solution obtained at point A in Figure (9b) is subsequently used in computations at the interior grid point upstream of point A. The solutions at points B and C are used for the adjacent blade surface points on the upper and lower surfaces, respectively. The solution at point D is used in computations at the interior point above the leading edge, and that at point E for the interior point below the leading edge.

---

*The possible existence of a shock wave at this point due to the flow deflection is neglected in this connection. The oblique shock entropy increase could, of course, be computed, if appropriate, by suitable modification of the code.

(g) Intersection of Slipstream and Discharge Boundary - Finally, special consideration must be given to the grid points at the intersections of the slipstreams and the discharge boundary, since these grid points lie on two boundaries of the computational domain. It should be emphasized in regard to these points that all the characteristic points (A, B, D and E in Figure 7) which influence a slipstream point (0 in Figure 7) lie upstream of the subject point (assuming $\bar{u} > 0$). The numerical domain of dependence of a slipstream point, therefore, extends to the adjacent grid points only through the linear interpolations necessary to evaluate variables and derivatives at the characteristic points. This dependence represents the only mechanism by which those slipstream points which lie on the discharge boundary are affected by the discharge boundary conditions that are explicitly enforced at all other discharge boundary points.

In connection with these same special slipstream points, it should be pointed out that if the slipstream angle ϕ at the discharge boundary becomes sufficiently large (i.e., the included angle between the slipstream and discharge boundary is sufficiently acute) it is possible for the characteristic point to be located outside the computational domain. The physical meaning of this occurrence is that the slipstream solution explicitly depends on data downstream of the discharge boundary and, therefore, the boundaries of the computational domain do not encompass the numerical domain of dependence of the solution. Theoretically, this condition represents a limitation on the applicability of the present formulation. In practice, it represents an extreme condition which has thus far only been encountered during transient phases of a solution; use of linear extrapolation of data from the set of grid points adjacent to the discharge boundary to the characteristic point has proven successful in these instances, although it temporarily violates the CFL convergence criterion.

Periodicity Condition

In the analysis of an isolated circular (or infinite) cascade of blades in a uniform free stream, it is clear that the solution for each blade-to-blade passage will be identical. The solution for the complete cascade in this case will be steady (in the frame of reference of the blades) and have an angular period of $2\pi/N$. Enforcement of this periodicity condition is straight-

forward; the solution on the exterior grid rows k=1, 2 and 3 (see Figure 5) can be equated to those on interior grid rows KS-2, KS-1 and KS, and those on exterior rows k=KS+1, KS+2 and KS+3 can be equated to those on interior rows k=4, 5 and 6. It may be noted that in domains 1 and 2, grid rows 1 and 3 and KS+1 and KS+3 are superfluous, since the lateral boundaries of these domains are in reality composed of ordinary interior points. However, the solutions on grid rows 1, 2 and 3 and KS+1, KS+2 and KS+3 are required to carry out the slipstream point solutions in domains 4, 6 and 7 as well as the blade leading and trailing edge point solutions. (Compare Figures 5 and 8.)

In the more general case of a stage composed of interacting blade rows having unequal numbers of blades, the fundamental angular period of the complete cascade solution is $2\pi/\Delta N$, where ΔN is the difference in the number of blades. Furthermore, the flow pattern rotates with an angular velocity which is, in general, a multiple of the wheel speed.[11] (In the special case of an equal number of blades the flow pattern rotates at "infinite" speed and the angular period $2\pi/N$ is recovered.) Numerical representation of the periodicity condition pertaining to the conventional configuration, consisting of a pair of blade rows with the larger number of blades in the second row, has been accomplished by formulation of a cyclic procedure for equating the solution on the exterior grid rows identified above (i.e., k=1, 2, 3 and KS+1, KS+2, KS+3) to that on corresponding interior rows (i.e., k=KS-2, KS-1, KS and 4, 5, 6) at an earlier time through a set of appropriate phase relations. The same procedure is applied on the grid columns at the interface between domains 4 and 5.

An illustration of the nature of the cyclic procedure devised to enforce the periodicity of the solution can be accomplished through use of the following simplified configuration. Consider first a stage having three rotor blades and three stator blades. For the present discussion, let the stator precede the rotor. This configuration is shown in Figure (10a) in both axial and cascade projections. At time t_o all rotor and stator blades are aligned, whereas at time $t_o+\Delta t$ the rotor has moved through a fraction of a revolution, and none of the blades are now aligned. It is clear in this case that the geometric boundary conditions (which determine the angular periodicity of the flow through the stage) are identical in each blade-to-blade passage at any time. Accordingly, the flow field in each passage should be identical, since none of the boundary

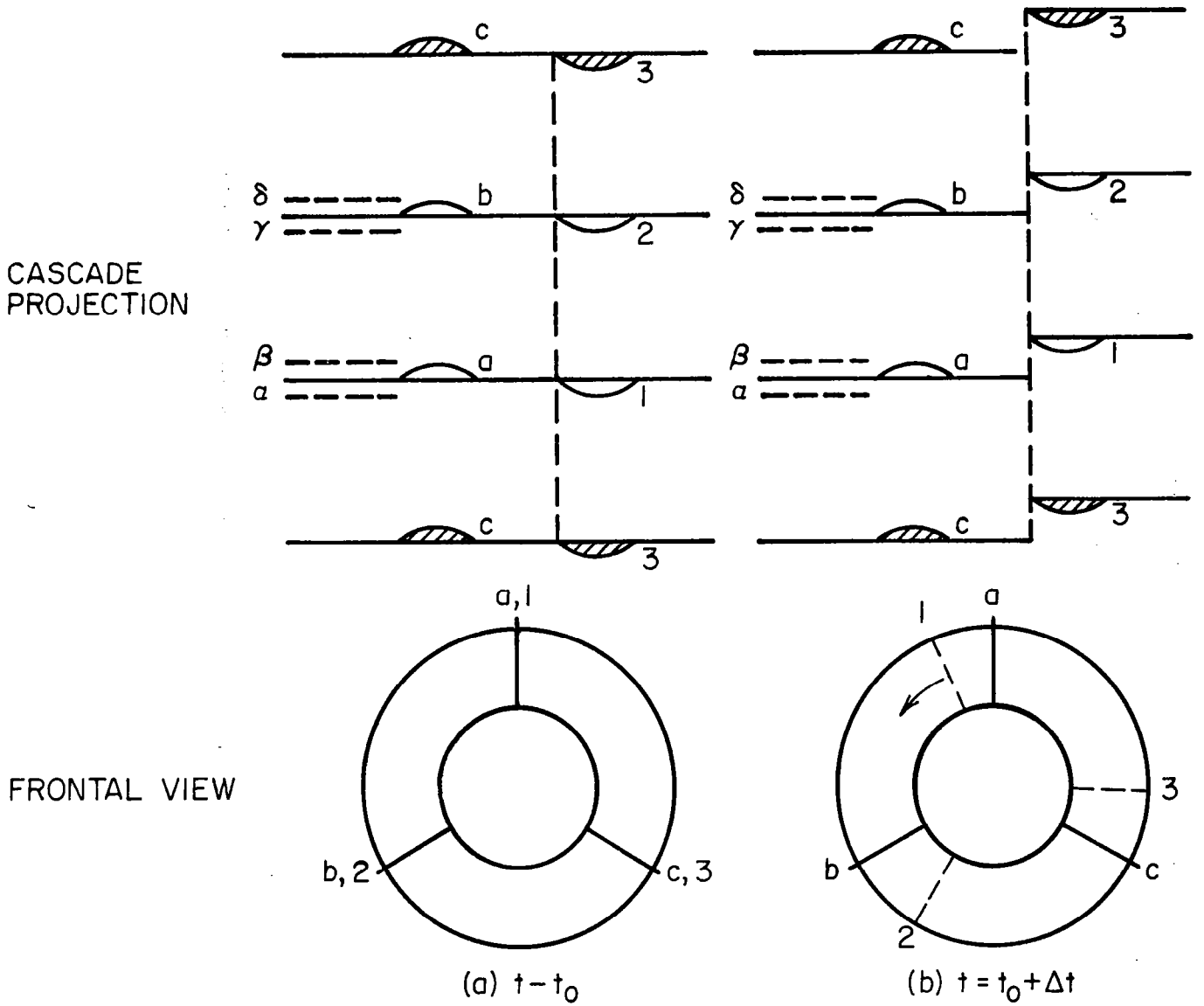

FIGURE 10a. ILLUSTRATION OF CYCLIC ALGORITHM FOR STAGE WITH EQUAL NUMBER OF BLADES IN STATOR AND ROTOR ($N_1 = 3$, $N_2 = 3$)

conditions distinguish one passage from the next. In this case the solution along an exterior grid row δ can be equated to that along the interior grid line β and similarly that along exterior line α can be equated to that along interior line γ, at any instant. Consider now the case with three blades in the stator and four blades in the rotor as shown in Figure (10b). At time t_o rotor blade 2 is aligned with stator blade b, whereas at time $t_o+\Delta t$ rotor blade 3 is aligned with blade c. In this case the geometric conditions pertaining to the passage between blades a and b are obviously different from those for the passage between blades b and c at any time. However, it may be noted that those pertaining to passage bc at $t_o+\Delta t$ are precisely the same as those which pertained to passage ab at the previous time t_o. Therefore, the flow conditions along exterior grid line δ at time $t_o+\Delta t$ can be equated to those along interior grid line β at the earlier time t_o. However, in this case those along exterior grid line α at time $t_o+\Delta t$ cannot be equated to those occurring in passage ab at time t_o, but must be equated to those occurring along line γ at an earlier time. Thus, a phase shift is introduced in application of the lateral boundary conditions.

A similar procedure is used to define boundary values along the interface between domains 4 and 5. However, in this connection it is pointed out that sufficient data must be stored along this interface to provide information for a maximum period corresponding to the blade passing frequency of the first row (i.e., the row with the smaller number of blades). During this period the relative angular positions of the two domains will shift by $2\pi/N_1$. In addition, domain 4 will itself span an arc of $2\pi/N_1$; therefore data covering a total arc of $2(2\pi/N_1)$ must be available. The boundary data is stored for one blade-to-blade passage on either side of the central passage which forms the computational domain, i.e., a total of three passages. Thus, for domain 5 the stored data spans the arc $3(2\pi/N_2)$. An upper limit on the ratio of number of blades results, namely: $3/N_2 \geq 2/N_1$ is required. The permissible number of blades in the second row is, therefore, bounded by:

$$1 \leq \frac{N_2}{N_1} \leq \frac{3}{2} \tag{142}$$

The high speed fan configurations to be considered later in this report have stator to rotor ratios of the order of 1.05 and 1.12, which are within these

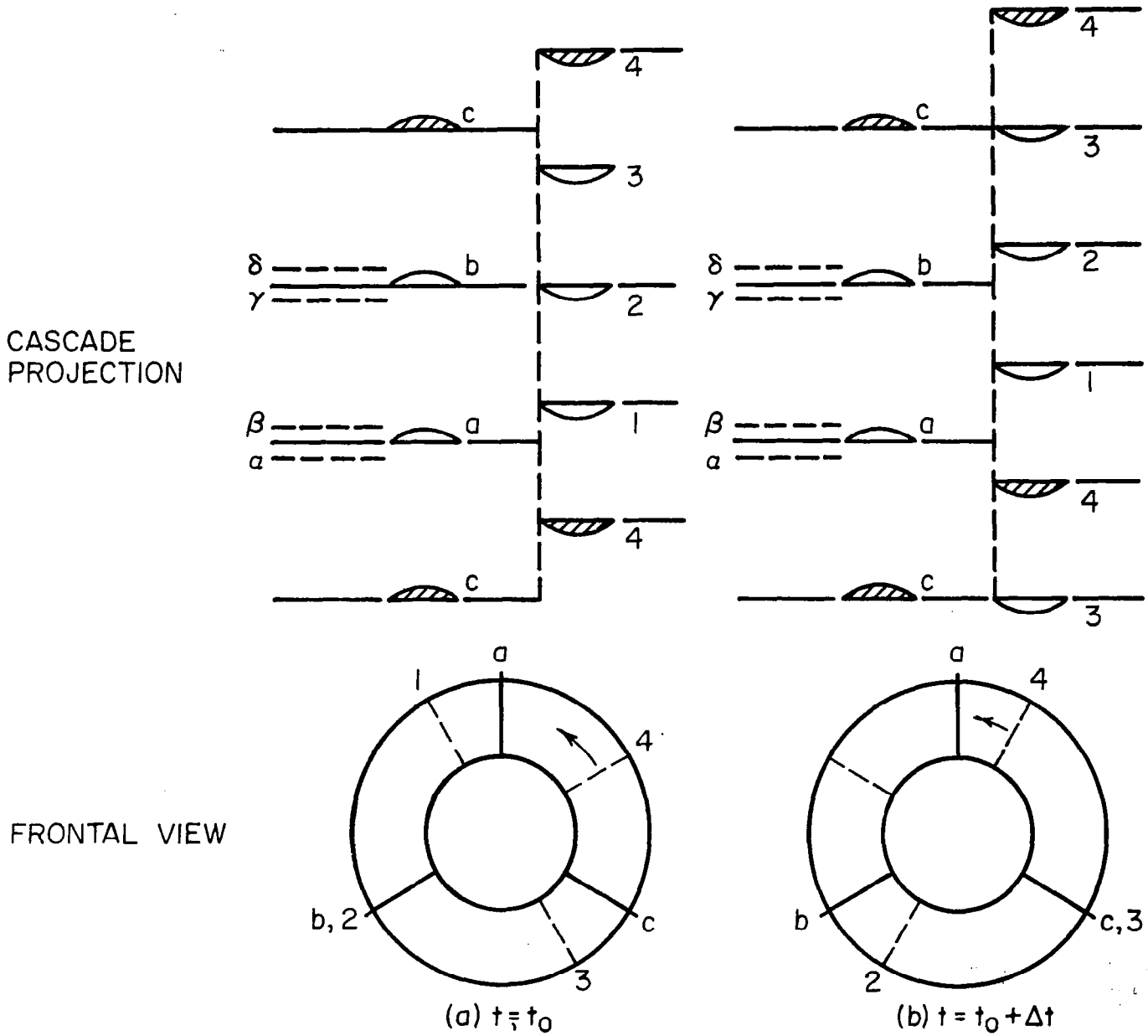

FIGURE 10b. ILLUSTRATION OF CYCLIC ALGORITHM FOR STAGE WITH UNEQUAL NUMBER OF BLADES IN STATOR AND ROTOR ($N_1 = 3$, $N_2 = 4$)

limits. Should the upper limit prove restrictive for other configurations, the stored boundary data for the interface of domain 5 with domain 4 could be extended to span an arc $5(2\pi/N_2)$, for example, by including two passages on either side of the central passage, which would increase the upper limit to $N_2/N_1 \leq 5/2$. Some modification of the computer program described in Volume II of this report would, however, be required.

A more detailed exposition of the development and application of the phased boundary conditions is contained in Appendix I of this report. In particular, it is demonstrated that the required boundary information from adjacent blade-to-blade passages is generated as one passage of the first row crosses one blade of the second row, and that the desired periodicity is attained asymptotically in time.

Initial Conditions

The initial conditions need be considered only to the extent that they bear on the asymptotic limit in time, since only the asymptotic solution is of interest. Several observations relative to this point should be emphasized:

(a) The initial data is necessarily approximate, at best, since determination of the exact solution is the objective of the calculation. The initial transient solution is associated with the difference between the initial data and the exact solution, and consequently the time needed to attain an asymptotic solution may be expected to diminish as the accuracy of the initial data is improved.

(b) The initial data can be approximate in the sense that it does not satisfy the boundary conditions, or it does not satisfy the governing equations, or both. If the initial data does not satisfy the governing equations, the resulting transient solution has no physical relevance; only the asymptotic limit is meaningful. On the other hand, if the initial data satisfies the governing equations but does not satisfy the imposed boundary conditions (i.e., it satisfies some other set of boundary conditions) then the resulting transient solution is physically relevant; it represents the response of the system to an impulsive change in boundary conditions. The computer program has not

been structured to handle such impulsive changes in boundary conditions, but the ability of the formulation to do so is simply pointed out.

(c) As a consequence of the present formulation of inlet and discharge boundary conditions, existence of an asymptotic solution for arbitrary initial data or for arbitrary boundary conditions cannot be guaranteed. Obviously, it is possible to specify inconsistent boundary conditions, such as an unattainably high pressure ratio across a stage, or initial data that generate a transient solution which violates certain underlying assumptions, such as $u > 0$ at the inlet and discharge station. An asymptotic solution cannot be attained in such cases (i.e., the computer program "bombs"). However, this problem should not be any more disturbing than the failure to reach a stable operating point in an actual turbomachine due to surge, for example. In the present formulation, possible non-existence of an asymptotic solution is the penalty incurred by modelling as closely as possible the actual wave mechanics of the inlet and discharge flows without modelling the entire starting process by which a stable operating point is reached. On the other hand, if existence of an asymptotic solution is demonstrated for a particular set of boundary conditions and initial data, then uniqueness of the numerical solution necessarily follows. If it were non-unique, the numerical solution would drift through an endless succession of states, since each time step is a new initial value problem with a perturbation of the data provided by the round-off error. In other words, convergence of the solution guarantees its uniqueness.

(d) It should be apparent from the preceding discussion that the initial data can bear on the existence of an asymptotic solution, but the extent to which an asymptotic solution depends on the initial data is more difficult to define. It is conjectured here, on the basis of experience thus far, that variations in the initial data within those bounds for which a solution exists have no effect on the asymptotic solution. It is clear that the solution at any instant during the transient oscillation through which the flow proceeds can be regarded as an initial condition leading to the same asymptotic solution. Although this is not a conclusive proof of the conjecture, it tends to support the limited observations on which the conjecture is based. In connection with this same question, it should be recognized that application of the inlet and discharge boundary conditions formulated herein to a duct

flow without any turbomachinery would not be sufficient to define a unique solution, as is frequently the case in inviscid flow problems. An infinity of solutions, ranging from no flow to choked flow, could satisfy the imposed boundary conditions, and only the initial data would determine which solution (if any) would be obtained. It is the addition of the rotating blade row and the application of a Kutta condition to each airfoil which provides the additional constraint that defines a unique solution. From this viewpoint, the role of initial conditions should be irrelevant, as long as a solution can be obtained.

In the present formulation, initial conditions can be specified in either of two ways. If no previous information is available (a "cold start"), the initial data for the entire computational domain is approximated from the inlet and discharge boundary conditions, (supplemented by $u_{-\infty}$ in the open duct case) and an initial value of the swirl angle, $\tan^{-1} v/u$, at the inlet. In this case the inlet pressure and entropy are imposed in the domains preceding the rotor. The density is computed from the equation of state and the meridional velocity from the inlet mass flow rate $(\rho u 2\pi rb)_{-\infty}$. The circumferential velocity component is approximated by maintaining the inlet value of the tangent of the swirl angle, (v/u), throughout these domains. Within the rotor, a linear increase in pressure from the inlet value at the leading edge station to the discharge value at the trailing edge station is assumed. An entropy gradient may also be imposed across the rotor corresponding to anticipated shock losses. Downstream of the rotor, the pressure and entropy obtained at the rotor trailing edge station are assumed to prevail. The density and meridional velocity are again obtained from the equations of state and inlet mass flow rate, respectively. Downstream of either blade row, the slipstream is assumed to lie on a continuation of the trailing edge camber line, and the circumferential velocity component is approximated from the slipstream angle rather than the inlet swirl angle. The blade surface and slipstream point routines are then activated for one time step to satisfy the boundary conditions on these surfaces.

If a previous solution, employing the same grid structure, is available (i.e., a "restart") it may be used as initial data, with either the same or

revised boundary conditions.* However care must be exercised in this regard when carrying out a computation using the phased boundary conditions. The elapsed time must always be measured from the "cold start" since the cyclic procedure uses stored boundary data which is identified by a time counter that cannot be altered when "restarting" the computation.

Finally, it is pointed out that an initial transient solution which is physically irrelevant can excite slipstream oscillations which are sufficiently violent to abort the computation. Therefore, provision has been included to utilize a "small disturbance" type slipstream approximation during the initial transient phase. In this case, the slipstream point algorithm is carried out in its entirety, but the resulting solution is applied on the original slipstream contour, which is held fixed. The computation of the slipstream motion can be restored after the initial transient phase of the interior solution has decayed. This option can be regarded as a "two phase" initialization procedure.

BOUNDARY LAYER AND WAKE ANALYSIS

Motivation and Approach

The requirement for evaluation of viscous effects in compressors and/or fans arises from a number of sources: (a) the displacement effect of the boundary layers on the blades, and on the hub and casing walls constricts the inviscid flow area and thereby alters the inviscid solution, (b) the viscous drag is largely responsible for the loss of total pressure through the stage (in a shock-free flow it is solely responsible), (c) passage of one blade row through the wakes of a preceding row contributes significantly to the unsteady lift of the second row and the associated acoustic properties of the stage, and (d) in the extreme, the inviscid portion of the flow is entirely engulfed by turbulent eddies. In the last case, the physical and mathematical character of the flow is fundamentally changed, and the analytical model must be reformulated accordingly. In the present approach, as described in the preceding section, it is assumed that the flow is predominantly inviscid, and viscous ef-

*Details of these procedures are contained in Volume II of this report. Note that the stored data is the non-dimensional form defined by Equation (49).

fects can be modelled by standard boundary layer theory. Thus, the situations in which viscous effects predominate (i.e., separation or fully turbulent flow) are excluded. However, approximate representation of the first three effects noted above is incorporated in the present model.

The displacement interaction between boundary layer and inviscid flow under steady conditions has been, and remains, a subject of extensive research. Practical computational methods which are applicable when separation (i.e., flow reversal within the boundary layer) occurs have not been firmly established as yet. A less satisfactory situation exists in an unsteady interaction, for which even the definition of separation is not universally agreed upon. Unfortunately, the pressure gradients in compressors are usually adverse and, therefore, separation is a significant problem.

The intent of the present effort is to provide only an approximation to the boundary layer displacement effect on the blade surfaces; therefore recourse is made to standard steady boundary layer representations based on zero pressure gradient and local similarity concepts with heuristic corrections to account for regions of separated flow. If separation is indicated on this basis, a more detailed analysis of the boundary layer is clearly required.

Quasi-Steady Approximations

The use of steady boundary layer representations implies that either the anticipated time scale for variations in the inviscid flow is much larger than the characteristic boundary layer response time, or that the anticipated unsteady components of the viscous flow solution are small compared to the steady components. The first condition can be examined by comparing the time for a diffusion wave to traverse the thickness of the boundary layer with the period between rotor blade passings. The speed of a diffusion wave is of the order $\mu/(\rho\delta)$ and hence the time to traverse the boundary layer is of the order $\delta^2\rho/\mu$. Therefore, the first condition requires:

$$\rho \frac{\delta^2}{\mu} << \frac{2\pi}{N\Omega} \tag{143}$$

The maximum boundary layer thickness is on the order of

$$\frac{\delta}{c} = \begin{cases} 5\ R^{-1/2} & \text{laminar} \\ \\ \frac{1}{3}\ R^{-1/5} & \text{turbulent} \end{cases} \tag{144}$$

where $R = \rho uc/\mu$ is a Reynolds number based on chord length and characteristic (mean) values of velocity, density and viscosity in the inviscid flow. Therefore, Equation (143) becomes:

$$\left(\frac{2\pi}{N}\right) \left(\frac{u}{\Omega r}\right) \left(\frac{r}{c}\right) >> \begin{cases} 25 & \text{laminar} \\ \\ \frac{1}{9}\ R^{3/5} & \text{turbulent} \end{cases} \tag{145}$$

(The laminar value is only included for the sake of comparison; a turbulent boundary layer is expected to prevail over most of the blade under typical operating conditions.)

Typical values of the parameters appearing in Equation (145) are of the order of $2\pi/N \simeq 1/10$, $u/\Omega r \simeq 1$ and $r/c \simeq 10$. Therefore, the required inequality is not generally satisfied; i.e., the response time of the boundary layer is longer than the period between blade passings. Consequently, justification of the assumption of a quasi-steady viscous solution must be predicated on existence of relatively small amplitude unsteady disturbances in the inviscid flow. Thus, it is consistent with use of acoustic or linearized inviscid flow theory, but not necessarily consistent with the present use of nonlinear theory. The possible requirement for an unsteady viscous flow analysis to correctly represent the viscous-inviscid interactions in rotating turbomachinery should be recognized.

Blade Boundary Layer Displacement Thickness and Shear Stress

(a) Basic Equations - In the present context, the principal interest in the boundary layer solution resides in determination of the displacement effect

on the blade surfaces and the initial conditions for the wakes which emanate from the trailing edges. Therefore, the well known momentum integral equation (cf., Reference 15, Chapter VIII) is adequate to provide the required information:

$$\frac{d\theta}{d\bar{x}} = \frac{\tau_o}{\rho \bar{u}_e^2} + \frac{1}{\bar{u}_e} \frac{d\bar{u}_e}{d\bar{x}} [2\theta + \delta^*] \tag{146}$$

where $\bar{x}$ is the distance along the blade surface measured from the leading edge, $\bar{u}_e$ refers to the magnitude of the velocity vector in the inviscid flow at the blade surface (in the frame of reference of the blade row), ρ is the corresponding density, and density variations within the boundary layer as well as the effects of variable stream sheet thickness and radius are neglected. The shear stress, displacement thickness and momentum thickness are defined by:

$$\tau_o = \mu \left(\frac{\partial u}{\partial y}\right)_{y=o} \tag{147}$$

$$\delta^* = \int_o^\delta \left(1 - \frac{\bar{u}}{\bar{u}_e}\right) d\bar{y} \tag{148}$$

$$\theta = \int_o^\delta \frac{\bar{u}}{\bar{u}_e} \left(1 - \frac{\bar{u}}{\bar{u}_e}\right) d\bar{y} \tag{149}$$

where $\bar{u}$ is the velocity within the boundary layer. As will be shown below Equation (146) can be transformed to the following form for both laminar and turbulent boundary layers:

$$\frac{d\delta^*}{d\bar{x}} = AR^{-B} \tag{150}$$

where the parameters A and B are approximate functions of the shape factor, δ^*/θ, pressure gradient, Reynolds number, etc., which will be derived below. Numerical integration of Equation (150) by the simple Euler formula provides the displacement thickness at the grid points spanning the blade surface:

$$\delta^*_{j+1} = \delta^*_j + (AR^{-B})_j \quad \Delta\bar{x} \tag{151}$$

Integration is begun midway between the leading edge and the first surface point to avoid the singularity at the leading edge ($\bar{x} = 0$). Evaluation of the shear stress is outlined below.

(b) Laminar Flow - The solutions of the Falkner-Skan equation[16], i.e.,

$$f''' + ff'' + \beta(1-f'^2) = 0 \tag{152}$$

derived by Hartree[17] (cf. Reference 18 for a complete derivation and discussion of this equation) form the basis of the laminar flow approximations which are utilized up to the transition point. In this case

$$f = f(\eta) \tag{153}$$

$$\eta = \bar{y} \left(\frac{m+1}{2} \rho \frac{\bar{u}_e}{\mu\bar{x}}\right)^{\frac{1}{2}} \tag{154}$$

$$\beta = \frac{2m}{m+1} \tag{155}$$

$$\bar{u} = \bar{u}_e f'(\eta) \tag{156}$$

Accordingly,

$$\tau_o = \bar{u}_e \left(\frac{m+1}{2} \rho \frac{\bar{u}_e}{\mu\bar{x}}\right)^{\frac{1}{2}} f''(o) \tag{157}$$

and, from Equation (146) with $d\bar{u}_e/d\bar{x} = 0$:

$$\frac{d\delta^*}{d\bar{x}} = \frac{\delta^*}{\theta} \left(\frac{m+1}{2}\right)^{\frac{1}{2}} f''(o) \quad R^{-\frac{1}{2}} \tag{158}$$

Therefore, by comparison with Equation (150), the values of A and B for a laminar flow are identified as

$$A = \frac{\delta^*}{\theta} \left(\frac{m+1}{2}\right)^{\frac{1}{2}} f''(o) \tag{159}$$

$$B = 1/2 \tag{160}$$

The values of δ^*/θ and $f''(o)$ obtained from the Hartree solutions have been curve-fit as a function of the pressure gradient parameter β for the attached flow branch, $\beta \geq -.1988$:

$$\frac{\delta^*}{\theta} = 2.16 + 1.86 \exp(-7.367 (\beta + 0.1988)) \tag{161}$$

$$f''(o) = 0.79 (\beta + .1988)^{.525} \tag{162}$$

Separated flow solutions are obtained for $\beta < -.1988$. For this case $\delta^* \to \infty$ and $f''(o) < 0$. The condition

$$\frac{\delta^*}{\theta} f''(o) = 0.0 \tag{163}$$

is used to permit continuation of the integration of Equation (150) through the separation region. However, the result should be viewed with caution if separation is indicated, as a more detailed viscous solution is required for this case.

(c) Transition - The criterion for transition from laminar to turbulent flow is based on a study by Pretsch[18] described in Reference (15), Chapter XVII. Transition is considered to occur when:

$$R_{\delta^*} > R_{\delta^*_{critical}} \tag{164}$$

where $R_{\delta^*} = \rho u \delta^*/\mu$. The critical Reynolds number is defined by:

$$R_{\delta^*_{critical}} = \begin{cases} 60 & \text{for} \quad \beta < -.1988 \\ 60 + 600 \left(1 + \frac{\beta}{.1988}\right) & \text{for} \quad -.1988 \leq \beta < 0 \\ 660 + 12000\beta & \text{for} \quad \beta \geq 0 \end{cases} \tag{165}$$

(d) Turbulent Flow - A power-law velocity profile is assumed to be descriptive of the turbulent boundary layer (cf. Reference 15):

$$\frac{\bar{u}}{\bar{u}_e} = \left(\frac{\bar{y}}{\delta}\right)^{1/n} \qquad (\bar{y} \leq \delta) \tag{166}$$

In this case

$$\delta^* = \frac{\delta}{1+n} \tag{167}$$

$$\theta = \frac{\delta n}{(1+n)\ (2+n)} \tag{168}$$

This type profile was experimentally derived for pipe flows by Nikuradse[19], for which the corresponding shear stress law was proposed by Schlicting (Reference 15, Chapter XX):

$$\tau_o = \rho \bar{u}_e^2 \ .0225 \ R_\delta^{\frac{1}{4}} \tag{169}$$

where $R_\delta = \rho u \delta / \mu$. Substitution of these results into Equation (146) with $d\bar{u}_e/d\bar{x} = 0$ produces Equation (150), with the following values of A and B for turbulent flows:

$$A = \left(\frac{0.8}{n+1}\right) \left[\frac{0.028\ (1+n)\ (2+n)}{n}\right]^{0.8} \tag{170}$$

$$B = 0.2 \tag{171}$$

The following empirical correlations of the exponent n and factor B have been developed to extend the applicability of this result over the range of Reynolds numbers and pressure gradient effects discussed by Schlicting (Reference 15, Chapter XXI and XXII):

$$n' = \begin{cases} 2.183677 + .573308 \log R - .0136455\ (\log R)^2 & \text{for } R < 1.7\times10^6 \\ 7.6 \quad \text{for} \quad R \geq 1.7\times10^6 \end{cases} \tag{172}$$

$$n = \begin{cases} 2 + (n' - 2) \exp \left[\frac{Lp_{\bar{x}}}{\Delta p} \log \left(\frac{n' - 3}{n' - 2}\right)\right] & \text{for} \quad p_{\bar{x}} \geq 0 \\ 2n' - \left[2 + (n' - 2) \exp \left[- \frac{Lp_{\bar{x}}}{\Delta p} \log \left(\frac{n' - 3}{n' - 2}\right)\right]\right] & \text{for} \quad p_{\bar{x}} < 0 \end{cases} \tag{173}$$

$$B = \begin{cases} 0.2 - .061 \exp (R - 1.7\times10^6) & \text{for} \quad R < 1.7\times10^6 \\ 0.139 & \text{for} \quad R \geq 1.7\times10^6 \end{cases} \tag{174}$$

where $p_{\bar{x}} = \partial p/\partial \bar{x}$, L is the reference length used for non-dimensionalization of the inviscid flow, and Δp is the overall static pressure ratio across the stage.

Blade Wakes

The main interest in the wakes of a blade row resides in the reaction of the blades of a succeeding blade row to traversal of each of the wakes of the first row. The reaction is principally that of an airfoil passing through a nonuniform inviscid flow field (i.e., a "gust")[20]. However, the degree of nonuniformity (and the intensity of reaction thereto) depends on the diffusive properties of the viscous flow; the axial distance between blade rows is paramount in this regard. Although further diffusion can occur downstream of the plane of the leading edges of the second row, the identity of the individual wakes of the first blade row will be lost to a large extent after impingement upon the second row. Therefore, in the present program the inviscid slipstreams and viscous wakes of the first blade rows are only calculated up to the plane of the leading edges of the second row, i.e., the interface of domains 4 and 5. At this station the inviscid flow field at the entrance to domain 5 at any instant is considered to be the composite of the inviscid and viscous solutions at the exit of domain 4. In other words, the identity of the individual wakes of the first blade row is lost downstream of this station, but their momentum and energy defects are transferred to the inviscid flow field through definition of circumferential distributions of flow properties at this station which are composites of the inviscid and viscous wake solutions. The manner in which the composite solution is formed is described following the development of the wake solution.

In view of the intended application of the wake solution, greater emphasis has been placed on accurate description of the velocity defect within the wakes than is given to description of the boundary layer velocity profile. Accordingly, a more rigorous theoretical model of the wake has been derived, although it still lies within the framework of a quasi-steady integral method of analysis.

Governing Equations and Boundary Conditions

The standard boundary layer equations are assumed to apply along the blade slipstreams. The $\bar{x}$, $\bar{y}$ coordinate system defined in connection with analysis of the slipstream (Figure 7) forms the present boundary layer coordinate system* which is shown in Figure (11). The governing equations are, therefore, stated as:

$$\frac{\partial \rho \bar{u}}{\partial \bar{x}} + \frac{\partial \rho \bar{v}}{\partial \bar{y}} = - \rho u \left(\frac{1}{A} \frac{dA}{dx}\right) \approx \rho \bar{u}\left(\frac{1}{A} \frac{\partial A}{\partial \bar{x}}\right) \tag{175}$$

$$\frac{\partial}{\partial \bar{x}} (\rho \bar{u}^2 + p) + \frac{\partial}{\partial \bar{y}} (\rho \bar{u}\bar{v}) = \frac{\partial}{\partial \bar{y}} \left(\mu \frac{\partial \bar{u}}{\partial \bar{y}}\right) - \rho \bar{u}^2 \left(\frac{1}{A} \frac{\partial A}{\partial \bar{x}}\right) + \rho \Omega^2 r \frac{dr}{dx} \cos\phi \tag{176}$$

$$\frac{\partial}{\partial \bar{x}} (\rho \bar{u} H') + \frac{\partial}{\partial \bar{y}} (\rho \bar{v} H') = \frac{\partial}{\partial \bar{y}} \left(\mu \frac{\partial H'}{\partial \bar{y}}\right) - \rho \bar{u} H' \left(\frac{1}{A} \frac{\partial A}{\partial \bar{x}}\right) \tag{177}$$

where:

$$\frac{1}{A} \frac{\partial A}{\partial \bar{x}} = \frac{\cos \phi}{A} \frac{dA}{dx} = \cos \phi \left(\frac{1}{r} \frac{dr}{dx} + \frac{1}{b} \frac{db}{dx}\right) \tag{178}$$

$$H' = h + \frac{1}{2} (\bar{u}^2 + \bar{v}^2 - \Omega^2 r^2) \tag{179}$$

All time derivatives have been neglected and the standard boundary layer approximations have been invoked, (e.g., $\bar{v} << \bar{u}$). The Prandtl number $\mu C_p/k$ has been assumed equal to unity. The viscosity coefficient μ can be considered

*In this context $\bar{y}$ denotes an outward normal from the slipstream; thus $\bar{y} = |\bar{y}|$.

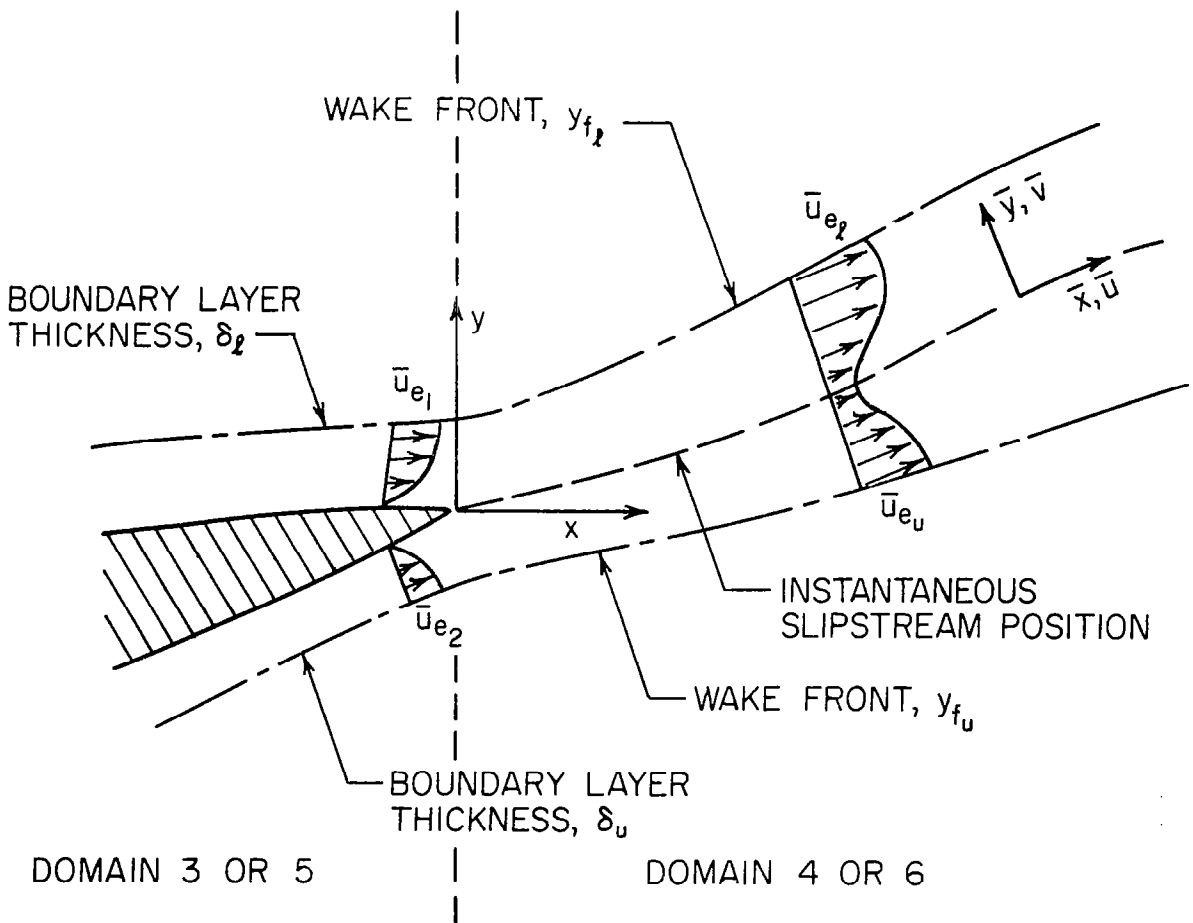

FIGURE 11. SCHEMATIC OF WAKE COORDINATE SYSTEM

to represent either the laminar value associated with molecular diffusion or an effective "eddy viscosity" associated with turbulent motion. In view of the extreme remoteness of the possibility that a laminar flow could exist in the wake of a fan or compressor blade under normal operating conditions in either full-scale flight or a sub-scale test facility, only the turbulent case is considered herein. In this connection, it should be emphasized that the previously noted comparisons of inviscid and viscous time scales should be extended to include the characteristic frequency range of turbulent fluctuations. The present usage of "eddy viscosity" concepts and associated results (derived from experimental observations in steady inviscid flows) is predicated on the assumption that the frequency range of inviscid flow oscillations induced by blade row interactions does not overlap the turbulence frequency range. Consequently, the two unsteady flow phenomena can be uncoupled. This assumption is of course suspect, but its removal requires research into the fundamentals of energy exchange between the inviscid flow and turbulent motion that is well beyond the scope of the present study.

The boundary conditions pertaining to the wakes are summarized as:

At $\bar{y} = 0$:

$$\bar{v} = 0 \tag{180}$$

$$\frac{\partial \bar{u}}{\partial \bar{y}} = \frac{\partial T}{\partial \bar{y}} = 0 \tag{181}$$

At $\bar{y} \to \bar{y}_f$:

$$\bar{u} = (u^2 + v^2)_f^{\frac{1}{2}} \tag{182}$$

$$T = T_f \tag{183}$$

$$\frac{\partial \bar{u}}{\partial \bar{y}} = \frac{\partial T}{\partial \bar{y}} = 0 \tag{184}$$

At $\bar{x} = \bar{x}_{T.E.}$:

$$\delta^*_{wake} = \delta^*_{boundary\ layer} \tag{185}$$

$$\theta_{wake} = \theta_{boundary\ layer} \tag{186}$$

The subscript f denotes the instantaneous inviscid flow values measured at some suitably defined front between the inviscid and viscous flows, which implies $\bar{y}_f < 2\pi r/N$. The boundary conditions for the case when the wakes merge to form a completely viscous flow will be stated in a following paragraph.

The conditions expressed by Equation (181) are approximate, since the wakes will not, in general, develop symmetrically about the slipstream position defined by $\bar{y} = 0$. However, the displacement of the line of minimum velocity and zero normal gradient of velocity from the slipstream position will be neglected. Furthermore, the asymmetric character of the wake, due to the differing boundary conditions which may exist on each side of the wake as $\bar{y} \to \bar{y}_f$, as well as the asymmetry of the boundary layer solutions of the blade trailing edge, will be approximated by using two symmetric solutions; one pertaining to $0 < \bar{y} < \bar{y}_{f,\ell}$ and the other to $0 < \bar{y} < \bar{y}_{f,u}$.

At sufficient distance downstream of the blade row the wakes will entrain the entire inviscid flow field and merge to form a fully turbulent flow. In this event, the boundary conditions given by Equations (182), (183) and (184) are replaced by:

$$\text{At } \bar{y} = \bar{y}_{f,\ell} = \frac{2\pi r}{N} - \bar{y}_{f,u}: \qquad \bar{v} = 0 \tag{187}$$

$$\frac{\partial \bar{u}}{\partial \bar{y}} = \frac{\partial T}{\partial \bar{y}} = 0 \tag{188}$$

The analyses pertaining to independent wakes and merged wakes differ correspondingly as outlined below.

Analysis of Independent Wakes

The method of integral relations[21] is employed using a single strip to cover the region from the wake axis ($\bar{y} = 0$) to the wake front (outer edge) ($\bar{y} = \bar{y}_{f,\ell}$ or $\bar{y}_{f,u}$). This approach is equivalent to use of the Karman momentum integral equation for the boundary layer; however, the surface boundary conditions are replaced by a set of differential equations corresponding to Equations (176) and (177) evaluated at $\bar{y} = 0$, where Equations (180) and (181) pertain:

$$\bar{u}_m \frac{d\bar{u}_m}{d\bar{x}} = - \frac{1}{\rho_m} \frac{dp}{d\bar{x}} + \varepsilon_m \left(\frac{\partial^2 \bar{u}}{\partial \bar{y}^2}\right)_m + \Omega^2 r \frac{dr}{dx} \cos\phi \tag{189}$$

$$\bar{u}_m \frac{dH'_m}{d\bar{x}} = \varepsilon_m \left(\frac{\partial^2 H'}{\partial \bar{y}^2}\right)_m \tag{190}$$

(The subscript m denotes minimum value, which in accord with the assumption of symmetry occurs at $\bar{y} = 0$.)

The integral form of the continuity equation results from multiplication of Equation (175) by $d\bar{y}$ and integration from $\bar{y} = 0$ to $\bar{y} = \bar{y}_f(\bar{x})$ (where $\bar{y}_f$ denotes both $y_{f,\ell}$ and $\bar{y}_{f,u}$) Observing the above noted boundary conditions at these limits, integration yields:

$$\rho_f \bar{v}_f = - \left[\int_0^{\bar{y}_f} \frac{\partial \rho \bar{u}}{\partial \bar{x}} \, d\bar{y} + \frac{1}{A} \frac{\partial A}{\partial \bar{x}} \int_0^{\bar{y}_f} \rho \bar{u} \, d\bar{y} \right] \tag{191}$$

Corresponding integration of Equations (176) and (177) and substitution of Equation (191) into the resulting equation yields:

$$\frac{d}{d\bar{x}} \int_0^{\bar{y}_f} \rho \bar{u}(\bar{u}_f - \bar{u}) \, d\bar{y} + \frac{d\bar{u}_f}{d\bar{x}} \int_0^{\bar{y}_f} (\rho_f \bar{u}_f - \rho \bar{u}) \, d\bar{y}$$

$$= - \frac{1}{A} \frac{\partial A}{\partial \bar{x}} \int_0^{\bar{y}_f} \rho \bar{u}(\bar{u}_f - \bar{u}) \, d\bar{y}$$

$$- \Omega^2 r \frac{dr}{dx} \cos\phi \int_0^{\bar{y}_f} \rho \, d\bar{y} \tag{192}$$

$$\frac{d}{d\bar{x}} \int_0^{\bar{y}_f} \rho\bar{u}(H_f' - H') \, d\bar{y} + \frac{dH_f'}{d\bar{x}} \int_0^{\bar{y}_f} (\rho_f\bar{u}_f - \rho\bar{u}) \, d\bar{y}$$

$$= - \frac{1}{A} \frac{\partial A}{\partial \bar{x}} \int_0^{\bar{y}_f} \rho\bar{u}(H_f - H) \cdot d\bar{y} \qquad (193)$$

Equations (191), (192) and (193) each represent a pair of equations; one for $y_f = y_{f,\ell}$, $u_{f,\ell}$, $v_f = v_{f,\ell}$, etc. and the other for $y_f = y_{f,u}$, $u_f = u_{f,u}$, etc.

The $\bar{y}$ coordinate is transformed according to:

$$\eta_1 = \int_0^{\bar{y}} \frac{\rho}{\rho_{f,\ell}} \, d\bar{y} \qquad \text{and } \eta_2 = \int_0^{\bar{y}} \frac{\rho}{\rho_{f,u}} \, d\bar{y} \qquad (194)$$

and transformed wake thicknesses are defined by:

$$\delta_\ell = \int_0^{\bar{y}_{f,\ell}} \frac{\rho}{\rho_{f,\ell}} \, d\bar{y} \qquad \text{and } \delta_u = \int_0^{\bar{y}_{f,u}} \frac{\rho}{\rho_{f,u}} \, d\bar{y} \qquad (195)$$

The eddy viscosity coefficient is assumed to transform according to[22]:

$$\varepsilon_i = \left(\frac{\rho}{\rho_{f,\ell}}\right)^2 \varepsilon_\ell = \left(\frac{\rho}{\rho_{f,u}}\right)^2 \varepsilon_u \qquad (196)$$

where ε_i denotes an equivalent incompressible value. The above transformations reduce the system consisting of Equations (189) through (193) to that of an equivalent incompressible flow. The eddy viscosity in incompressible flows has been experimentally correlated by*:

---

*For the sake of clarity, discussion of the basis of the selected eddy viscosity law and velocity profile representations is deferred to the end of this derivation.

$$\varepsilon_i = .032 \quad (\bar{u}_f - u_m)\ \delta \tag{197a}$$

In view of the noted asymmetry in the present application, Equation (197a) is interpreted as:

$$\varepsilon_i = .032 \quad ((\bar{u}_{f,\ell} + \bar{u}_{f,u})/2 \ - \ \bar{u}_m) \quad (\delta_\ell + \delta_u)/2 \tag{197b}$$

The velocity profile is represented by a corresponding approximation:

$$\bar{u}_f - \bar{u} = \begin{cases} (\bar{u}_{f,\ell} - \bar{u}_m)\ (1 + \cos\pi\eta_\ell/\delta_\ell)/2 & \text{for } 0 \leq \bar{y} \leq \bar{y}_{f,\ell} \\ \\ (\bar{u}_{f,u} - \bar{u}_m)\ (1 + \cos\pi\eta_u/\delta_u)/2 & \text{for } 0 \leq \bar{y} \leq \bar{y}_{f,u} \end{cases} \tag{198}$$

A similar representation is assumed for the relative total enthalpy profile, however, the possible existence of a different thickness for the relative total enthalpy defect than for the velocity defect is recognized:

$$H_f' - H' = \begin{cases} (H_{f,\ell}' - H_m')\ (1 + \cos\pi\eta_\ell/\delta_{T,\ell})/2 & \text{for } 0 \leq \bar{y} \leq \bar{y}_{T,\ell} \\ \\ (H_{f,u}' - H_m')\ (1 + \cos\pi\eta_u/\delta_{T,u})/2 & \text{for } 0 \leq \bar{y} \leq y_{T,u} \end{cases} \tag{199}$$

where $\delta_{T,\ell} \neq \delta_\ell$ and $\delta_{T,u} \neq \delta_u$ is assumed. In this connection, it should be pointed out that compressor or fan blades are usually uncooled and, therefore, operate at a wall temperature corresponding to the <u>average</u> absolute total temperature (or total enthalpy) of the airstream in which they are immersed. Thus, the difference $H_f' - H_m'$ will be on the order of the difference between the local, instantaneous total enthalpy and the average value experienced by the blade. It is anticipated that in general:

$$H_f' - H' \ll H_f' \tag{200}$$

Furthermore, it is well established that

$$\bar{u}_f - \bar{u} << \bar{u}_f \tag{201}$$

prevails within a turbulent wake a very short distance from the trailing edge. It, therefore, follows that:

$$\rho/\rho_f \simeq 1 \tag{202}$$

Also in connection with Equations (198) and (199), it should be noted that double-valued second derivatives of velocity and total enthalpy at $\bar{y} = 0$ result from the two forms of each equation. Therefore, the second derivatives at $\bar{y} = 0$ are approximated by:

$$\left(\frac{\partial^2 \bar{u}}{\partial \eta^2}\right)_m = \frac{2\pi^2}{(\delta_\ell + \delta_u)^2} \left((\bar{u}_{f,\ell} + \bar{u}_{f,u})/2 - \bar{u}_m\right) \tag{203}$$

$$\left(\frac{\partial^2 H'}{\partial \eta^2}\right)_m = \frac{2\pi^2}{(\delta_{T,\ell} + \delta_{T,u})^2} \left((H'_{f,\ell} + H'_{f,u})/2 - H'_m\right) \tag{204}$$

Substitution of the above-stated profile representations, eddy-viscosity law, and transformations (e.g., Equation (178)) into the system given by Equations (189), (190), (192) and (193), and using $\rho/\rho_f \simeq 1$ in evaluation of the integrals, yields the following set of ordinary differential equations:

$$\bar{u}_m \frac{d\bar{u}_m}{d\bar{x}} = -\frac{1}{\rho_m}\frac{dp}{d\bar{x}} + \frac{.032\pi^2}{(\delta_\ell + \delta_u)} \left[(\bar{u}_{f,\ell} + \bar{u}_{f,u})/2 - \bar{u}_m\right]^2 + \Omega^2 r \frac{dr}{dx} \cos\phi \tag{205}$$

$$\bar{u}_m \frac{dH'_m}{d\bar{x}} = \frac{.032\pi^2 (\delta_\ell + \delta_u)}{(\delta_{T,\ell} + \delta_{T,u})^2} \left[(\bar{u}_{f,\ell} + \bar{u}_{f,u})/2 - \bar{u}_m\right] \left[(H'_{f,\ell} + H'_{f,u})/2 - H'_m\right] \tag{206}$$

$$\frac{1}{\delta_i}\frac{d\delta_i}{d\bar{x}} = \frac{1}{(\bar{u}_{f,i} - \bar{u}_m)}\left(\frac{d\bar{u}_m}{d\bar{x}} - \frac{d\bar{u}_{f,i}}{d\bar{x}}\right) - \left(\frac{2}{\bar{u}_{f,i}}\frac{d\bar{u}_{f,i}}{d\bar{x}} + \frac{1}{\rho_{f,i}}\frac{d\rho_{f,i}}{d\bar{x}}\right)$$

$$- \frac{\cos\phi}{A}\frac{dA}{dx} - \frac{2\Omega^2 r\cos\phi}{\bar{u}_{f,i}(\bar{u}_{f,i} - \bar{u}_m)}\frac{dr}{dx}, \text{ for } i=\ell \text{ and } u \tag{207}$$

$$\frac{1}{\delta_{T,i}}\frac{d\delta_{T,i}}{d\bar{x}} = \frac{1}{(H'_{f,i} - H'_m)}\left(\frac{dH'_m}{d\bar{x}} - \frac{dH'_{f,i}}{d\bar{x}}\right) - \left(\frac{1}{\bar{u}_{f,i}}\frac{d\bar{u}_{f,i}}{d\bar{x}} + \frac{1}{\rho_{f,i}}\frac{d\rho_{f,i}}{d\bar{x}}\right)$$

$$- \frac{1}{\bar{u}_{f,i}}\left(\frac{dH'_{f,i}}{d\bar{x}}\right)\frac{\delta_i(\bar{u}_{f,i} - \bar{u}_m)}{\delta_{T,i}(H'_{f,i} - H'_m)} - \frac{\cos\phi}{A}\frac{dA}{dx}, \text{ for } i = \ell \text{ and } u \tag{208}$$

A more specific definition of the frontal locations $y_{f,\ell}$ and $y_{f,u}$ is now required to carry out the numerical integration of the above system. The frontal location can be unambiguously defined by matching the mass flow contained in the wake at any streamwise position to that in a corresponding inviscid streamline, namely:

$$\dot{m} = \int_0^{\bar{y}_f} (\rho\ \bar{u}\ d\bar{y})_{inviscid} = \int_0^{\bar{y}_f} (\rho\ \bar{u}\ d\bar{y})_{wake} \approx \rho_f\ \bar{u}_f\ \bar{y}_f \tag{209}$$

Thus;

$$\bar{y}_f = \frac{1}{\rho_f\ \bar{u}_f}\int_0^{\bar{y}_f} (\rho\ \bar{u}\ d\bar{y})_{inviscid} \tag{210}$$

where:

$$\bar{u}_f = \bar{u}_{inviscid}(\bar{x}, \bar{y} = \bar{y}_f, t) \tag{211a}$$

$$\rho_f = \rho_{inviscid}(\bar{x}, \bar{y} = \bar{y}_f, t) \tag{211b}$$

etc.

and:

$$\frac{d\bar{u}_f}{d\bar{x}} = \left[\frac{\partial \bar{u}_{inviscid}}{\partial \bar{x}}\right]_{\bar{x},\bar{y}=\bar{y}_f,t} + \left[\frac{\partial \bar{u}_{inviscid}}{\partial \bar{y}}\right]_{\bar{x},\bar{y}=\bar{y}_f,t} \frac{d\bar{y}_f}{d\bar{x}} \tag{212}$$

The $\bar{x}$ derivatives of H_f' and ρ_f must be correspondingly defined. Since $\rho/\rho_f \simeq 1$;

$$\frac{d\bar{y}_{f,i}}{d\bar{x}} = \frac{d\delta_i}{d\bar{x}} \qquad \text{for } i = \ell \text{ and } u \tag{213}$$

Therefore, Equation (207) must be rewritten as:

$$\frac{d\delta_i}{d\bar{x}} = \frac{\frac{1}{(\bar{u}_{f,i} - \bar{u}_m)}\left[\frac{d\bar{u}_m}{d\bar{x}} - \left(\frac{\partial \bar{u}}{\partial \bar{x}}\right)\right] - \left(\frac{2}{\bar{u}_{f,i}}\frac{\partial \bar{u}}{\partial \bar{x}} + \frac{1}{\rho_{f,i}}\frac{\partial \rho}{\partial \bar{x}}\right) - \frac{\cos\phi}{A}\frac{dA}{dx} - \frac{2\Omega^2 r\cos\phi}{\bar{u}_{f,i}(\bar{u}_{f,i} - \bar{u}_m)}\frac{dr}{dx}}{\frac{1}{\delta_i} + \frac{3\bar{u}_{f,i} - 2\bar{u}_m}{\bar{u}_{f,i}(\bar{u}_{f,i} - \bar{u}_m)}\left(\frac{\partial u}{\partial \bar{y}}\right) + \frac{1}{\rho_f}\frac{\partial \rho}{\partial \bar{y}}} \tag{214}$$

for $i = \ell$ and u

where $\partial/\partial\bar{x}$ and $\partial/\partial\bar{y}$ denote the inviscid flow values at $(\bar{x}, \bar{y} = \bar{y}_f, t)$ as used in Equation (212).

To within the approximation contained in the above system of equations, the displacement, momentum defect and thermal energy defect thicknesses in the wake are defined by:

$$\delta_i^* = \delta_i \frac{\bar{u}_{f,i} - \bar{u}_m}{2\bar{u}_{f,i}} \qquad \text{for } i = \ell \text{ and } u \tag{215}$$

$$\theta_i = \delta_i \frac{\bar{u}_{f,i} - \bar{u}_m}{2\bar{u}_{f,i}} \qquad \text{for } i = \ell \text{ and } u \tag{216}$$

$$\theta_{T,i} = \delta_{T,i} \frac{H_{f,i}' - H_m'}{2H_{f,i}'} \qquad \text{for } i = \ell \text{ and } u \tag{217}$$

Thus, $\delta_i^* = \theta_i$ in this context. However, in the boundary layer at the trailing edge $\delta^* \neq \theta$; therefore, the wake solution cannot match both the displacement and momentum thicknesses of the boundary layer solution, and a mismatch in one or the other must be accepted. Since the displacement thickness is to be used as an effective boundary of the inviscid flow, a mismatch in δ^* is considered unacceptable. Therefore, the initial conditions for the wake solution are taken to be:

$$\bar{u}_m(0) = 0.0 \tag{218}$$

$$H_m'(0) = (C_p T)_{\substack{\text{blade} \\ \text{trailing edge}}} - \frac{1}{2}\Omega^2 r^2 \tag{219}$$

$$\delta_\ell(0) = 2\,\delta^*_{\substack{\text{blade upper surface} \\ \text{trailing edge}}} \tag{220a}$$

$$\delta_u(0) = 2\,\delta^*_{\substack{\text{blade lower surface} \\ \text{trailing edge}}} \tag{220b}$$

$$\delta_{T,\ell}(0) = \delta_\ell(0) \tag{221a}$$

$$\delta_{T,u}(0) = \delta_u(0) \tag{221b}$$

(The initial thermal defect thickness is equated to the initial velocity defect thickness in lieu of any more precise information. Should a more detailed boundary layer solution be incorporated in the model at a later date, the initial wake conditions can be modified accordingly.)

Analysis of Merged Wakes

In the foregoing discussion, it has been implied that the wake of each blade grows into a known inviscid flow field. However, at a sufficient distance downstream of the blade row the wakes will entrain the entire inviscid field and merge to form a completely turbulent field. In this case the previously stated analysis must be modified accordingly. Following the previously

outlined procedures, using the same small perturbation approximations, and adopting the same profile representations*, the integrated form of the continuity equation becomes:

$$\frac{d}{d\bar{x}} (\bar{u}_m + \bar{u}_f) = - (\bar{u}_m + \bar{u}_f) \frac{\cos \phi}{A} \frac{dA}{dx} \tag{222}$$

where now $\bar{u}_f = \bar{u}_{f,\ell} = \bar{u}_{f,u}$ and $\bar{\delta} = (\delta_\ell + \delta_u)/2$. Evaluating the momentum equation on the axis ($\bar{y} = 0$) and at $\bar{y} = \bar{y}_{f,\ell} = 2\pi r/N - \bar{y}_{f,u}$ gives:

$$\bar{u}_m \frac{d\bar{u}_m}{d\bar{x}} = - \frac{1}{\rho_m} \frac{dp}{d\bar{x}} + .032 (\bar{u}_f - \bar{u}_m)^2 \frac{\pi^2}{2\bar{\delta}} + \Omega^2 r \frac{dr}{dx} \cos\phi \tag{223}$$

and

$$\bar{u}_f \frac{d\bar{u}_f}{d\bar{x}} = - \frac{1}{\rho_f} \frac{dp}{d\bar{x}} - .032 (\bar{u}_f - \bar{u}_m)^2 \frac{\pi^2}{2\bar{\delta}} + \Omega^2 r \frac{dr}{dx} \cos\phi \tag{224}$$

Substituting from Equation (224) into (222) gives:

$$\bar{u}_f \frac{d\bar{u}_m}{d\bar{x}} = \frac{1}{\rho_f} \frac{dp}{d\bar{x}} + .032 (\bar{u}_f - \bar{u}_m)^2 \frac{\pi^2}{2\bar{\delta}} - \bar{u}_f (\bar{u}_m + \bar{u}_f) \frac{\cos \phi}{A} \frac{dA}{dx} - \Omega^2 r \frac{dr}{dx} \cos\phi \tag{225}$$

Adding Equations (223) and (225), and noting that $\rho_f - \rho_m << \rho_f$, yields:

$$(\bar{u}_f - \bar{u}_m) \frac{d\bar{u}_m}{d\bar{x}} \simeq .064 (\bar{u}_f - \bar{u}_m)^2 \frac{\pi^2}{2\bar{\delta}} - \bar{u}_f (\bar{u}_m + \bar{u}_f) \frac{\cos \phi}{A} \frac{dA}{dx} \tag{226}$$

Thus, the rate of changes of $\bar{u}_f$ and of $\bar{u}_m$ are determined from Equations (222) and (226). Furthermore, the pressure is determined from the sum of Equations (223) and (224):

$$\left(\frac{1}{\rho_f} + \frac{1}{\rho_m}\right) \frac{dp}{d\bar{x}} = - \left(\bar{u}_m \frac{d\bar{u}_m}{d\bar{x}} + \bar{u}_f \frac{d\bar{u}_f}{d\bar{x}}\right) + 2\Omega^2 r \frac{dr}{dx} \cos\phi \tag{227}$$

---

*Note that the cosine function is particularly appropriate for this problem due to the periodic character of the wake. See Reference (15), Chapter 23, p. 604.

Evaluation of the energy equation on $\bar{y} = 0$ and on $\bar{y} = \bar{y}_{f,\ell} = 2\pi r/N - \bar{y}_{f,u}$ gives:

$$\bar{u}_m \frac{dH_m'}{d\bar{x}} = .032\ (\bar{u}_f - \bar{u}_m)\ (H_f' - H_m')\ \frac{\pi^2}{2\bar{\delta}} \tag{228}$$

and

$$\bar{u}_f \frac{dH_f'}{d\bar{x}} = -\ .032\ (\bar{u}_f - \bar{u}_m)\ (H_f' - H_m')\ \frac{\pi^2}{2\bar{\delta}} \tag{229}$$

from which the rates of change of H_m' and H_f' can be obtained. Note that $\delta_T = \delta$ is required downstream of the point of merger.

It is remarked parenthetically that in the special case of $dA/d\bar{x} = 0$, Equations (222) and (226) can be combined to yield the well known result that the maximum velocity differential $(\bar{u}_f - \bar{u}_m)$ must asymptotically decay linearly with increasing distance, in contrast to asymptotic square root decay rate for the individual blade wakes.[15]

Eddy Viscosity Law and Velocity Profile Representations

A variety of formulas have been proposed in various investigations to relate the eddy viscosity defined by the Reynolds stress, namely:

$$\varepsilon = -\frac{\overline{u'v'}}{(\partial\bar{u}/\partial\bar{y})} = \left(\frac{\varepsilon}{\nu}\right)_{turbulent} \tag{230}$$

to the mean properties of a turbulent flow. The present formulation will draw upon one of the earliest and most generally accepted eddy viscosity laws; however, its validity can only be established by comparison with experiment and it should always be regarded as tentative and subject to revision.

A "universal" number characterizing the eddy viscosity in a turbulent, incompressible wake was derived by Townsend[23] based on equilibrium of energy among the large-scale eddies:

$$R_T = (\bar{u}_f - \bar{u}_m)\, \ell_o/\varepsilon = \text{constant} \tag{231}$$

where ℓ_o is a wake width parameter defined by the requirement that the velocity profile conform with:

$$\bar{u}_f - \bar{u} = (\bar{u}_f - \bar{u}_m) \exp(-\bar{y}^2/2\ell_o^2) \tag{232}$$

Townsend[23] obtained the value $R_T = 12.5$ from a correlation of his data on the wake of a cylindrical rod in the form:

$$\bar{u}_f - \bar{u} = (\bar{u}_f - \bar{u}_m) \exp\left(-\sqrt{\frac{\pi}{2}}\, \frac{R_T}{C_d}\, \frac{\bar{y}^2}{(\bar{x} - \bar{x}_o)d}\right) \tag{233}$$

from which ℓ_o can be identified as:

$$\ell_o = (C_d\, (\bar{x} - \bar{x}_o)d/\sqrt{2\pi}\, R_T)^{\frac{1}{2}} \tag{234}$$

where C_d is the drag coefficient, d the rod diameter and x_o an effective origin. A somewhat more useful definition of ℓ_o can be obtained as follows. We note that Townsend's wake data can also be accurately correlated in terms of Coles wake function[24] as indicated in Figure (12):

$$\frac{\bar{u} - \bar{u}_m}{\bar{u}_f - \bar{u}_m} = \frac{1}{2}\, W(\eta) \tag{235}$$

where $\eta = y/\delta$ and δ is the value of y where $u \simeq u_f$. $W(\eta)$ is a tabulated function based on correlation of turbulent boundary layer data, and is known to have wide applicability to compressible as well as incompressible flow through suitable transformation[25]. $W(\eta)$ can be accurately approximated (see Figure 12) by $W = 1 - \cos\pi\eta$. Therefore,

$$\bar{u}_f - \bar{u} = (\bar{u}_f - \bar{u}_m)\, \frac{1}{2}\, (1 + \cos\pi\eta) \tag{236}$$

The above velocity distribution is matched to the desired exponential form, Equation (232), by requiring that:

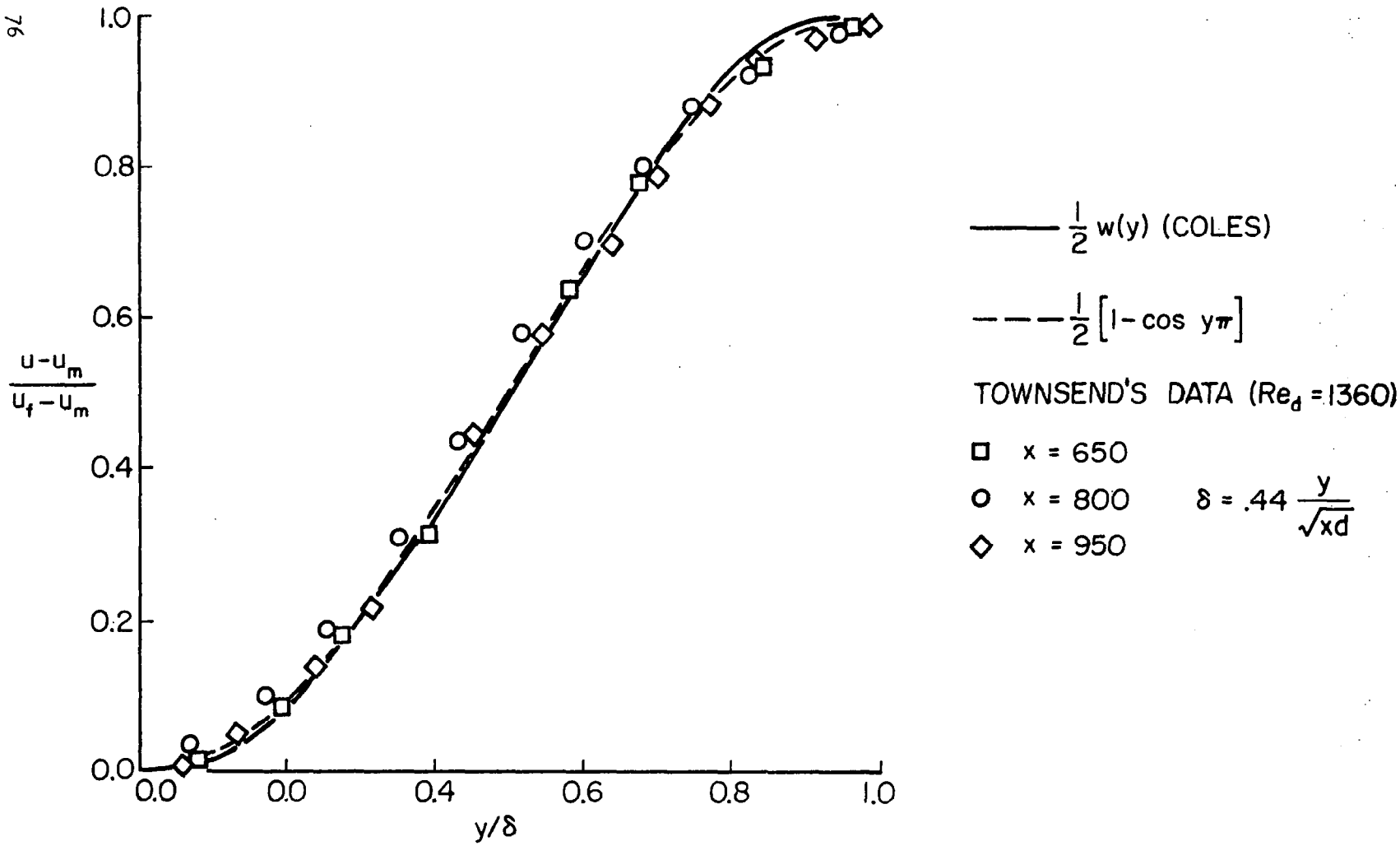

FIGURE 12. NON-DIMENSIONAL TURBULENT WAKE VELOCITY PROFILE

$$\int_0^\infty \exp\left(-\bar{y}^2/2\ell_o^2\right) \, d\bar{y} = \frac{1}{2} \int_0^\infty \left(1 + \cos\pi\bar{y}/\delta\right) \, d\bar{y} \tag{237}$$

which gives

$$\ell_o = \delta/\sqrt{2\pi} \simeq 0.40\ \delta \tag{238}$$

Therefore, if the velocity profile is represented by Equation (236), the eddy viscosity is consistently represented by:

$$\varepsilon = 0.032\ (\bar{u}_f - \bar{u}_m)\ \delta \tag{239}$$

Parenthetically, it is noted that in terms of the exponential form, the above value of ℓ_o gives $\bar{u} = .957\ \bar{u}_f + .043\ \bar{u}_m$ at $y = \delta$.

It is emphasized that the above results pertain to incompressible flows. The extension to compressible flows by transformation has been discussed by Ting and Libby[22]. In particular, the postulate that the shear stress remains invariant under density transformation (see Reference 22) has led to satisfactory results at supersonic and hypersonic conditions and, thus, should be quite accurate for the presently considered transonic and low supersonic flows.

Composite Solution

As previously indicated, the viscous and inviscid solutions obtained at the exit of domain 4 are used to define a composite inviscid solution for the entrance station of domain 5. The composite solution is defined as follows:

$$u = \left\{ \begin{array}{ll} (\bar{u}\cos\phi)_{viscous} & \alpha \leq 0 \\ (1-\alpha)\ (\bar{u}\cos\phi)_{viscous} + \alpha u_{inviscid} & 0 < \alpha < 1 \\ u_{inviscid} & \alpha \geq 1 \end{array} \right\} \tag{240}$$

$$v = \begin{cases} (\bar{u}\sin\phi)_{viscous} + v_{inviscid} & \alpha \leq 0 \\ (1-\alpha)\ (\bar{u}\sin\phi)_{viscous} + v_{inviscid} & 0 < \alpha < 1 \\ v_{inviscid} & \alpha \geq 1 \end{cases} \tag{241}$$

$$H' = \begin{cases} H'_{viscous} & \alpha \leq 0 \\ (1-\alpha)\ H'_{viscous} + \alpha\ H'_{inviscid} & 0 < \alpha < 1 \\ H'_{inviscid} & \alpha \geq 1 \end{cases} \tag{242}$$

$$p = p_{inviscid} \tag{243}$$

where:

$$\alpha = (\bar{y}-\delta^*)/(\delta-\delta^*) \tag{244}$$

$$\bar{y} = |y-y_i|\ \cos\phi \qquad i = \ell \text{ and } u \tag{245}$$

The variables denoted by $\bar{u}_{viscous}$ and $H'_{viscous}$ are obtained from the profile representation given by Equations (198) and (199) using the viscous solution $\bar{u}_m$, H'_m, δ_i and $\delta_{T,i}$ and the frontal values $\bar{u}_{f,i}$ and $H'_{f,i}$ ($i = \ell$ and u). The range of values of $\bar{y}$ is selected to match the undisplaced y coordinates* of the grid points on those two grid columns of domain 4 which bound the first grid column of domain 5, and composite solutions are generated at these two stations, Equations (240) - (243). The inviscid solution for the first grid column of domain 5 is then obtained by linear interpolation of the composite solutions, for use in accord with the procedures outlined in the sub-section entitled "Periodicity Condition". Thus, the composite solutions simply replace the inviscid solution which would be used to carry out the interfacing of domains 4 and 5 in the absence of viscous effects.

---

*The transformed circumferential coordinate ν used for the inviscid solution in domain 4 (and also domains 3, 5, 6 and 7) obviously includes the local displacement thickness in definition of the computational boundaries; i.e., in Equation (37) $y_i = r\theta_i \pm \delta_i^*$ ($i = \ell$, u). Thus, the displaced computational domain does not span the entire blade-to-blade passage, whereas the undisplaced domain does.

RESULTS

The method of analysis described above has been implemented in a FORTRAN code[26] and tested with respect to several single stage transonic fans for which experimental data is available[27,28]. A combination of design information and measured data for these fans has been used to define the initial and boundary conditions. The "infinite duct" inlet and discharge boundary conditions were used in the calculations reported here; limited tests with the "open end" conditions were also conducted, but detailed comparisons with the "infinite duct" model were not carried out. The meridional plane analysis of Katsanis and McNally[29] was used to define the streamsheet thickness and radius by tracing a selected streamtube through the stage.

As a prelude to analysis of rotor-stator interactions, several isolated rotor analyses and an isolated stator analysis were carried out. The stator analysis will be discussed first, since comparison of the present method and the relaxation method of Katsanis[30] is possible for this case, which offers a direct assessment of the program accuracy, independent of the viscous and three-dimensional effects present in the transonic rotor data. Since the stator is subcritical at the selected operating condition, the velocity-gradient technique[30] provides a reasonably accurate benchwork solution for a shock-free flow. The experimental data[27,28] for the rotors will be used primarily to indicate the predictive capability of the present method with respect to the structure of passage shock systems.

The stator is part of a 1500 fps (457 m/s) tip speed transonic fan stage[27], which will be described more completely later in connection with the rotor-stator interaction analysis. The stator row has 46 blades and a hub to tip ratio of 0.6. The selected operating point corresponds to Reading 137, of Reference (27) which is an open throttle, 100% speed condition. The selected streamsheet follows the casing wall and has a thickness of 1/3 of 1% of the casing radius at the inlet station (one chord length upstream of the rotor). The inlet Mach number is 0.6 and the inlet flow angle is -30.7°. The stator is intended to produce a purely axial exit flow. The blade section at the casing is shown at the top of Figure (11). A grid network consisting of 17 columns (axially) and 9 rows (circumferentially) in each of three domains (i.e., 459 points, excluding external

grid points) was used for this case, as well as the isolated rotor cases to be discussed next. The solutions converged within 10^3 time steps with this grid point density, and each required approximately three minutes execution time on a CDC 7600 computer.

An inlet Mach number of 0.65 and an inlet flow angle of -30.0°, with negligible circumferential variations, were obtained from the present stator solution. The outlet flow angle varied circumferentially from 6.6 to 7.0°. The relaxation solution was carried out for the same inlet Mach number of 0.65, but using the design inlet and exit flow angles of -30.7° and 0.0°, respectively. (Specification of the exit flow angle replaces the trailing edge Kutta condition in the relaxation method[30].) Sixty-one grid columns and 20 grid rows were used in the relaxation solution. The surface Mach number distributions are shown on the bottom of Figure (13). It can be seen that the effect of nose bluntness (which is included in the relaxation solution[30]) is essentially confined to the first 5-10% of the chord. The compression surface solutions are in quite good agreement up to the last 20% of the chord, where the effect of the manner of enforcing the Kutta condition is evident. The suction surface solutions exhibit a fairly uniform difference; the present method results in a somewhat higher Mach number over almost all the surface. In view of the doubled grid point density in the circumferential direction used in the relaxation solution, it must be regarded as numerically more accurate; however, the accuracy of the velocity-gradient approximation for a local Mach number approaching unity is uncertain.

The rotor for this stage[27] has 44 blades and a hub-to-tip ratio of 0.5. The tip speed is 1500 fps, (457 m/s), producing an inlet relative Mach number of 1.526 at the design point. The tip diameter is 36.5 inches (0.927 m) and has an axial chord length of 1.7 inches (0.0432 m) at the tip. The rotor has a shroud (vibration damper) located about 40% of span in from the tip. The stage also included 24 variable camber inlet guide vanes, located slightly more than one rotor chord length upstream of the rotor. Under the presently considered conditions the guide vanes were set to zero camber, to produce a purely axial inlet flow to the rotor. The same operating point (Reading 137) was examined, at which the stage total pressure ratio was 1.48 and the inlet relative Mach number at the tip was 1.49. The streamsheet was again assumed to be a very narrow layer along the casing wall (having a thickness about 1/3 of 1% of the radius).

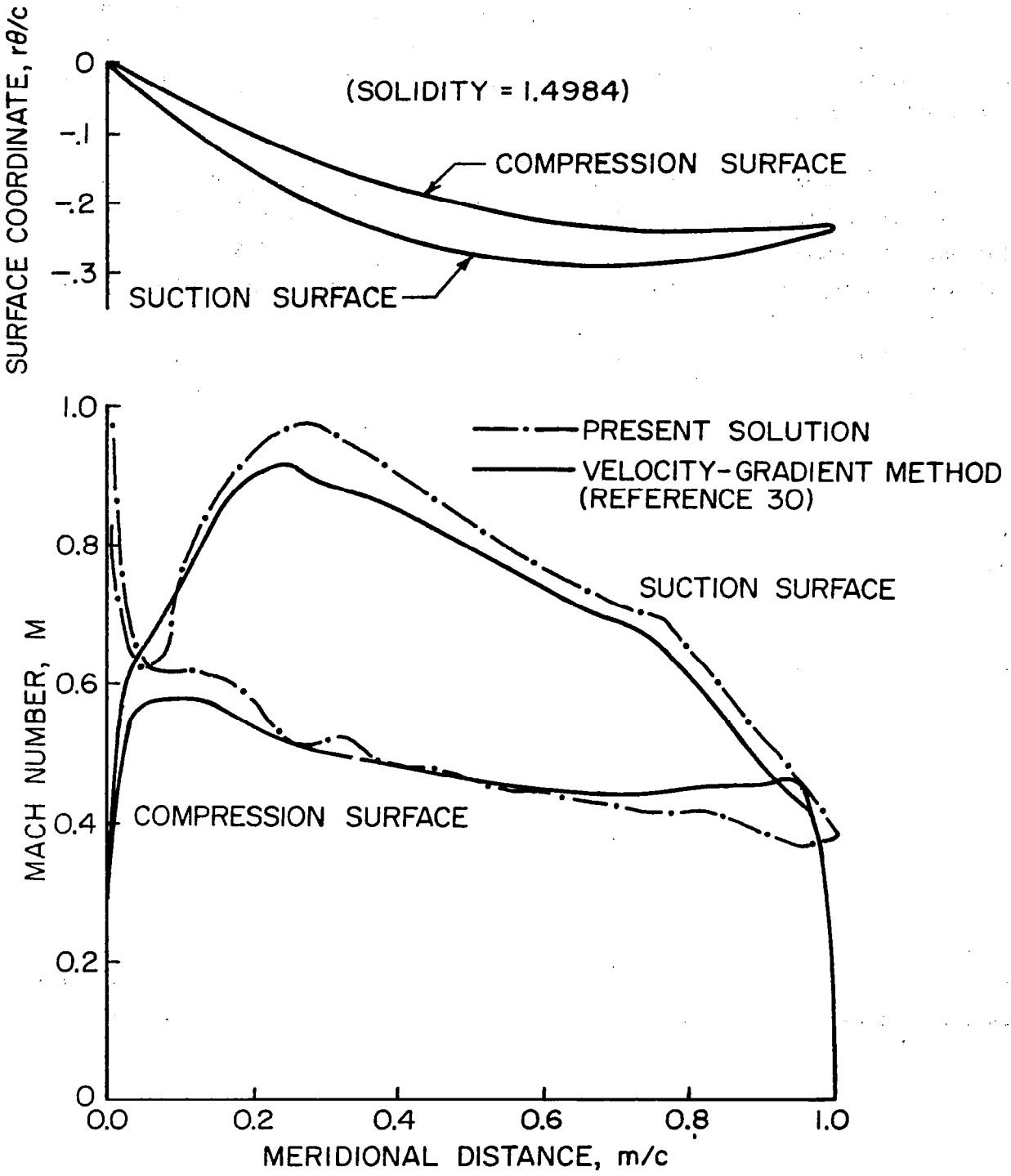

FIGURE 13. STATOR BLADE TIP SECTION GEOMETRY AND COMPARISON OF SURFACE MACH NUMBER DISTRIBUTIONS

An inlet Mach number of 1.47 was obtained in this case, and the rotor total pressure ratio varied (circumferentially) from 1.37 to 1.50, in good agreement with the design conditions. The rotor pressure contours obtained from the present solution are displayed in Figure (14a) and compare favorably with those obtained from arrays of fast-response pressure gages in the casing wall[27], shown in Figure (14b). A more direct comparison is offered in Figure (15) which presents the blade surface pressure distributions. The differences near the leading edge are probably attributable to the effects of nose bluntness. The observed regions of compression-expansion preceding the passage shock ($z/c \approx 0.7$ on the compression surface and $z/c \approx 1.0$ on the suction surface) are indicative of local boundary layer separation bubbles. The part-span shroud may also be generating a shock wave which interacts with the blade shock system. In view of these factors, the general agreement between theory and experiment is regarded as quite satisfactory.

The three-dimensional shock structure near the tip of a similar transonic rotor was visualized using pulsed laser holography in Reference (28). In this example, the rotor has a tip speed of 1600 fps, (488 m/s), and a design pressure ratio (for the stage) of about 1.5. The tip diameter of the fan is 28.74 inches (0.730 m) and the (axial) chord length is 1.804 inches (.0458 m). The inlet hub-to-tip radius ratio is 0.46 and the nominal inlet relative Mach number is 1.6 at the tip. The rotor has 40 blades, and includes a midspan vibration damper located about 30% of the span in from the tip.

The streamsheet thickness and radius distributions were obtained by tracing a streamtube located about 5% of the span in from the tip and having 0.11 inches (.00279 m) thickness at the inlet station one chord upstream of the blade row. Since its thickness is less than 1% of its radius, the streamsheet radius closely follows the casing of the machine. Three operating conditions were examined; (a) the design point (Reading 128), (b) 100% design speed with a pressure ratio of 1.7 (Reading 126) and (c) 90% speed with a pressure ratio of 1.5 (Reading 106).

The computed pressure contour map for the design case is shown in Figure (16). The presence of a weak shock off the blade leading edge is evident; it subsequently reflects off the lower blade at about the 85% chord position and then apparently merges into a stronger shock which crosses the passage from the trailing edge of

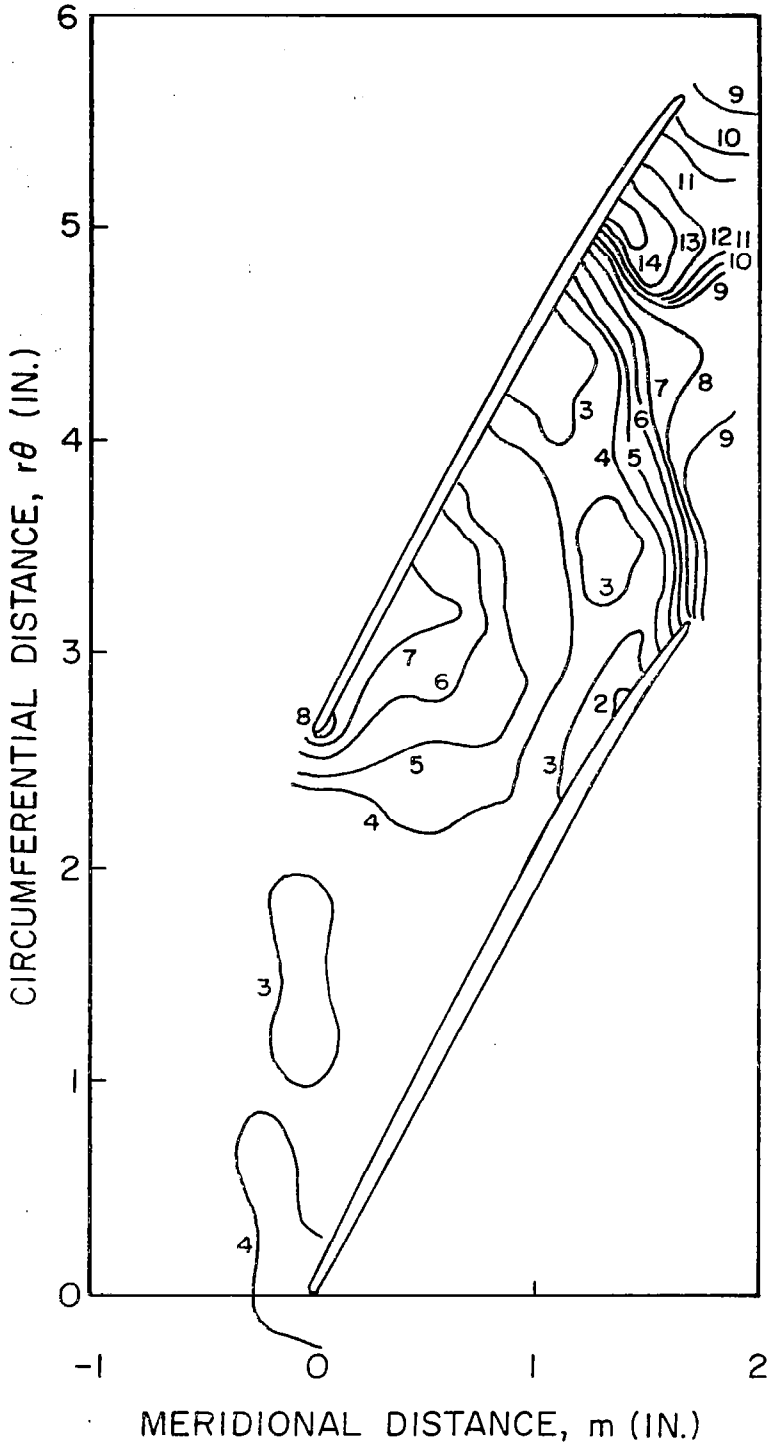

FIGURE 14a. CALCULATED STATIC PRESSURE CONTOURS AT ROTOR TIP

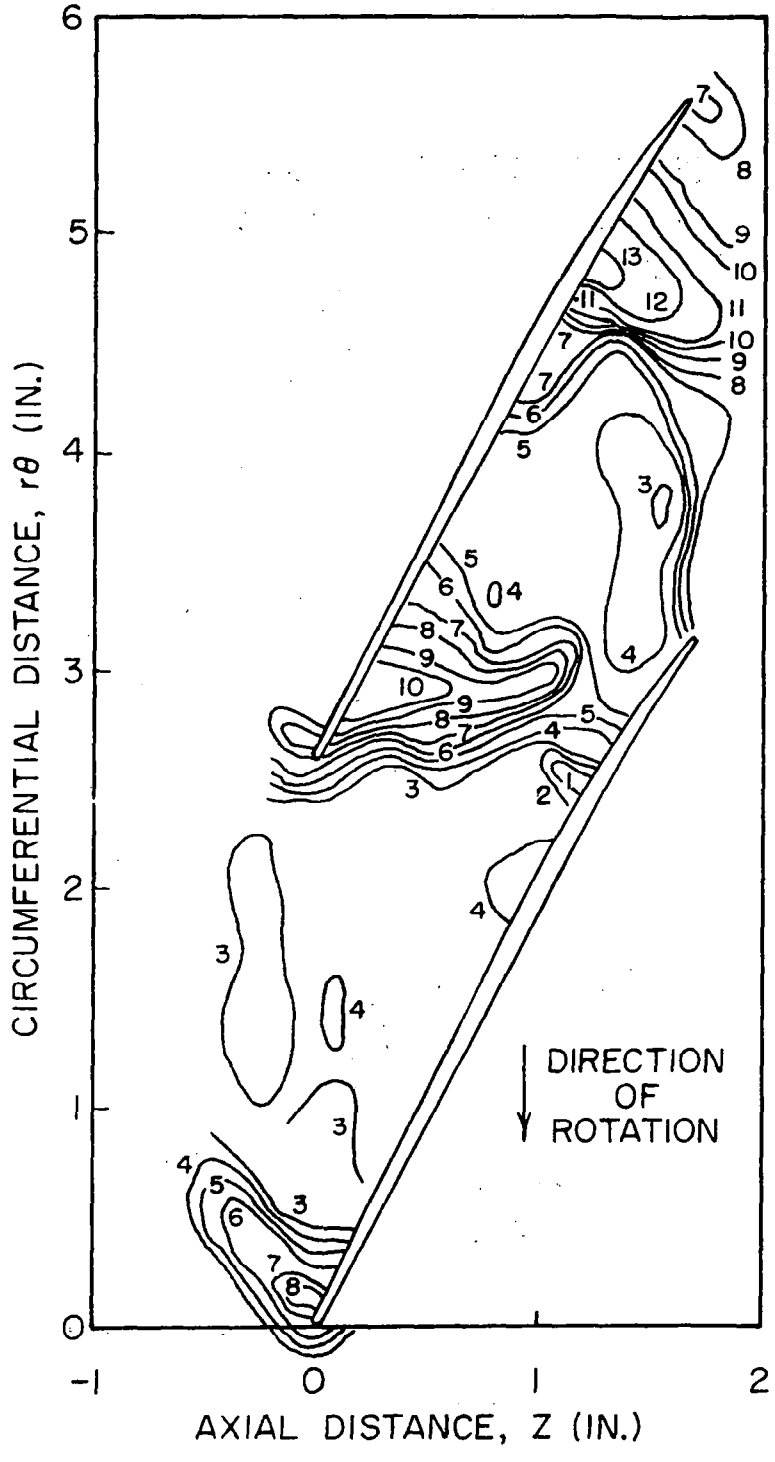

CONTOUR NUMBER	PRESSURE (PSIA)	(P/P_∞)
1	9	.7647
2	10	.8496
3	11	.9346
4	12	1.0195
5	13	1.1045
6	14	1.1895
7	15	1.2744
8	16	1.3594
9	17	1.4444
10	18	1.5293
11	19	1.6143
12	20	1.6992
13	21	1.7842

FIGURE 14b. MEASURED STATIC PRESSURE CONTOURS AT ROTOR TIP (READING 137 FROM REFERENCE 27)

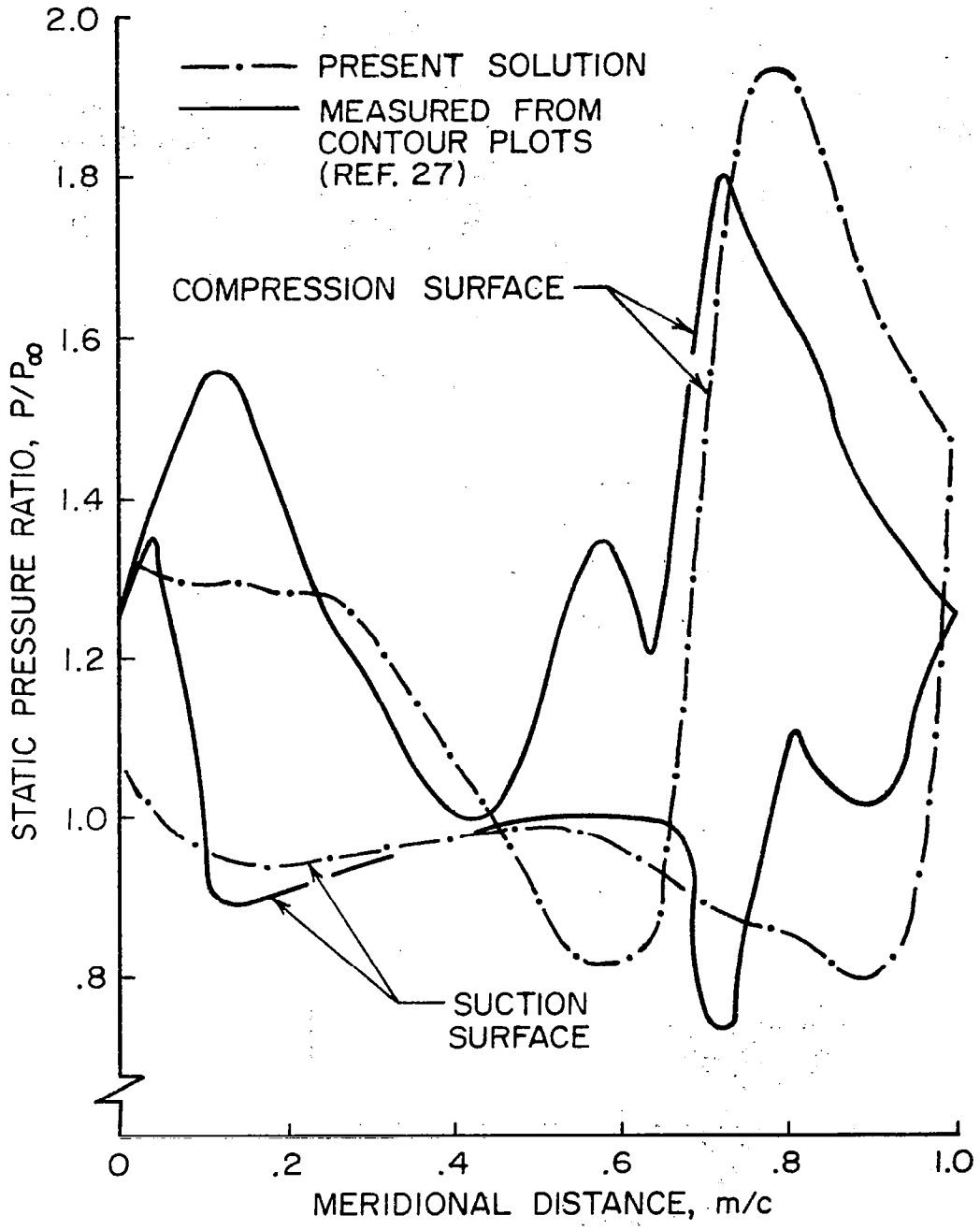

FIGURE 15. PRESSURE DISTRIBUTIONS ON ROTOR BLADE TIP SURFACES (READING 137).

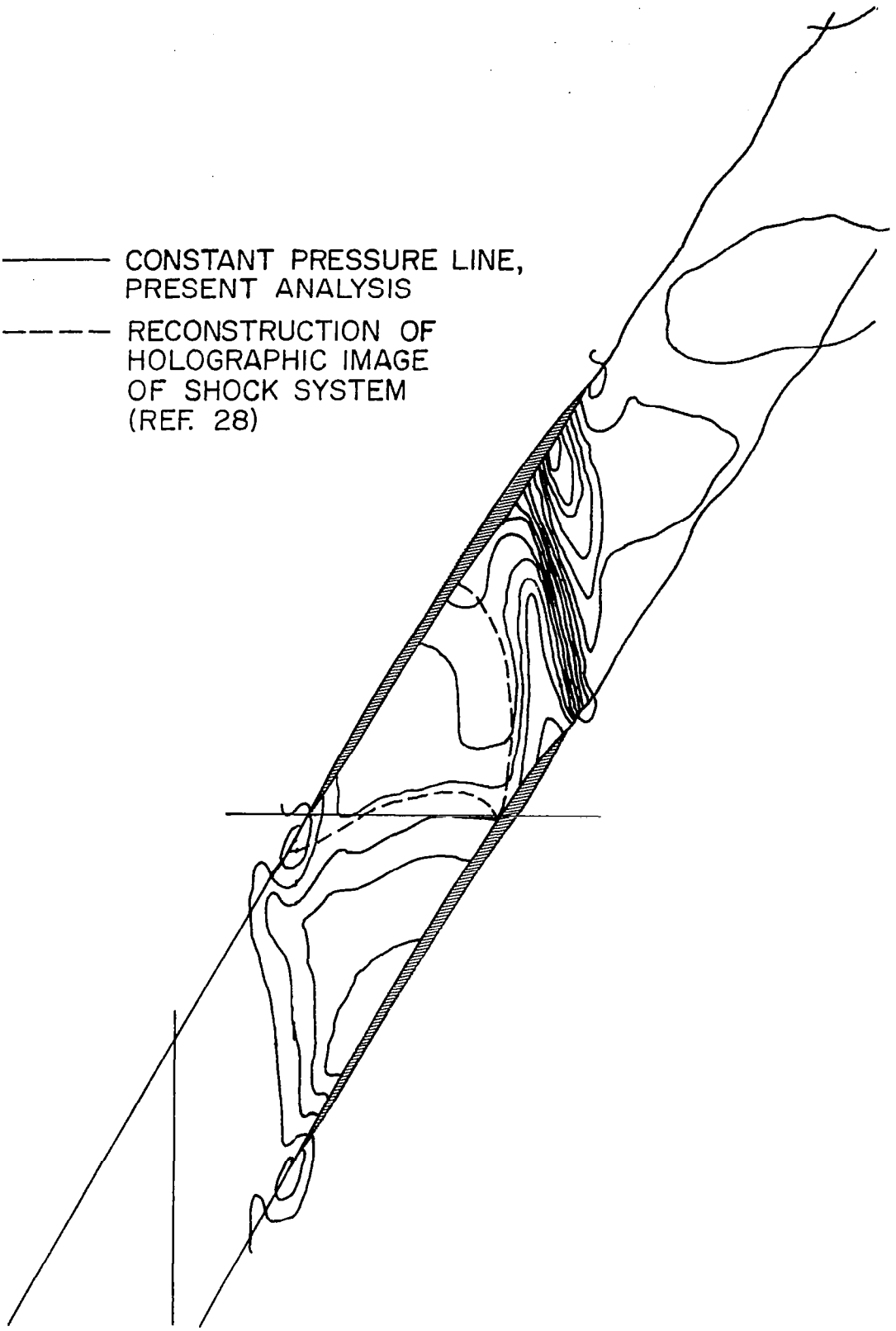

FIGURE 16. COMPUTED ISOBARS FOR READING 128 OF REFERENCE (28) $M_\infty = 1.6$ AND PRESSURE RATIO = 1.5

the lower blade to about the 85% chord position on the upper blade. These features are generally in accord with the reconstructed holographic observations[28]; however, the interaction between the tip leakage vortex, which stands on the suction (i.e., low pressure) surface of the lower blade, apparently causes the rearward portion of the leading edge shock to bend forward somewhat such that it reflects off the lower blade at about 75% chord (rather than 85%), and the trailing edge shock is correspondingly displaced upstream. The shock off the vibration damper also appears to be interacting with the blade shocks[28]. In addition, the assumption of a sharp leading edge may have reduced the strength of the leading edge shock. The computed total pressure ratio at the discharge station varied (circumferentially) from 1.45 to 1.51, in reasonable agreement with the overall stage pressure ratio of 1.505 reported at this operating condition[28]. The relative Mach number at the inlet converged to 1.51 as compared to the initial value of 1.53.

In the second case (Reading 126), the higher back pressure produced a modest forward shift of the trailing edge shock near the upper blade, as can be seen in Figure (17). The solution along the suction surface of the lower blade, as well as the forward 50-60% of the compression surface of the upper blade, is virtually unchanged, since forward propagation of the higher back pressure is terminated at the trailing edge shock. No experimental data is available at this operating condition.

As can be seen from Figure (18), the reduced wheel speed of the third case (Reading 106) results in a lower relative inlet Mach number, i.e., about 1.4, and a further shift of the trailing edge shock, to form a normal shock across the passage. However, the holographic reconstruction[28] indicates that the rotor is "unstarted" at this condition, i.e., the normal shock stands across the passage at the leading edge of the upper blade. The solution for this case was perturbed several times, e.g., by increasing the back pressure, by altering the streamsheet thickness distribution, and by reinitializing the data to an "unstarted" condition, in an unsuccessful attempt to produce an "unstarted" solution. Therefore, this disparity between theory and experiment must be attributed to one or more significant features of the acutal flow field identified above but not incorporated in the present analysis: finite nose bluntness, viscous effects, and three-dimensionality. Nose bluntness effects are believed to be significant in several

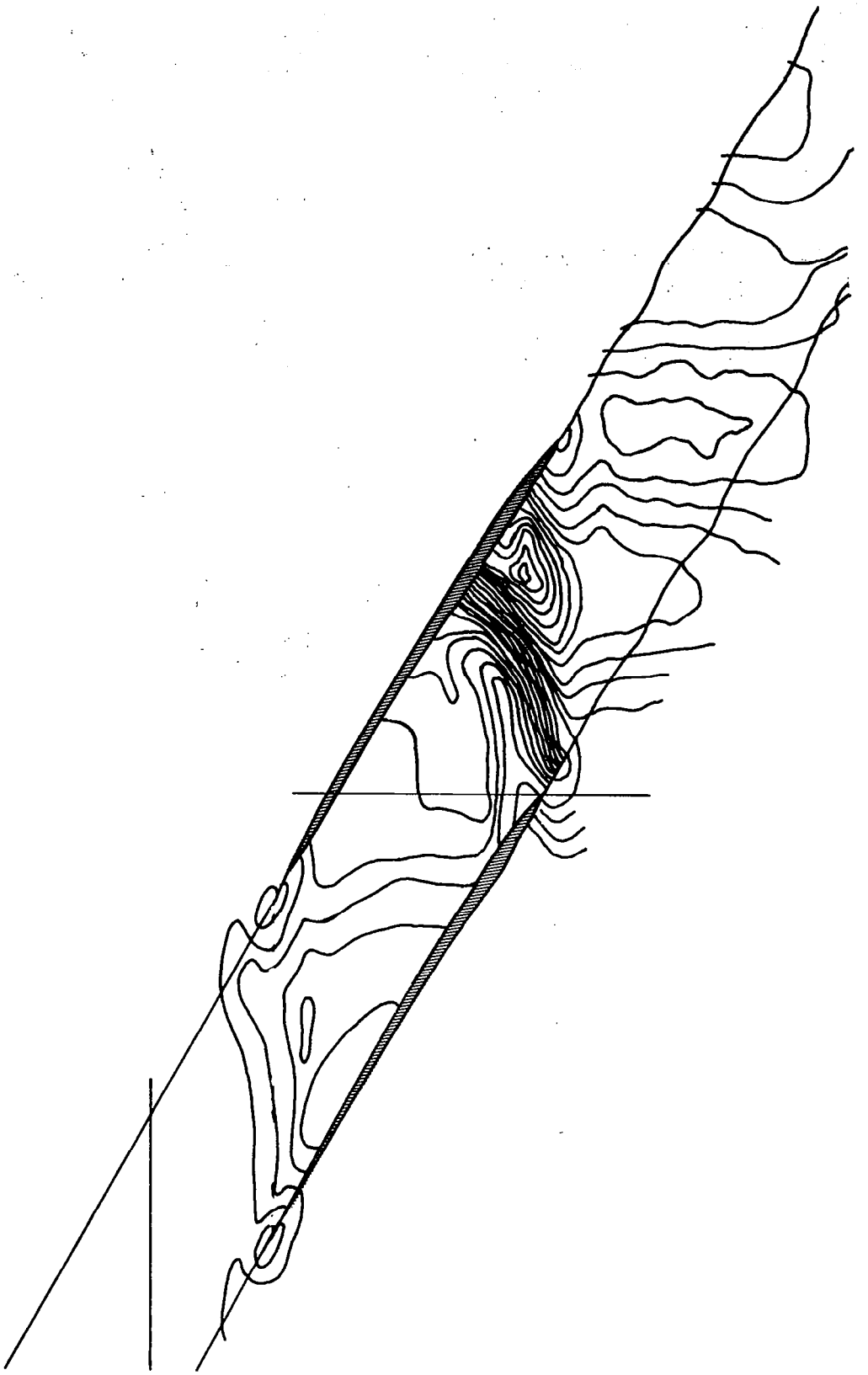

FIGURE 17. COMPUTED ISOBARS FOR READING 126 OF REFERENCE (28)
$M_\infty = 1.6$ AND PRESSURE RATIO = 1.7

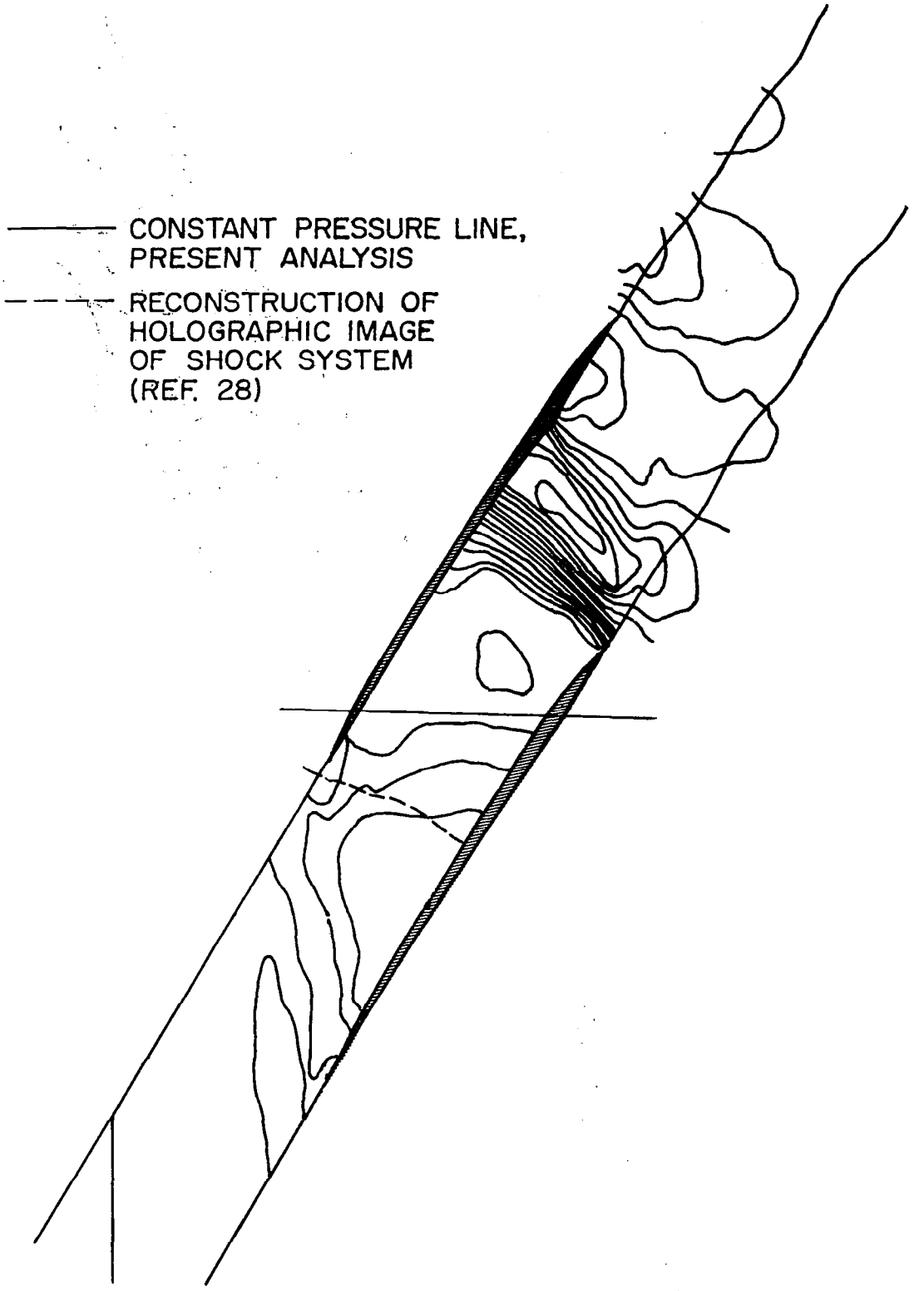

FIGURE 18. COMPUTED ISOBARS FOR READING 106 OF REFERENCE (28) $M_\infty = 1.4$ AND PRESSURE RATIO = 1.5

respects, and should be included to enhance the accuracy and expand the range of applicability of the present analysis, but in the present case do not appear to be sufficient to cause the passage to "unstart". The same comments can be made with respect to viscous effects on the blade surfaces. However, the tip leakage vortex and the vibration damper shock present major three-dimensional perturbations to the flow near the tip section, which are not easily accommodated in a two-dimensional model, but could cause the noted discrepancy between the present results and the observed unstarted shock system structure.

Finally, the rotor-stator interaction has been examined at the open throttle, 100% speed operating point (Reading 137 of Reference 27) previously selected. As pointed out earlier, the stage includes 44 rotor blades and 46 stator blades. Since the flow leaving the rotor is supersonic ($M \simeq 1.1$) upstream propagation of disturbances from the stator should be cut-off beyond the steady wave front intersecting the trailing edge of the lower rotor blade of the passage. If the flow were uniform in the passage, this wave front would intersect the upper rotor blade at about the 40% chord position; due to the nonuniformity of the flow it actually intersects the upper blade at between 60 and 80% of chord. (See Figures 14a and 14b.) The rotor flow field upstream of this wave front converges rapidly to an essentially steady solution, whereas the stator is subjected to sequence of perturbations which travel both upstream and downstream and, therefore, converge to a periodic solution somewhat more slowly. The calculation was carried out for one complete revolution of the rotor, which required about 30 minutes of CDC 7600 computer time, using a grid network consisting of 12 grid columns and 9 grid rows in each of 5 domains. Approximately 1/4 of a revolution (500 time steps) was required to achieve an asymptotic solution in the rotor passage, and about 1/2 revolution (1000 time steps) should have been sufficient to attain an asymptotic solution in the stator. Unfortunately, a minor coding error in the application of the phased boundary conditions was not discovered until 3/4 of a revolution (1600 time steps) had been computed. Upon correction, a periodic solution was achieved during the last 1/4 of the revolution. The entire solution was not repeated due to the computing time requirement.

Provision to integrate the surface pressure distributions to obtain normal force and moment coefficients was not included in the code, making display of

the periodic solution rather cumbersome. Therefore. the pressure difference across the blade at the midchord point has been selected to represent the blade force. The midchord pressure differential across the stator is shown in Figure (19) for a period covering approximately the last 1/4 of the rotor revolution. Presence of a periodic solution formed by superposition of two very distinct waves is apparent. One wave appears to have a peak-to-peak frequency twice the rotor passing frequency, and the other has a peak-to-peak frequency twice the stator passing frequency (relative to the rotor). Fourier analysis of the solution over the period of 1/2 a revolution would be required to quantify the spectral components of the blade row interaction field.

As indicated above, the asymptotic flow field upstream of about the midchord position of the rotor should be steady in the rotating frame of reference of the rotor. However, as can be seen in Figure (20), a periodic pressure differential across the rotor midchord location is obtained, and in fact even the inlet pressure distribution exhibits periodicity in the rotating coordinate system. However, the amplitide of these oscillations is much smaller than those found in the stator. In view of the noted supersonic character of the relative flow through the rotor, these oscillations must be attributed to numerical propagation. Once the oscillations produced by the stator reach the leading edge of the rotor they are correctly able to propagate upstream, since the axial velocity component is subsonic. This spurious numerical propagation could be eliminated by observing the correct domain of dependence in formation of the difference operator, along the lines of the type-dependent difference operator used in the relaxation method developed by Murman and Cole[2].

SUMMARY AND RECOMMENDATIONS

A numerical method of solution for inviscid, transonic flow through a set of interacting cascades has been described in detail. Particular attention has been devoted to the statement and method of implementation of boundary conditions. The solution algorithms employed at the interior and boundary points of the computational grid have been described in detail.

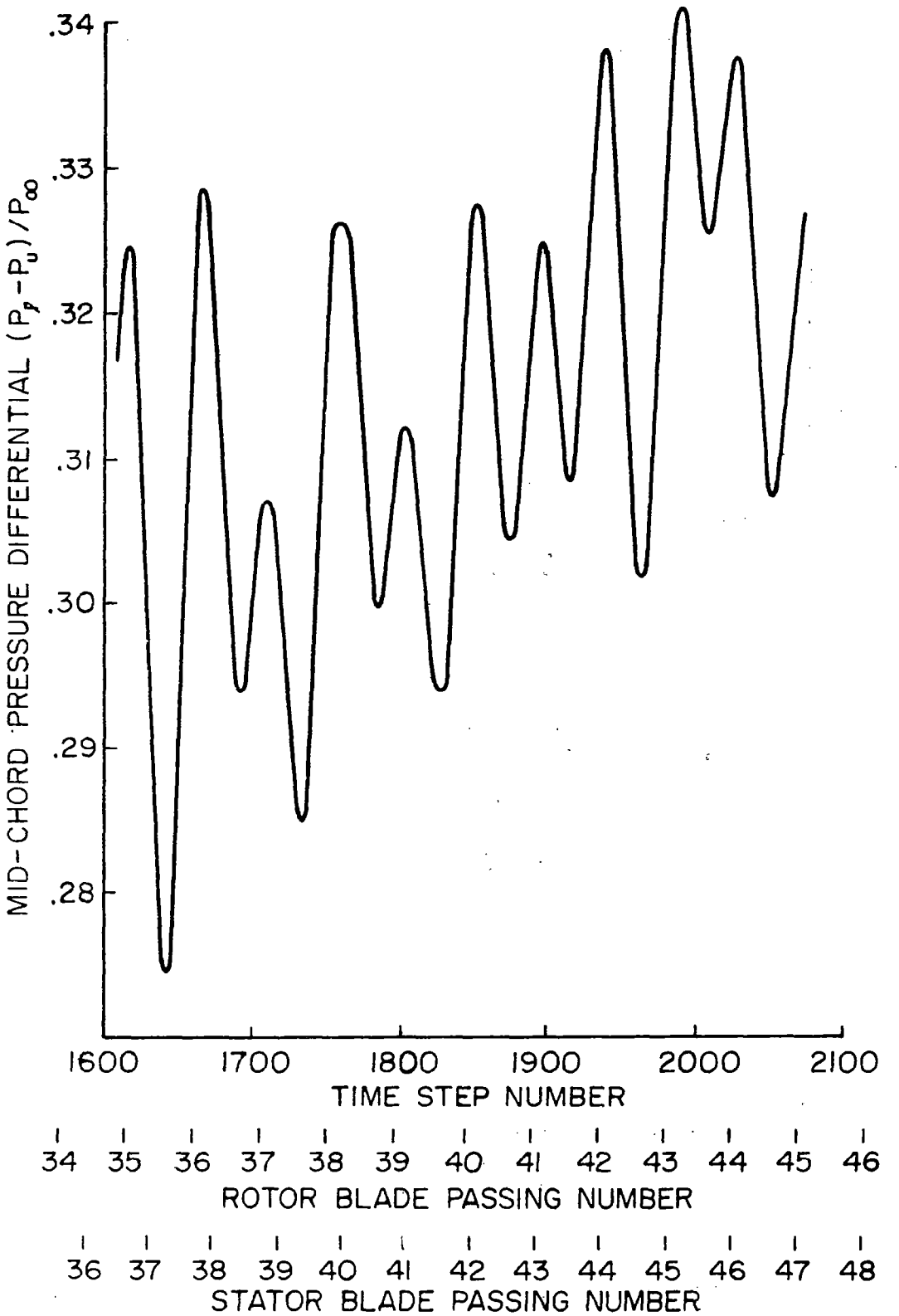

FIGURE 19 STATOR MID-CHORD PRESSURE DIFFERENTIAL DURING QUARTER REVOLUTION OF ROTOR

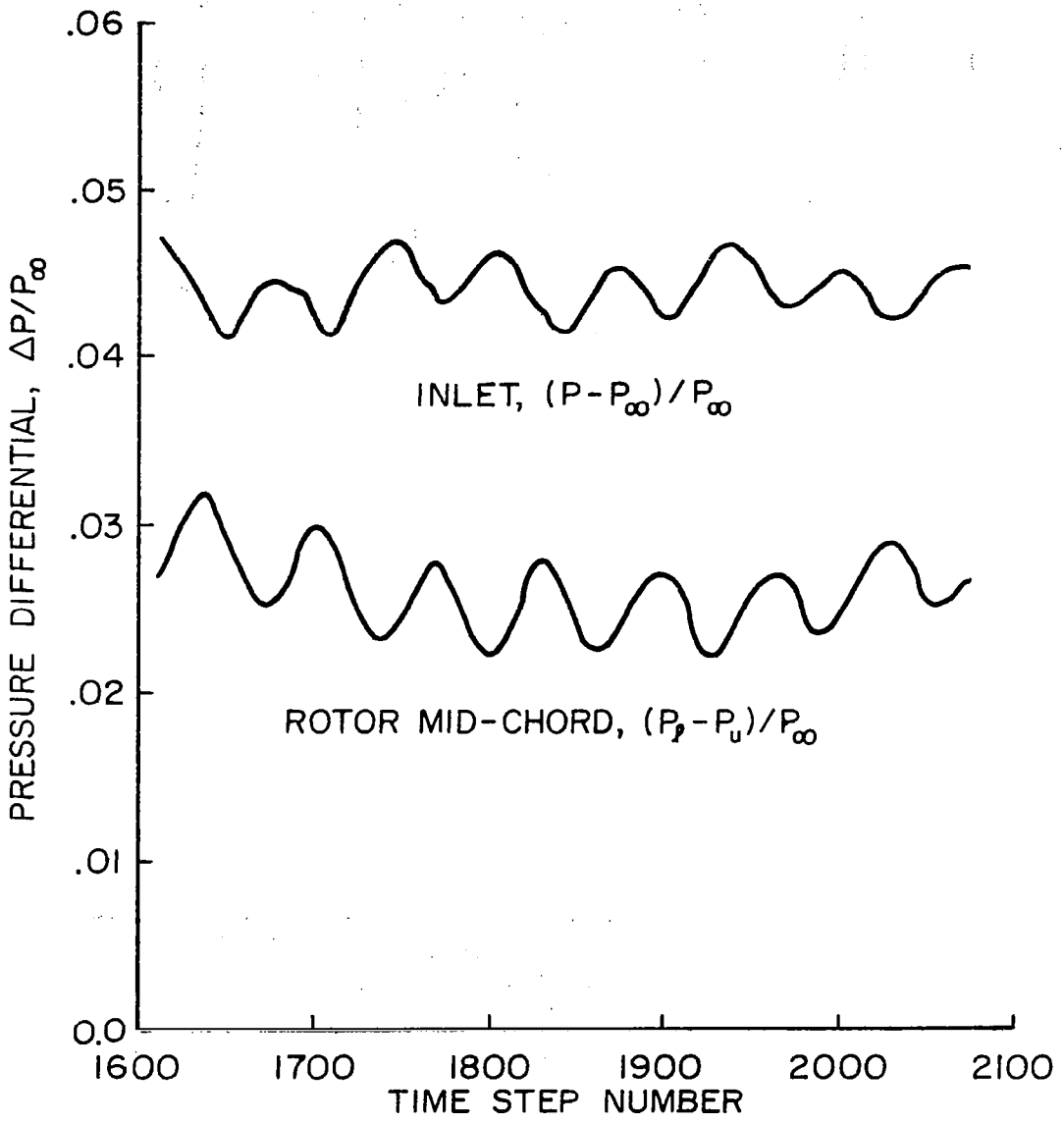

FIGURE 20. PRESSURE VARIATIONS AT ROTOR MID-CHORD AND AT INLET DURING QUARTER REVOLUTION

Several numerical examples have been carried out to demonstrate the capabilities and limitations of the present method. For example, a sharp blade leading edge is assumed in the present model. Comparison with a relaxation method solution for a stator blade row having blades with small but finite leading edge radius and operating under subcritical, transonic flow conditions indicates that the effect of nose bluntness is felt over the first 5 to 10% of the chord, which represents 10 to 20 nose radii for this case. In addition, comparison with experimental transonic rotor data indicates that the leading edge shock is generally stronger than that obtained from the present analysis, which is attributable to neglect of the nose radius. Thus, the range of applicability and degree of accuracy of the present computational model could be enhanced by inclusion of finite nose radius. However, the accuracy of the solution over the major portion of the chord length, under subcritical flow conditions, was found to be quite good with only 9 grid rows used from blade-to-blade; obviously it could be further improved by a finer grid network.

Examination of several transonic rotor solutions for "started" operating conditions indicates generally good agreement with the overall shock system structure; however, boundary layer separation effects on the blade surface, evident in the data, produce local departures from the predicted shock structure. A significant disparity between theory and experiment was encountered at a high back pressure operating condition. In this case, the present analysis produced a normal shock across the passage near the trailing edge of the lower blade, whereas holographic visualization showed a normal shock at the leading edge of the upper blade, i.e., the rotor was in an "unstarted" operation mode. This condition has been attributed to one or more observed effects of the three-dimensionality of the actual flow field, namely: presence of a shock off the midspan vibration damper, and of the blade tip vortex. Although not explicitly observed, separation of the end wall boundary layer may also contribute to the disagreement between the present two-dimensional analysis and the experimental observations in this case.

A transonic rotor-stator interaction case was carried out for one full revolution of the rotor. Unfortunately, any conclusions regarding the rate of convergence to a periodic solution were compromised by the presence of a minor cod-

ing error which was not detected during the first 3/4 of the rotor revolution. A periodic solution was obtained in the stator during the final 1/4 revolution, upon correction of the error. The rotor solution became asymptotic within the first 1/4 revolution, in accord with the rate of convergence of the isolated rotor cases. Integration of the instantaneous surface pressure distributions to obtain normal force and moment coefficients would facilitate interpretation of the results and is, therefore, recommended as well as Fourier analysis of these coefficients to identify attainment of an asymptotic state and to characterize the spectral content of their temporal variation. Additionally, numerical propagation of periodic disturbances through a supersonic portion of the rotor passage, which on the basis of the mathematical zones of influence should have been inaccessible to upstream travelling waves, has been noted. Alteration of the finite difference operators to eliminate or at least minimize spurious upstream propagation through supersonic zones by correctly observing the mathematical domains of dependence of the grid points is also suggested.

Testing of the influence of the blade boundary layer and wake models and of the acoustic far field boundary conditions was not included in the present investigation due to time and budgetary limitations. In view of the above mentioned areas in which further improvement of the inviscid analysis is considered warranted, continued developmental work appears necessary to fully achieve the predictive capability of the present method of analysis. Determination of viscous and acoustic far field effects may logically be regarded as part of this next level of development.

APPENDIX

TREATMENT OF VIRTUAL BOUNDARIES

Periodic Boundary Conditions

In order to clearly describe application of the periodic boundary conditions in the present analysis it is useful to illustrate the discussion by introducing several rotating devices that demonstrate certain general concepts with minimal complexity of the geometric configuration. First, consider a symmetric three bladed rotor developed into a cascade as shown in Figure (A1):

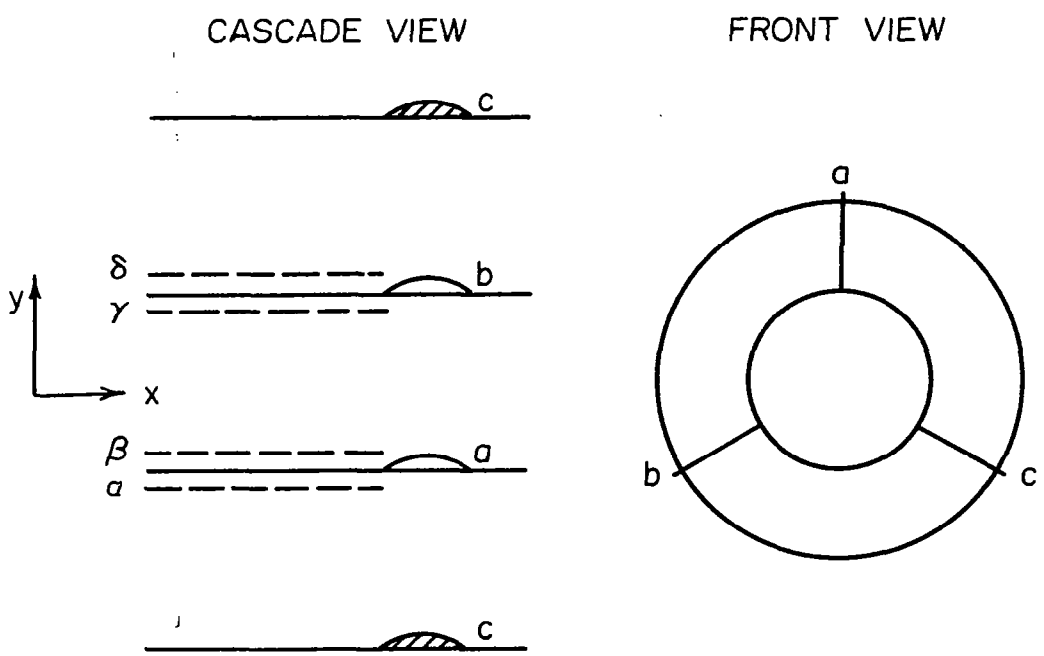

FIGURE AI. ISOLATED BLADE ROW

Let virtual boundaries* of the blade-to-blade passages be drawn from the blade leading and trailing edges to $\pm\infty$. In a reference frame fixed to the blades it

*These sufaces are not, in general, coincident with streamlines; flow can cross them and disturbances can propagate along and across them.

is clear that the flow field in each of the three passages must be identical if the blades are identical and the inlet and discharge boundary conditions are uniform and steady. Therefore, at any instant the flow is circumferentially periodic. The flow along line δ is identical to the flow at the spatially equivalent points on line β. The flow along lines α and γ is also obviously equivalent at any instant. The same argument also applies to points in the flow field downstream of the blades.

Next consider the system composed of a rotor and stator each having the same number of blades; specifically, consider 3 blades each as shown in Figure (A2).

When the blades are aligned, say at time t_o; as shown in Figure (A2a), it is clear that, because symmetry produces identical flow channels, the flow along and through the virtual boundaries extending from x and between leading and trailing edges is the same in each "passage"; i.e., all influences with respect to corresponding points in the respective "passages" are necessarily the same. For a different relative position, say at some later time $t_o + \Delta t$ for example, see Figure (A2b), the noted symmetry persists since the geometry of respective "passages" is the same and again the flow through the respective control volumes is identical. The same conclusion as above is also reached regarding the equivalence of lines α with γ and δ with β. The same argument again can be applied to the flow field between the two blade rows and also downstream of the second blade row.

It is noted that due to the repetition of identical configurations with identical flows it is clear that only one passage of each blade row need be computed in order to determine the flow field in the whole periphery of the stage. As a consequence of the equivalence of the corresponding interior and exterior grid rows, it is also clear that the boundary values, say on exterior line δ, can be specified by equating them to the currently computed values at corresponding interior points, in this case on line β, to enforce the periodic boundary conditions for the passage being computed. The same reasoning is applied to lines γ and α, and to corresponding virtual boundaries between and downstream of the blades.

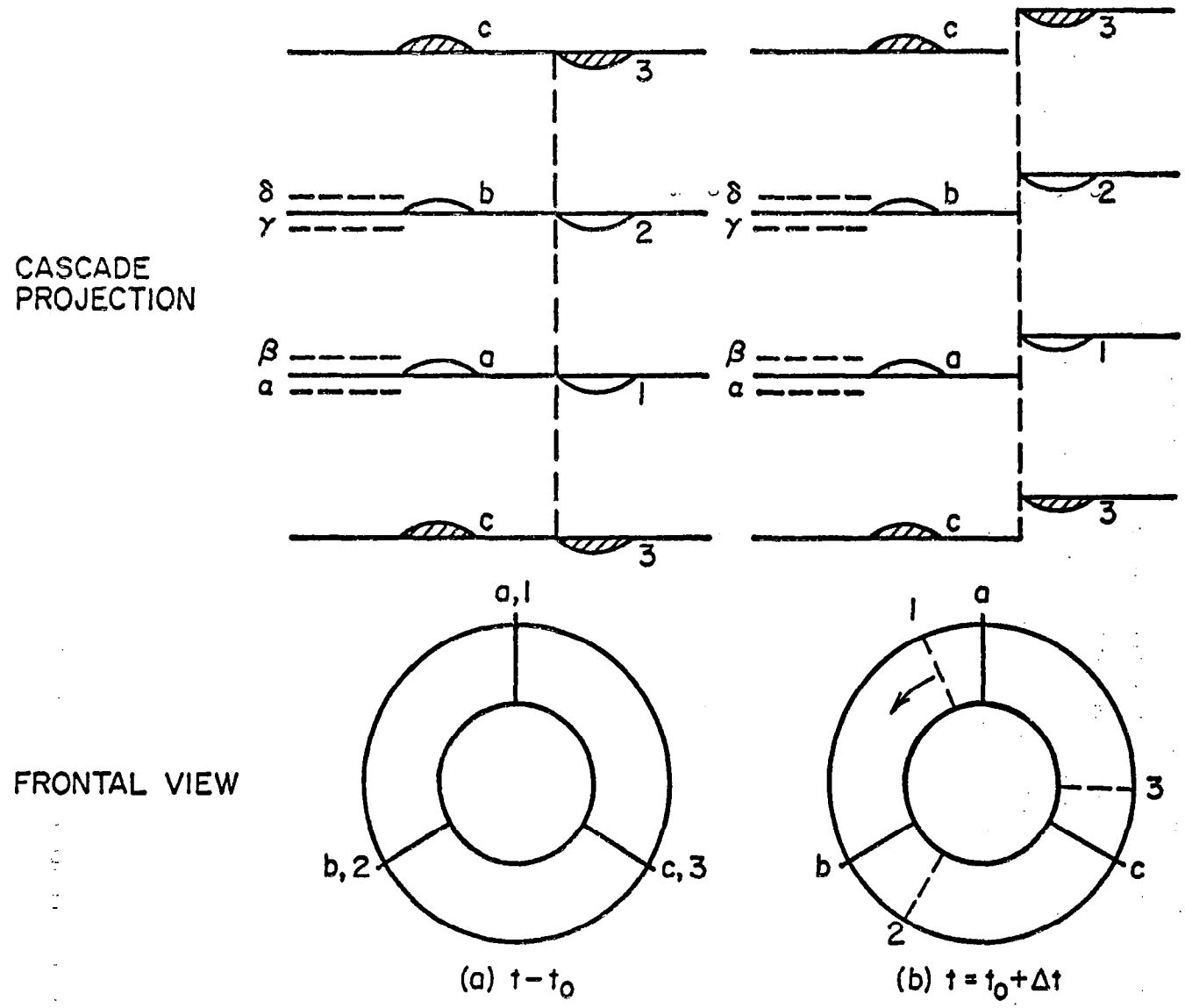

FIGURE A2. ILLUSTRATION OF CYCLIC ALGORITHM FOR STAGE WITH EQUAL NUMBER OF BLADES IN STATOR AND ROTOR ($N_1 = 3$, $N_2 = 3$)

It is not obvious that the case of an unequal number of blades in the stator and rotor can be treated analogously; however, the following detailed explanation is intended to demonstrate clearly that the above techniques for specifying boundary conditions on a single passage can be extended to this case by introduction of a phase shift. In this regard a pair of blade rows, shown in Figure (A3a) and (A3b) portray the configuration of a 3 bladed stator followed by a 4 bladed rotor which will be used to demonstrate the unequal spacing techniques.

The underlying assumption here is that the inlet and discharge boundary conditions applied upstream and downstream of the stage are uniform and steady, and that the non-steady flow in the vicinity of the stage is stably periodic in time. The first question that arises is whether the starting process associated with an arbitrary set of initial conditions can lead to an asymptotically periodic solution through use of the above-described numerical procedure for treating spatially periodic boundary conditions. It is useful in this regard to pictorially describe the physical starting process for a system of blade rows set into motion impulsively. This is done for the configuration introduced above with both the rotational speed and free stream velocity subsonic. Figures (A4a) to (A4m) show the development of a disturbance wave system thus generated. Only those waves generated when a blade of the rotor is aligned with a blade of the stator are portrayed in these figures and then only a portion of each wave, extending a distance x_w, as shown in Figure (A4c), are shown for clarity. One complete revolution of the rotor, an angle of rotation of 2π, is represented over 12 intervals. The time increment for each interval is

$$\Delta t = \frac{2\pi}{N_1 N_2 \omega} = \frac{2\pi}{12\omega} \tag{A1}$$

where N_1 is the number of blades in the stator, N_2 is the number of blades in the rotor and ω is the rotational speed. The corresponding angular change for each Δt is

$$\Delta\phi = \frac{2\pi}{N_1 N_2} = \frac{2\pi}{12} \tag{A2}$$

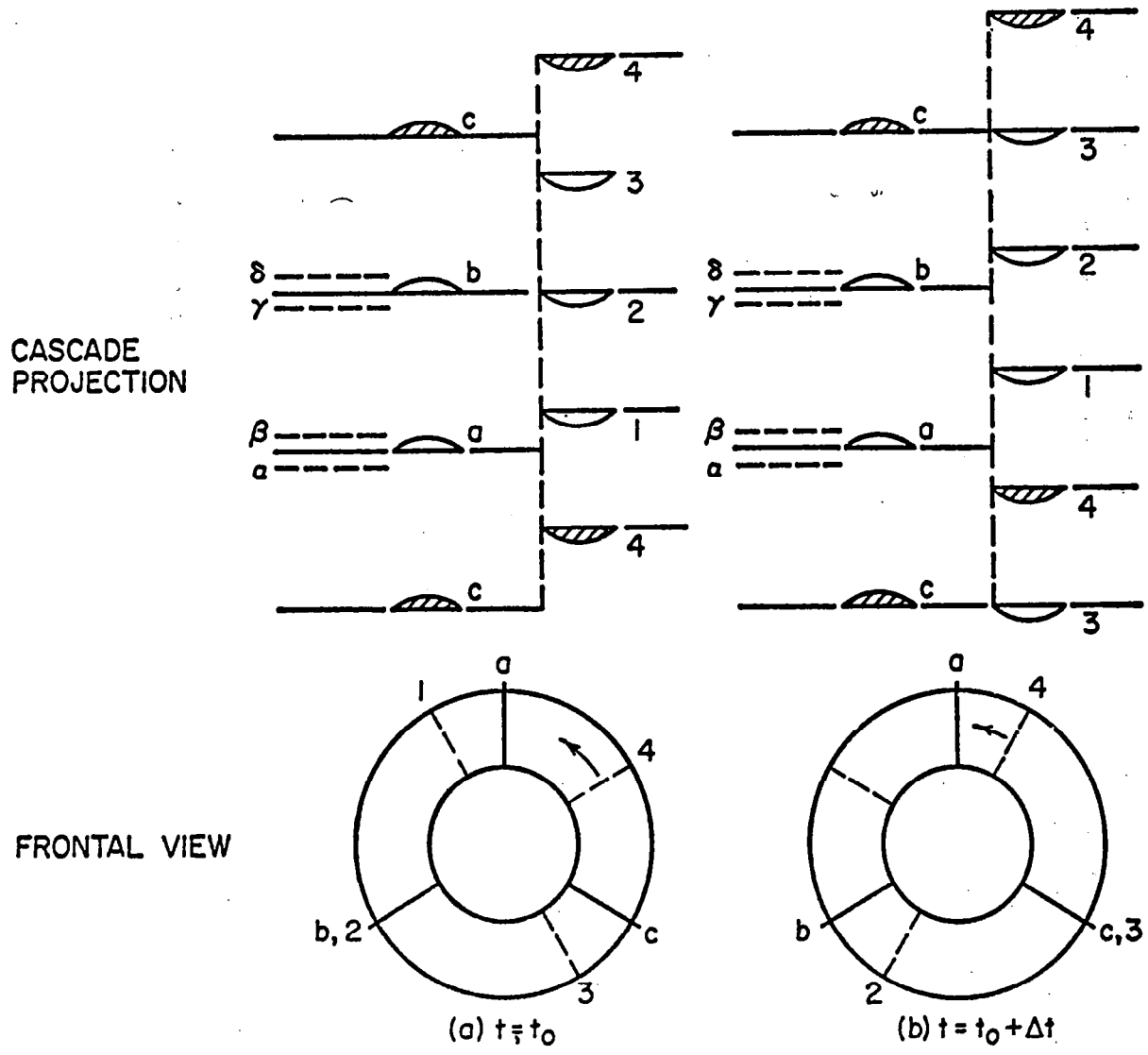

FIGURE A3. ILLUSTRATION OF CYCLIC ALGORITHM FOR STAGE WITH UNEQUAL NUMBER OF BLADES IN STATOR AND ROTOR ($N_1 = 3$, $N_2 = 4$)

Each time two blades are aligned, indicated by an arrow in Figure (A4a) through (A4m), a pulse, shown as a large dot at $x = 0$ above the alignment, is created; this pulse then travels out to form a cylindrical disturbance wave with increasing radius in time. Figure (A4a) has a pulse labelled (1) created at $t = 0$ where the two reference blades (cross hatched) are aligned. This pulse forms the wave, labelled (1) shown in Figure (A4b) after $\Delta t = 2\pi/(12\omega)$ or $\Delta\phi = 2\pi/12$, and a new pulse, labelled (2), is created where the next two blades are aligned (see arrow). These disturbances, (1) and (2), travel out to the positions shown in Figure (A4c) and a new pulse, labelled (3), is created where the next set of blades are aligned, (see arrow). The subsequent Figures (A4d) through (A4m) show the waves travelling out further and new ones being created similarly to Figures (A4a) through (A4c). The first three waves are identified in Figures (A4a) through (A4d) and (A4m). Figure (A4m) can be considered as an asymptotic picture where the wave front in the whole periphery at a distance of $x = (a-u) \cdot 12\Delta t$ is almost flat. If asymptotic configurations at three times are now considered, say at times t_o, $t_o + \Delta t$ and $t_o + 2\Delta t$, as portrayed in Figures (A5a) through (A5c), several important conclusions can be drawn. Consider first the geometry of the configurations. In Figure (A5a) the cross hatched reference or first set of blades are aligned (note the control volume indicated by the dot-dash border, •-•-, to the top and right of it). In Figure (A5b), representing a time Δt later, the next or second set of blades to the right are aligned (also note the corresponding control volume as described above). Finally, in Figure (A5c) $2\Delta t$ after reference time t_o the third set of blades are aligned (this also corresponds to the two blades at the far left of Figure (A5c), thus the control volume to the right of this set of blades shall be noted). Each of these dot-dash control volumes correspond to the same relative geometry and it can be seen by direct comparison that the asymptotic wave pattern is identical in each. The same thing is true at all other possible relative blade positions, (which implies all other times) that are encountered as the reference blade of the rotor moves through one complete blade spacing of the stator. It is thus possible to construct the entire asymptotic solution of the periphery at any one instant (and, therefore, at all instances) from all of the asymptotic periodic solutions at successive times found in one blade spacing control volume as the reference blade of the rotor travels through one blade spacing of the stator.

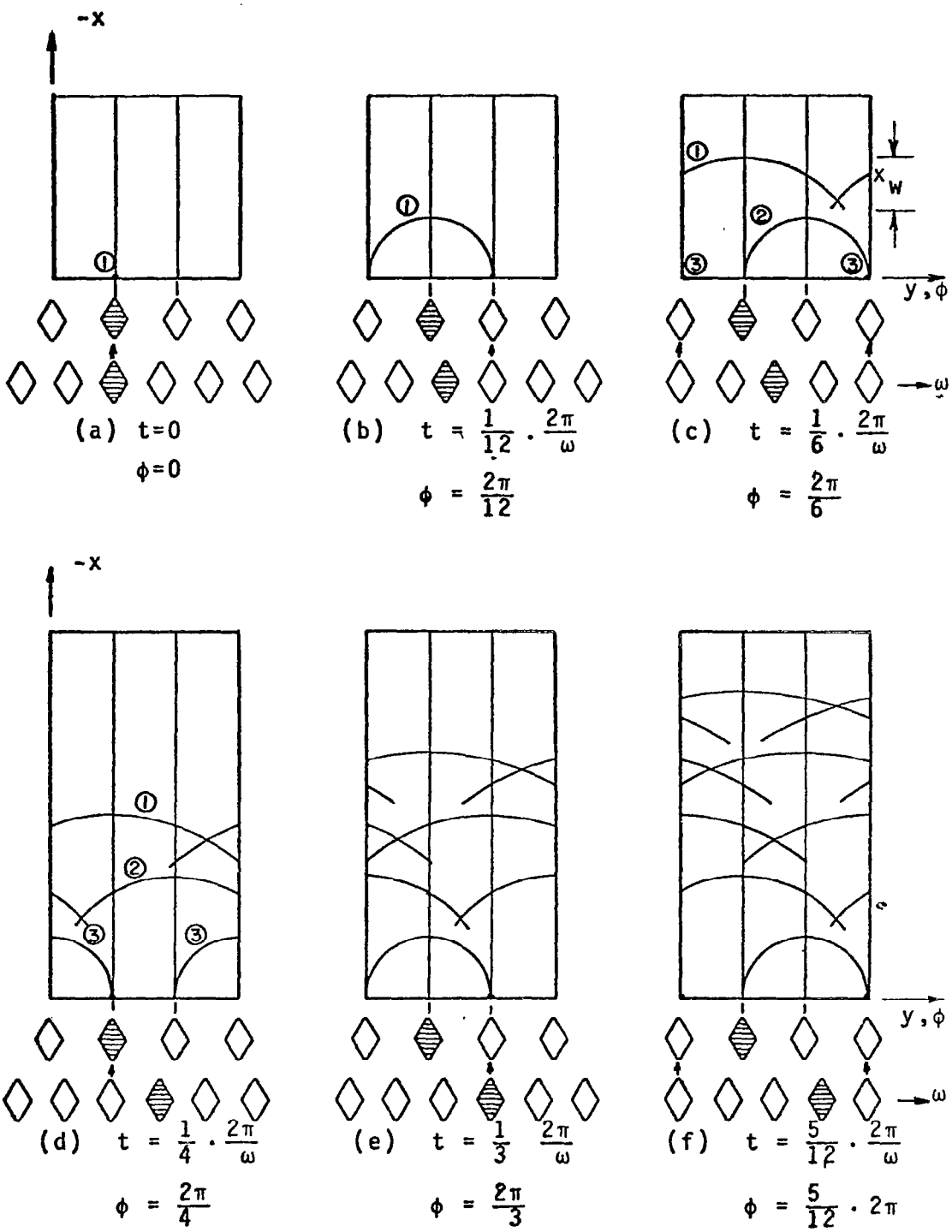

FIGURE A4. STARTING PROCESS SHOWING DEVELOPMENT OF DISTURBANCE WAVES FORMED WHEN BLADES ARE ALIGNED (ACTUAL SOLUTION)

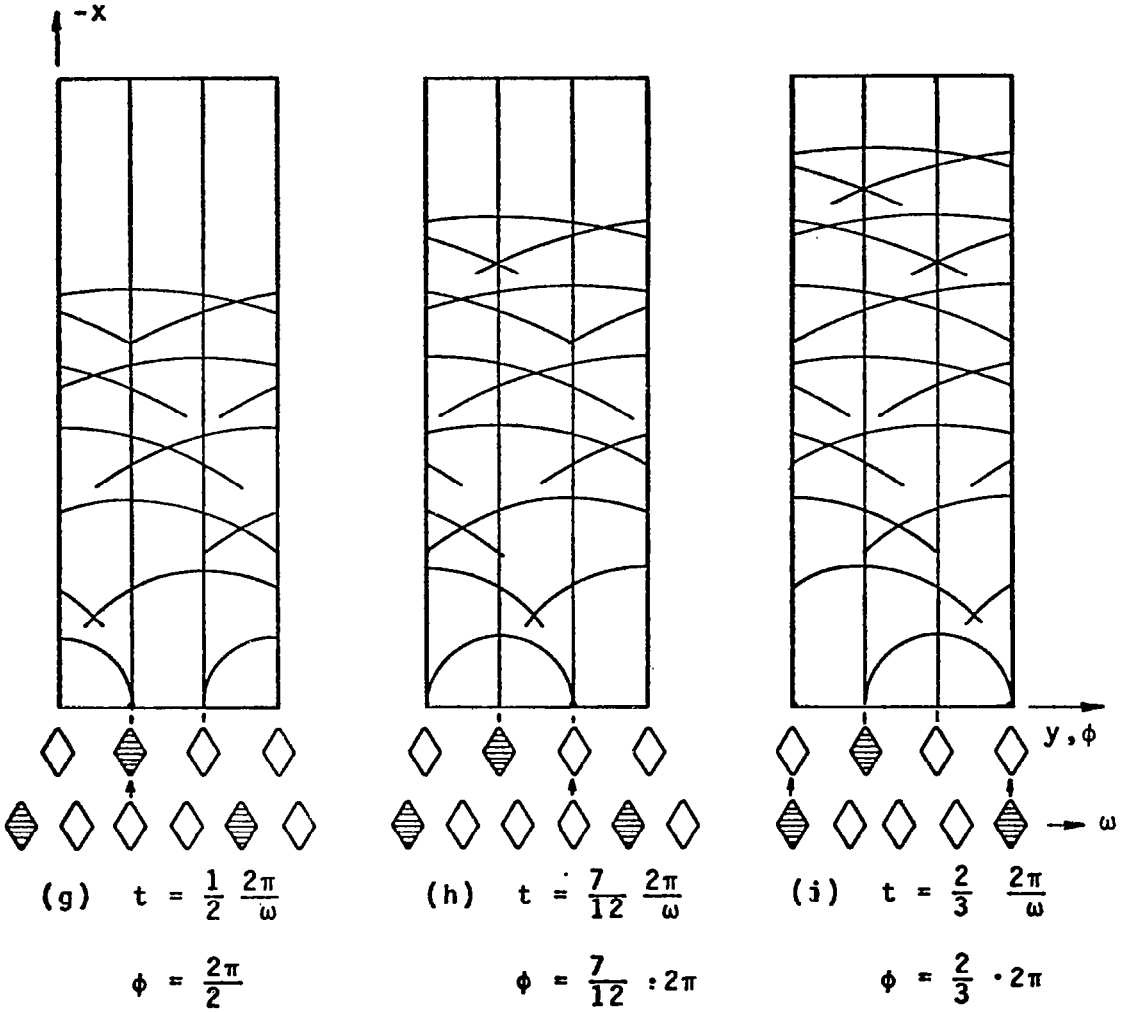

FIGURE A4. (CONTINUED)

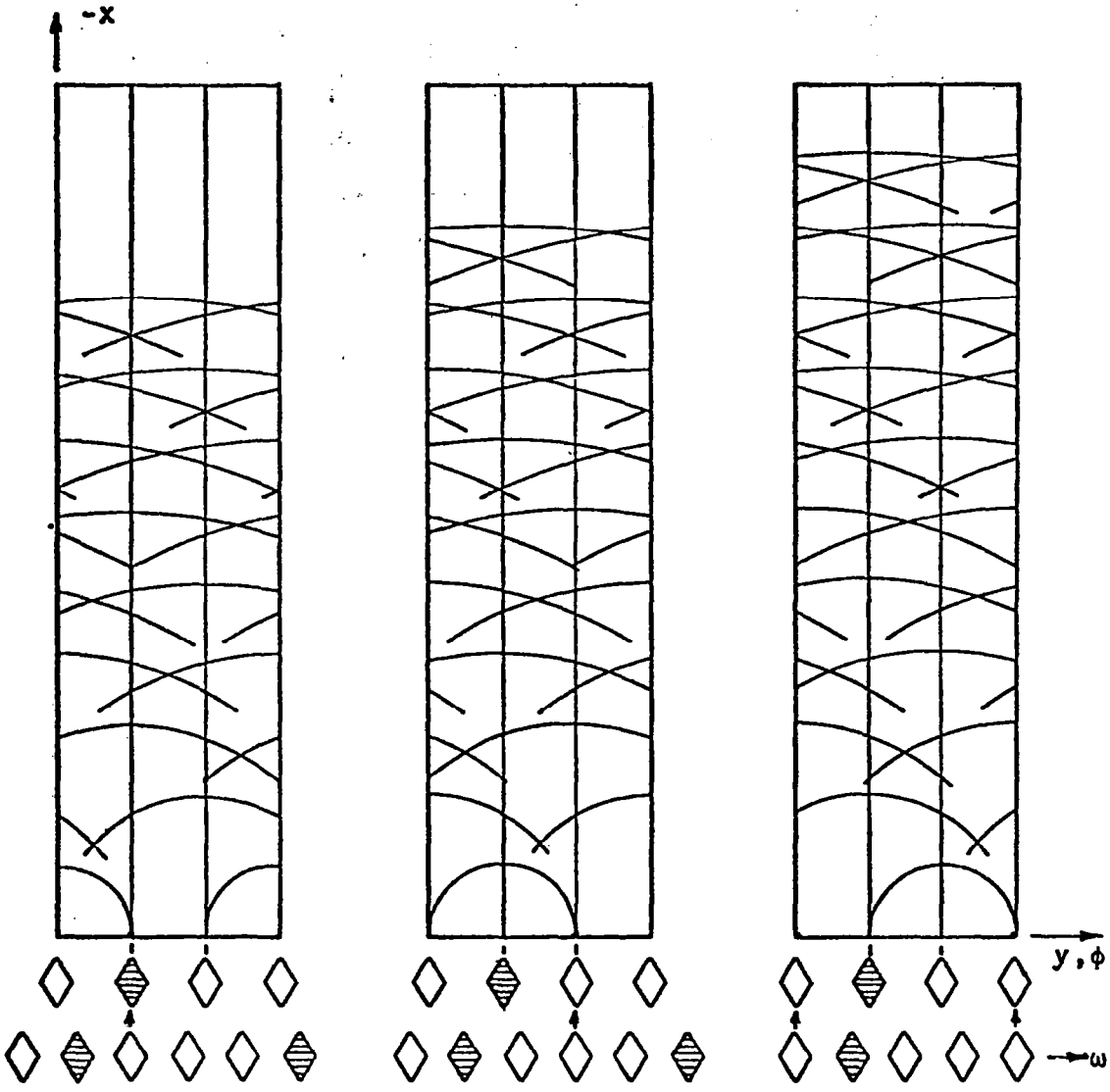

(j) $t = \frac{3}{4} \cdot \frac{2\pi}{\omega}$ $\phi = \frac{3}{4} \cdot 2\pi$

(k) $t = \frac{5}{6} \cdot \frac{2\pi}{\omega}$ $\phi = \frac{5}{6} \cdot 2\pi$

(l) $t = \frac{11}{12} \cdot \frac{2\pi}{\omega}$ $\phi = \frac{11}{12} \cdot 2\pi$

FIGURE A4. (CONTINUED)

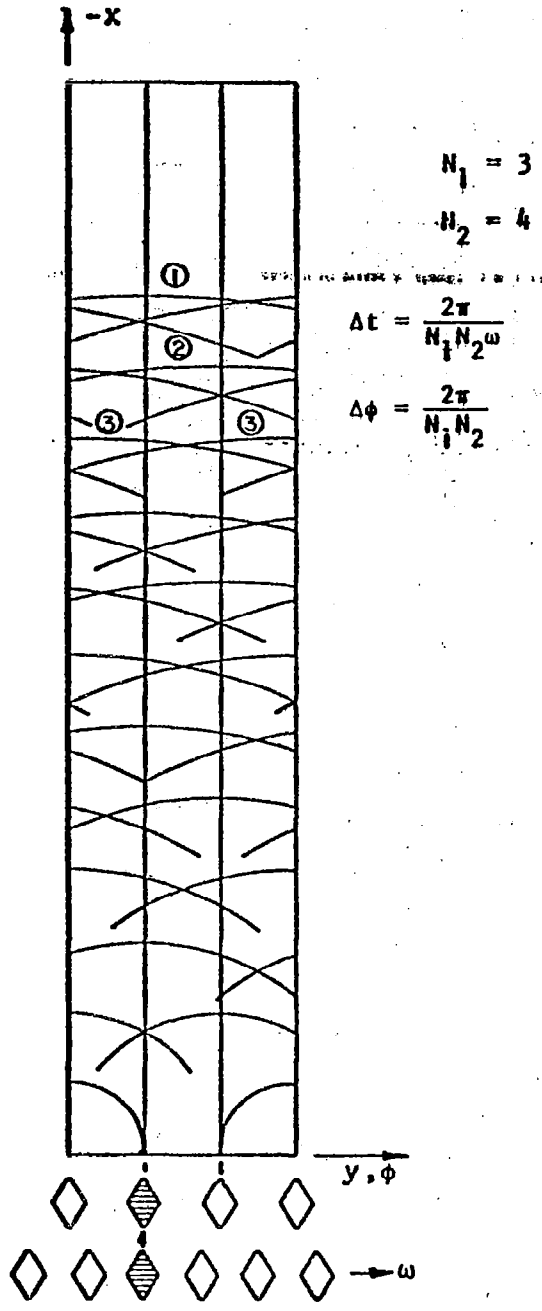

(m) $t = \frac{2\pi}{\omega}$

$\phi = 2\pi$

FIGURE A4 (CONTINUED)

Next consider the dash-dash, ---, control volume always lying to the right of the stator reference blade. This is the reference control volume within which all solutions for the flow upstream of the stator will be found as a function of time. Consider now the asymptotic wave pattern which would be found to the right of the reference control volume at time $t_o+2\Delta t$ in Figure (A5c). It is obvious that it is identical to the wave pattern within the reference control volume in Figure (A5b) at time $t_o+\Delta t$ or one Δt time step earlier (arrows "A"). Next consider the asymptotic wave pattern which would be found to the left of the reference control value at time $t_o+2\Delta t$ i.e., in Figure (A5c). Again it is obvious that it is identical to the wave pattern within the reference control volume in Figure (A5a) at time t_o or two Δt time steps earlier (arrows "B"). In view of this fact, the appropriate portions of the earlier solutions found in the reference control volume can be applied as boundary conditions to the reference control volume at the current time before proceeding with the computation for the next Δt. This is carried out, refer also to Figure (A3a) and (A3b), by equating the values at the first row of exterior grid points, say line δ, to the values that existed Δt time step earlier at corresponding points, in this case line β, when the geometrical configurations with respect to lines α and β were the same. A similar procedure is carried out for lines α and γ with its own phase lag. In addition, all other horizontal boundaries (those between the blade rows and downstream of the rotor) and vertical boundaries which require phase lags for proper specification are specified analogously. These vertical boundaries are on the downstream side of domain 4 and the upstream side of domain 5.

Consider now the starting process for the computational model. Figure (A6a) through (A6m) portrays the computational starting problem comparable to the actual physical one shown in Figure (A4a) through (A4m). The successive application of the boundary conditions in this manner puts a numerical phase lag into the solution through the imposed boundary conditions as the computation is started. As in the actual physical starting process discussed earlier, blade alignment, indicated by an arrow between blades, produces a pulse, indicated by a dot and identified in the first three waves in the Figures (A6a) through (A6d) and in Figure (A7m). Initially there are no previously computed boundary conditions with phase lag to apply, hence, the "tagged" disturbances created in the reference control volume are of minimal accuracy and as such

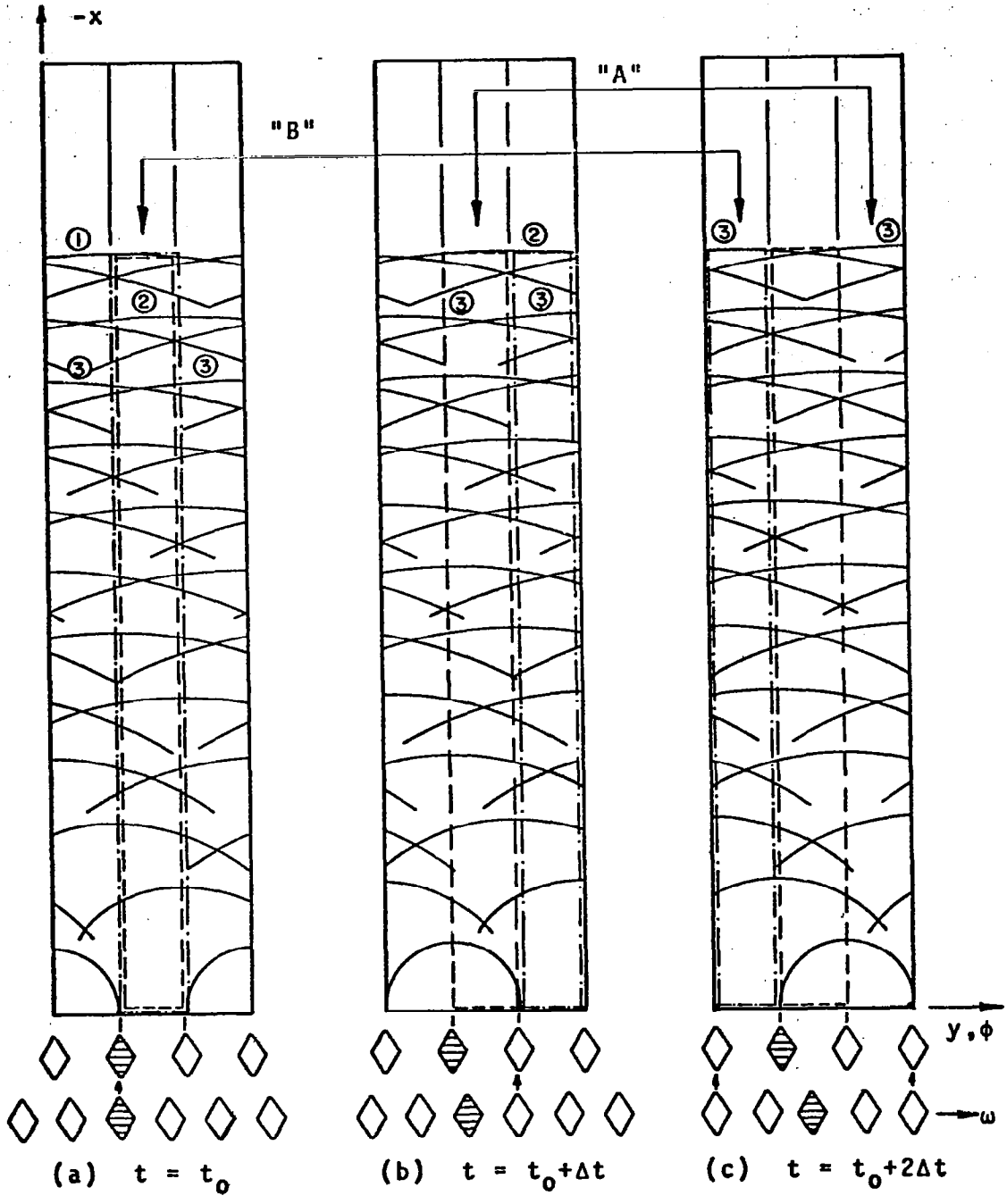

FIGURE A5. ASYMPTOTIC DISTURBANCE PATTERNS GENERATED WHEN A ROTOR BLADE IS ALIGNED WITH A STATOR BLADE.

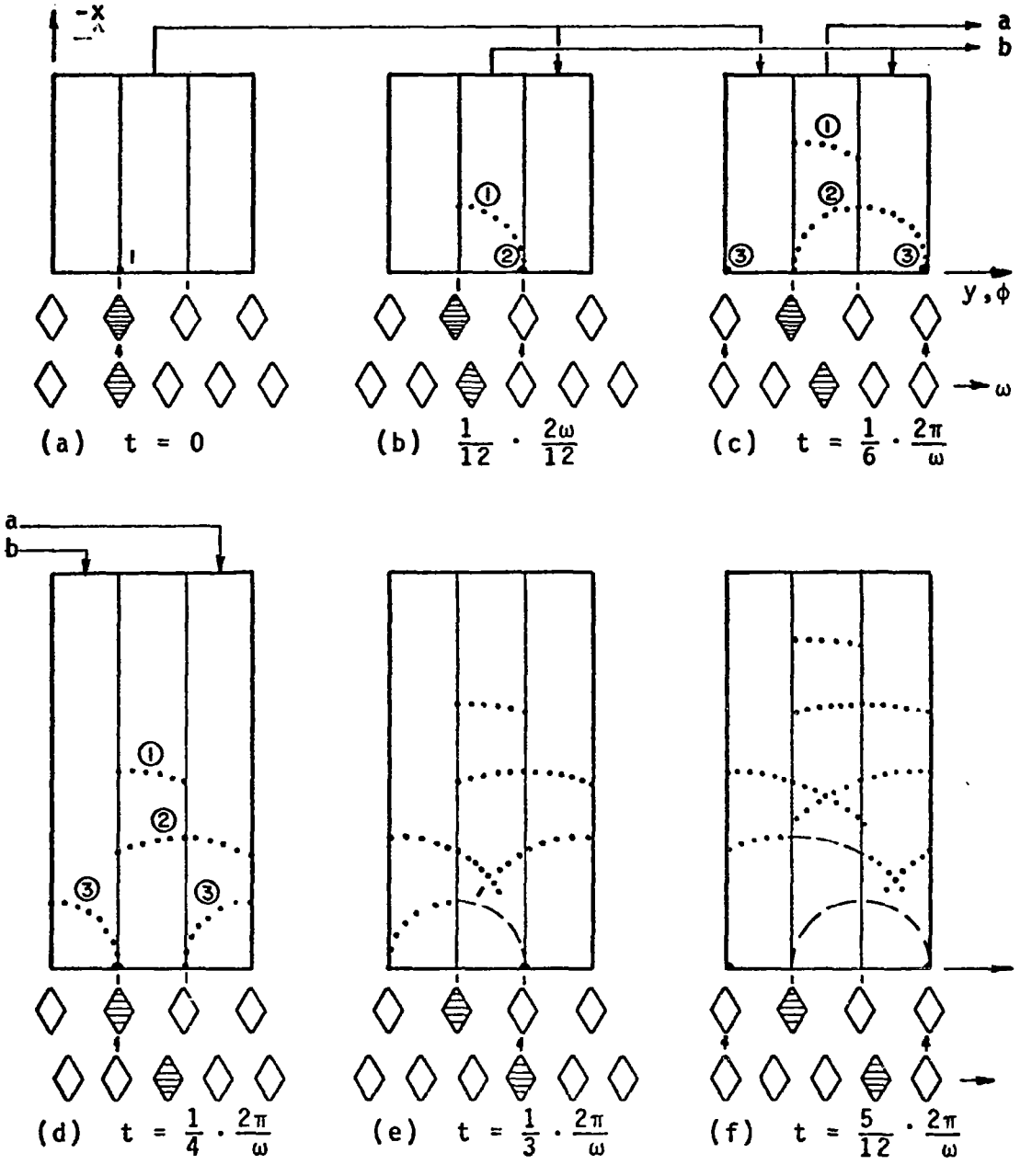

FIGURE A6. STARTING PROCESS SHOWING WAVE DEVELOPMENT OF DISTURBANCE WAVES FORMED WHEN BLADES ARE ALIGNED (SOLUTION WITH BOUNDARY CONDITIONS HAVING PHASE LAG).

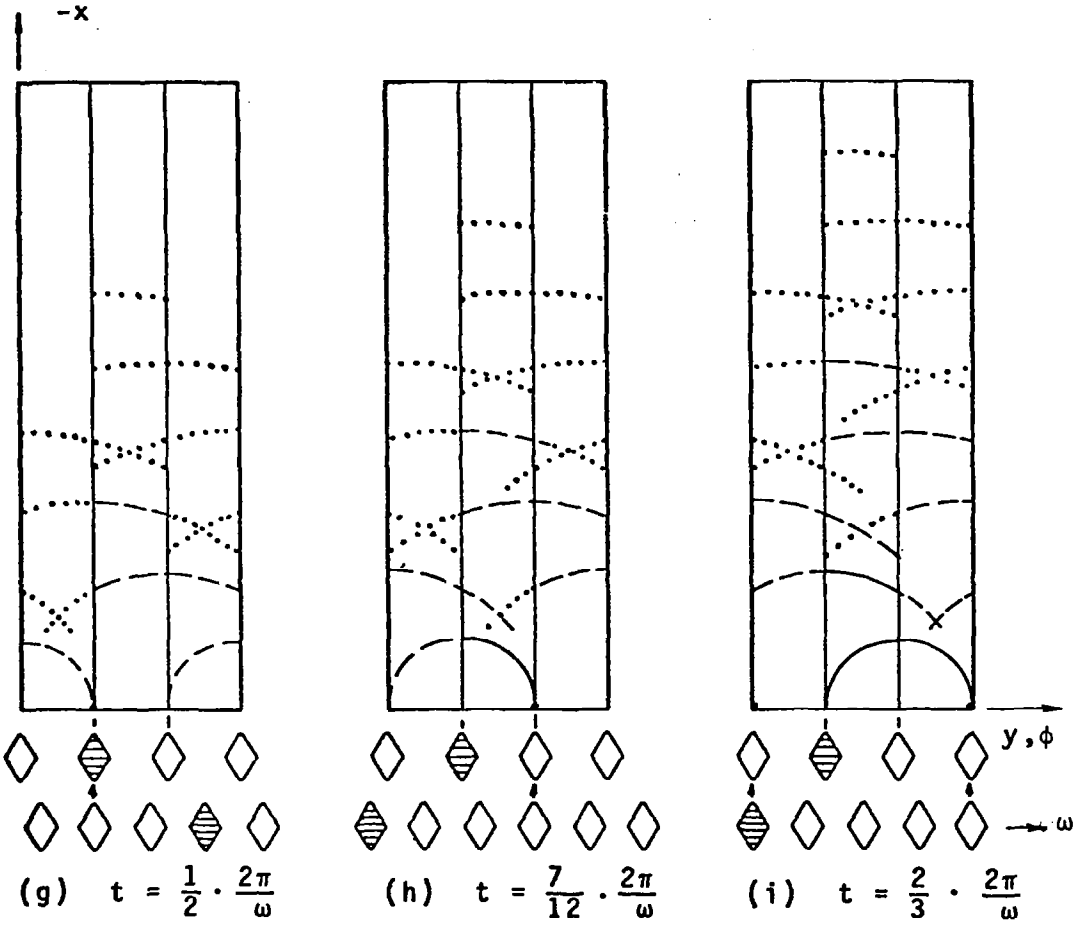

FIGURE A6. (CONTINUED)

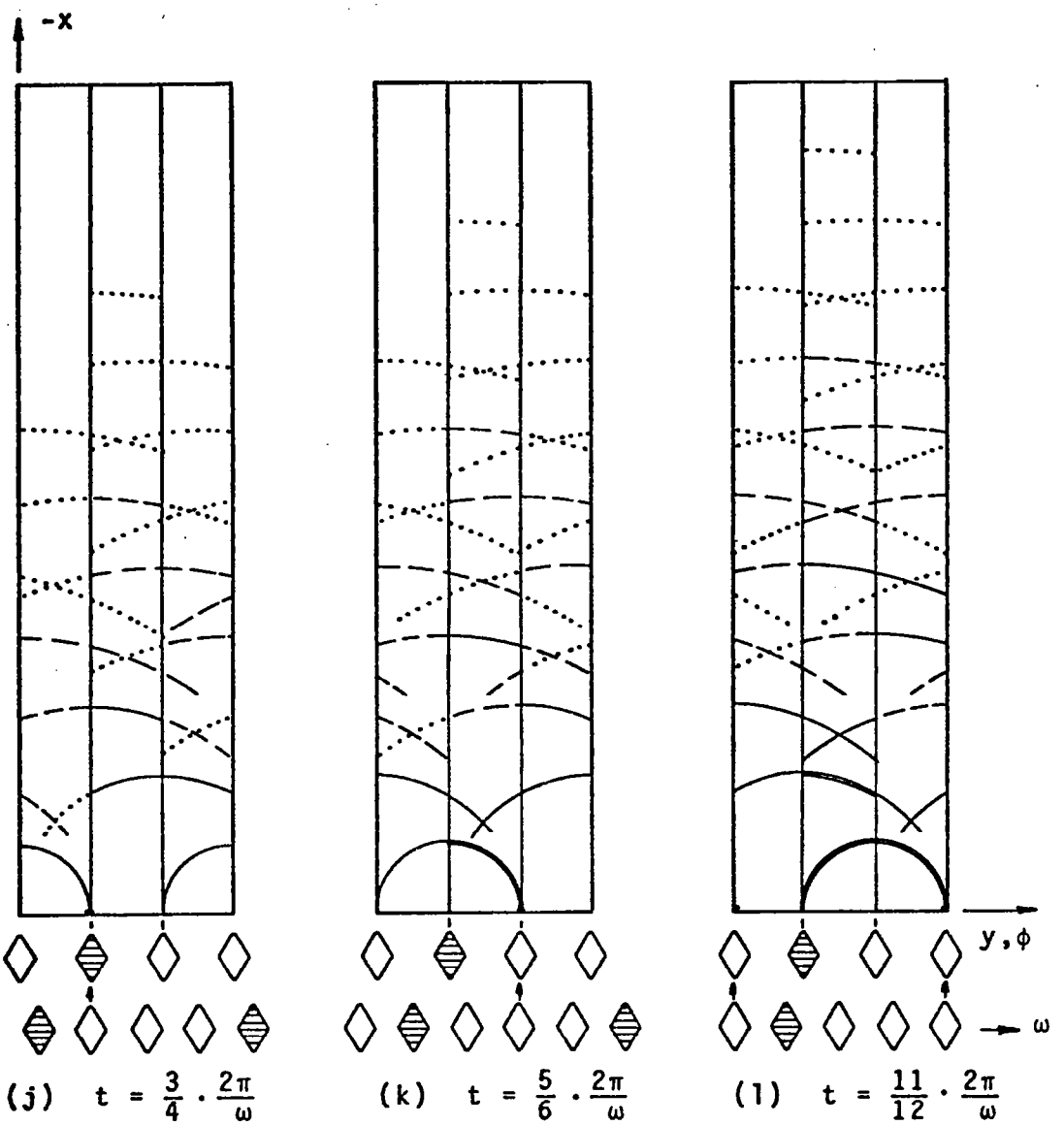

FIGURE A6. (CONTINUED)

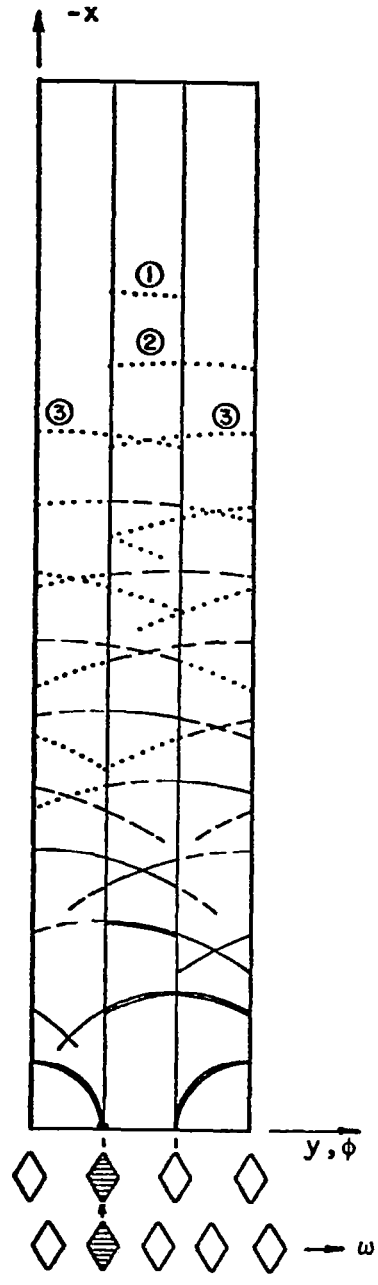

(m) $t = \frac{2\pi}{\omega}$

FIGURE A6. (CONTINUED)

are indicated by using dotted curves. When a more accurate boundary condition is available, i.e., when each side of the reference control volume can be specified from the solution at an earlier time, the accuracy of the solution within the control volumewill be improved. This is indicated by dashed lines, as for example in Figures (A6e) and (A6f) etc. The boundary conditions with phase lag are applied as already discussed previously and the arrows in Figures (A6a) through (A6d) give examples of the phase lag for several cases. As the solution proceeds in time it also becomes more accurate due to the repeated application of increasingly accurate boundary conditions; this is indicated schematically by an increasing solidity of the lines depicting the wave fronts in Figure (A6).

Ultimately all solutions of lesser accuracy propagate out of the computational domain and only the increasingly more accurate disturbances remain. The result is that the waves associated with the approximated starting process are lost and the solution becomes asymptotic in the same fashion as shown in Figures (A5a) through (A5c). The criterion which determines the improvement is not the angular distance that the rotor has travelled, but is the number of times the boundary conditions have been applied; consequently, the larger the number of blades, the better is the solution after a complete revolution of 2π. An asymptotically periodic solution should be attained when successive solutions at the interior points possess periodic relationships and phase lags with respect to each other which precisely match those imposed by the application of boundary conditions at the virtual grid points.

Horizontal Boundaries

The "horizontal" (i.e., streamwise) boundary points are specified by the technique discussed above which is based on the fact that these surfaces are "planes of equivalence" with a phase lag. Figure (A7) shows a typical domain. A row of "virtual" grid points in this case k = 2 and k = KS+2 is placed one mesh point outside the calculation domain; at these points the flow conditions are equated to those existing at corresponding grid points one mesh point inside the opposite boundary, in this case K = KS-1 and K = 5 respectively, at a time when the blade positions at that opposite boundary were the same as currently exist along the subject boundary. (The double-valued boundary rows

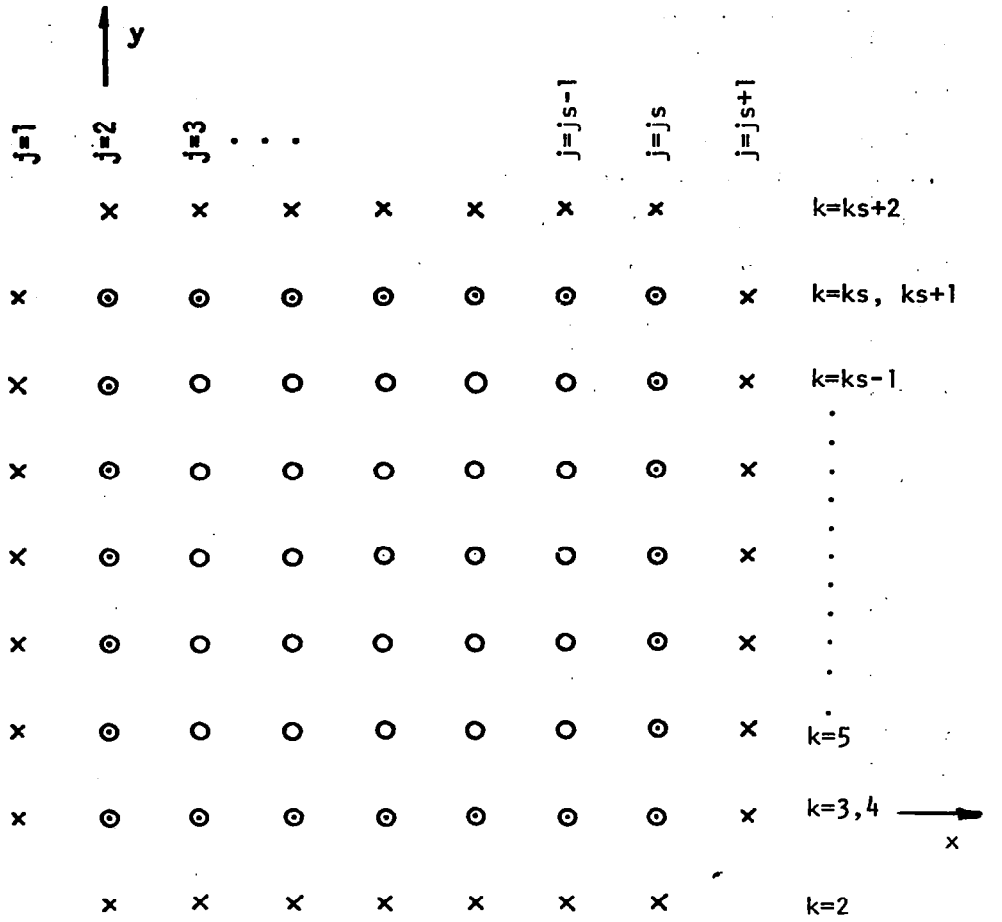

o Interior Point

⊙ Boundary and Interior Point

× Exterior or Virtual Point

FIGURE A7. SCHEMATIC OF A TYPICAL TRANSFORMED SQUARE DOMAIN

K=3, 4 and K=KS, KS+1, have been introduced to account for jumps in properties across the slipstreams.)

Specification of the phase lags for these horizontal boundaries is described as follows. Let there be N blades in the upstream blade row and M blades in the downstream blade row with $N \leq M \leq 3N/2$. Also let n be the number of time steps required for one blade spacing of the larger pitch to be traversed and m the number of time steps required for the smaller pitch to be traversed. Then:

$$Nn = Mm \tag{A3}$$

There are four sets of boundaries to be considered:

A. The upper boundary of domains 1, 2 and 4, adjacent to K=KS, KS+1.

B. The upper boundary of domains 6 and 7, adjacent to K=KS, KS+1.

C The lower boundary of domains 1, 2 and 4, adjacent to K=3, 4.

D. The lower boundary of domains 6 and 7, adjacent to K=3, 4.

The specific phase shifts are as follows:

(1) Set A at K=KS+2 = Set C at K=5 (n-m) time steps ago

(2) Set B at K=KS+2 = Set D at K=5 (n-m) time steps ago

(3) Set C at K=2 = Set A at K=KS-1 (m-(n-m)) time steps ago

(4) Set D at K=2 = Set B at K=KS-1 (m) time steps ago

The values computed at every time step at K=5 and KS-1 must, therefore, be stored for later use. Since a considerable number of time steps are involved, this cannot be done using core storage and is done instead by disk or tape storage and recall in a non-random method.

Virtual grid rows K=1 and K=KS+3 are required in domains 4, 6 and 7 to evaluate the spatial derivatives needed at K=2 and K=KS+2 in the characteristic solutions along the slipstreams. The procedure to define the solution at these exterior rows follows exactly the format outlined above, e.g., Set A at K=(KS+3) is equated to Set C at K=6 (n-m) time steps ago.

Entrance and Exit Boundaries

Solutions at the virtual grid points on vertical boundaries J=1 and J=JS+1 in Figure (A7) (except, of course, the inlet and discharge stations which are true boundaries rather than virtual boundaries) are linearly interpolated from the data in adjacent domains. Refer to Table AI for the following discussion for specific distribution of data at equivalent vertical boundaries. It is to be noted that in order to obtain spatially equivalent grid points for the vertical boundaries between domains 4 and 5 account must be taken of the relative motion of the domains; interpolation of data as well as application of phase shifts are required.

In the case of equal numbers of blades in adjacent rows, matching flow variables along the interface between domains 4 and 5 is straightforward; in any other case certain subtleties occur in the process of minimizing the computer storage and time requirements. Again a column of grid points external to domains 4 and 5 are considered. In the regions of overlap shown in Figures (A8a) and (A8b), it is clear that the exterior column of points from domain 4 overlaps the interior of domain 5, and vice versa. However, for the regions of "non-overlap" determination of the flow variables at these exterior grid points is accomplished by a phase lag technique, analogous to the periodic boundary technique discussed above, which is based on the blade positions during a full cycle of movement of domain 5 relative to domain 4. In the case of equal spacing the time-delay is zero, and the regions of non-overlap labelled "left" and "right" in Figure (A8a) have a direct correspondence. On the other hand, in the case of fractional (non-integer) spacing the matching of conditions along the region of non-overlap must be based on a correspondence of relative blade positions, which introduces a phase lag in the application of data on the interface between domains 4 and 5.

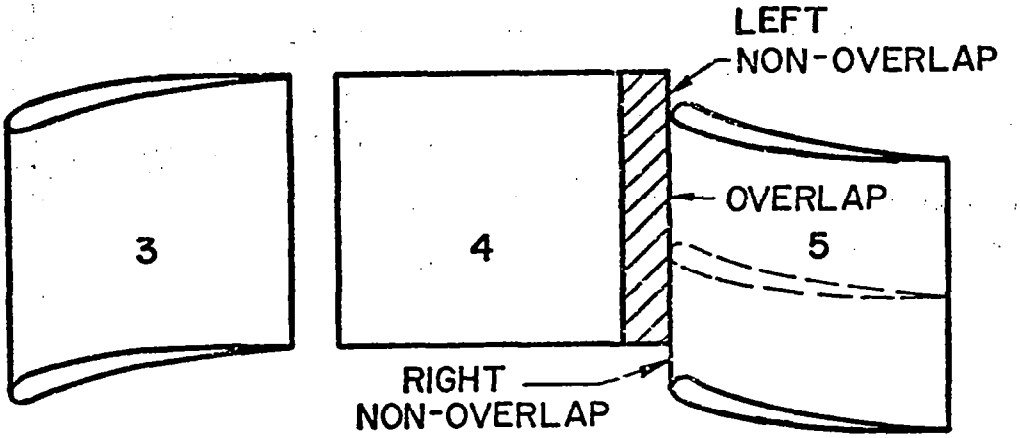

(a) Integer Multiple Domains (—1:1, ---2:1)

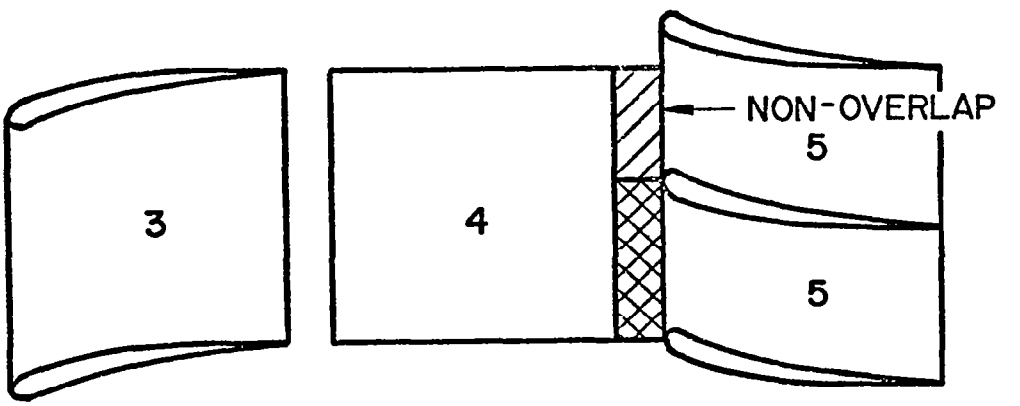

(b) Fractional Multiple Domains ($1:1 \leq N_2/N_1 < 3:2$)

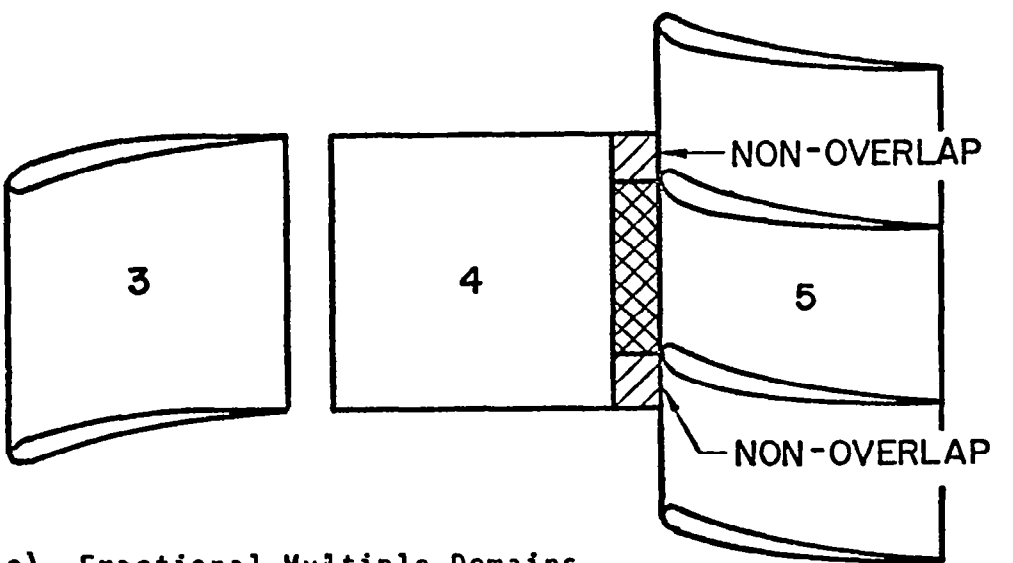

(c) Fractional Multiple Domains
(at Later Time)

FIGURE A8. VERTICAL BOUNDARIES BETWEEN DOMAINS 4 AND 5.

This phase is analogous to that discussed earlier for the horizontal boundaries. The only added feature is that up to three separate sets of data each with its appropriate phase shift must be applied since the overlap can be such as shown in Figure (A8c) which clearly shows three regions where data must be provided. Thus the J=JS values for domain 4, refer to Figure (A7), are equal to the J=2 values of domain 5 at times having up to three different phase shifts, as discussed earlier, and the J=1 values for domain 5 are equal to the J=JS-1 values for domain 4 at times having up to two different phase shifts. Even though only two are needed, three are specified since the non-overlap region can be either above or below the larger blade gap. The interpolation merely ignores the extra data.

TABLE A1

EQUIVALENT VERTICAL BOUNDARIES, WITH AND WITHOUT PHASE LAG

DOMAIN AND J INDEX (Exterior)		DOMAIN AND J INDEX (Interior)	COMMENTS
1 (JS)	=	2(2)	Only if Domain 1 is active
2 (1)	=	Interpolated between 1(JS-1) and 1(JS)	Only if Domain 1 is active
2 (JS)	=	3(2)	
3 (1)	=	2(JS-1)	
3 (JS+1)	=	Interpolated from Domain 4 6(3)	Two blade rows One blade row
4 (2)	=	3(JS)	Only if Domain 4 is active (i.e., two blade rows).
4 (JS)	=	5(2)	Interpolated with or without phase lag (IBLEQ=0 or 1), only if Domain 4 is active.
5 (1)	=	Interpolated from Domain 4	Interpolated with or without phase lag (IBLEQ=0 or 1), only if Domain 5 is active.
5 (JS+1)	=	6(3)	Only if Domain 5 is active (i.e., two blade rows)
6 (2)	=	5(JS)	
6 (JS+1)	=	Interpolated between 7(2) and 7(3)	Only if Domain 7 is active
7 (2)	=	6(JS)	Only if Domain 7 is active

REFERENCES

1. Gostelow, J. P., "Review of Compressible Flow Theories for Airfoil Cascades," Trans. ASME, J. Eng. for Power, pp. 281-292, October 1973.

2. Murman, E. M. and Cole, J. D., "Calculation of Plane Steady Transonic Flows," AIAA J, 9, 1, pp. 114-121, January 1971.

3. Gopalakrishnan, S. and Bozzola, S., "A Numerical Technique for the Calculation of Transonic Flows in Turbomachinery Cascades," ASME Paper No. 71-GT-42, 1971.

4. Oliver, D. A. and Sparis, P., "A Computational Study of Three-Dimensional Transonic Shear Flow in Turbomachinery Cascades," AIAA Paper No. 71-83, 1971.

5. Baily, F. R. and Steger, J. L., "Relaxation Techniques for Three-Dimensional Transonic Flow about Wings," AIAA J, 11, 3, pp. 318-325, March 1973.

6. Okurounmu, O. and McCune, J. E., "Three-Dimensional Vortex Theory of Axial Compressor Blade Rows at Subsonic and Transonic Speeds," AIAA J, 8, 7, pp. 1275-1283, July 1970.

7. Osborne, C., "Compressible Unsteady Interactions between Blade Rows," AIAA J, 11, 3, pp. 340-346, March 1973.

8. Kurosaka, M., "On the Unsteady Supersonic Cascade with a Subsonic Leading Edge - An Exact First Order Theory," Trans. ASME, J. Eng. for Power, pp. 13-31, January 1974.

9. Ehlers, F. E., "A Finite-Difference Method for the Solution of the Transonic Flow around Harmonically Oscillating Wings," AIAA Paper No. 74-543, 1974.

10. Alzner, E. and Erdos, J., "Unsteady Flow through Compressor Stages," NASA CR 127765, December 1971.

11. Slutsky, S., "Discrete Noise Generation and Propagation by a Fan Engine," Proceedings, AFOSR-UTIAS Symposium on Aerodynamic Noise, University of Toronto Press, pp. 20-21, May 1968.

12. Vavra, M. H., Aerothermodynamics and Flow in Turbomachines, Chapter 12 and Appendix A3, John Wiley & Sons, Inc., N.Y., 1960.

13. MacCormack, R. W., "The Effect of Viscosity on Hypervelocity Impact Cratering," AIAA Paper No. 69-534 (1969).

14. MacCormack, R. W., "Numerical Solution of the Interaction of a Shock Wave with a Laminar Boundary Layer," Proc. 2nd - Int'l. Conf. on Numerical Methods in Fluid Dynamics, M. Holt (Ed.) Springer-Verlag, N.Y. (1971).

15. Schlicting, H., Boundary Layer Theory, Fourth Edition, McGraw-Hill Book Company, N.Y., (1960).

16. Falkner, V. M. and Skan, S. W., "Some Approximate Solutions of the Boundary Layer Equations," Phil. Mag. Vol. 12, p. 865 1931; ARC R&M 1314 (1930).

17. Hartree, D. R., "On an Equation Occurring in Falkner and Skan's Approximate Treatment of the Equations of the Boundary Layer," Cambridge Phil. Soc., Vol. 33, Pt. 2, pp. 223-239, April 1937.

18. Pretsch, J., Die Stabilität einer ebenen Laminarströmung bei Druckgefälle und Druckanstieg, Jb. d. dt. Luftfahrtforschung I., 58 (1941).

19. Nikuradse, J., Gesetzmä Bigkeit der turbulenten Strömung in glatten Rohren. Forschungsheft 356 (1932) also Strömungsgesetze in rauhen Rohren. Forschungsheft 361 (1933).

20. Kemp, N. and Sears, W., "The Unsteady Forces Due to Viscous Wakes in Turbomachines," J. Aero. Sci., pp. 478-482, July 1955.

21. Dorodnitsyn, A. A., "General Method of Integral Relations and its Application to Boundary Layer Theory," in Advances in Aeronautical Sciences, Vol. 3, MacMilland and Co., N.Y. (1962).

22. Ting, L. and Libby, A., "Remarks on the Eddy Viscosity in Compressible Mixing Flows," J. Aero. Sci., 27, pp. 797-798, (1960).

23. Townsend, A. A., "The Structure of Turbulent Shear Flow," Chapter 7, Cambridge University Press, Cambridge, England (1956).

24. Coles, D., "The Law of the Wake in the Turbulent Boundary Layer," J. Fluid Mech., 1 Pt. 2, pp. 191-227, July 1956.

25. Baronti, P. and Libby, P., "Velocity Profiles in Turbulent Compressible Boundary Layers," AIAA J, 4, 2, pp. 193-201, February 1966.

26. Alzner, E. and Kalben, P., "Computation of Unsteady Transonic Flows through Rotating and Stationary Cascades - Vol. II User's Guide to Fortran Program B2DATL," NASA CR-2901, 1977.

27. Bilwakesh, K. R., Koch, C. C. and Prince D. C., "Evaluation of Range and Distortion Tolerance for High Mach Number Transonic Fan Stages," NASA CR-72880, June 1972.

28. Wuerker, R. F., Kobayashi, R. J., Heflinger, L. O. and Ware, T. C., "Application of Holography to Flow Visualization within Rotating Compressor Blade Row," NASA CR-121264, February 1974.

29. Katsanis, T. and McNally, W. D., "Revised Fortran Program for Calculating Velocities and Streamlines on the Hub-Shroud Midchannel Stream Surface of an Axial-, Radial-, or Mixed-Flow Turbomachine or Annular Duct," NASA TN D-8430, March 1977.

30. Katsanis, T., "Fortran Program for Calculating Transonic Velocities on a Blade-to-Blade Stream Surface of a Turbomachine," NASA TN D-5427, 1969.

1. Report No.	2. Government Accession No.	3. Recipient's Catalog No.
NASA CR-2900		

4. Title and Subtitle	5. Report Date
COMPUTATION OF UNSTEADY TRANSONIC FLOWS THROUGH ROTATING AND STATIONARY CASCADES I - METHOD OF ANALYSIS	December 1977
	6. Performing Organization Code
7. Author(s) John I. Erdos and Edgar Alzner	8. Performing Organization Report No. ATL TR 205 - Vol. I
	10. Work Unit No.
9. Performing Organization Name and Address Advanced Technology Laboratories, Inc. Merrick and Stewart Avenues Westbury, New York 11590	11. Contract or Grant No. NAS3-16807
12. Sponsoring Agency Name and Address National Aeronautics and Space Administration Washington, D.C. 20546	13. Type of Report and Period Covered Contractor Report
	14. Sponsoring Agency Code

15. Supplementary Notes

Final report. Project Manager, William D. McNally, Fluid System Components Division, NASA Lewis Research Center, Cleveland, Ohio 44135

16. Abstract

The report describes a numerical method of solution of the inviscid, compressible, two-dimensional unsteady flow on a blade-to-blade stream surface through a stage (rotor and stator) or a single blade row of an axial flow compressor or fan. A cyclic procedure has been developed for representation of adjacent blade-to-blade passages which asymptotically achieves the correct phase between all passages of a stage. A shock-capturing finite-difference method is employed in the interior of the passage, and a method-of-characteristics technique is used at the boundaries. The blade slipstreams form two of the passage boundaries and are treated as moving contact surfaces capable of supporting jumps in entropy and tangential velocity. The Kutta condition is imposed by requiring the slipstreams to originate at the trailing edges, which are assumed to be sharp. Results are presented for several transonic fan rotors and compared with available experimental data, consisting of holographic observations of shock structure and pressure contour maps. A subcritical stator solution is also compared with results from a relaxation method. Finally, a periodic solution for a stage consisting of 44 rotor blades and 46 stator blades is discussed.

17. Key Words (Suggested by Author(s))	18. Distribution Statement
Unsteady aerodynamics; Internal flows; Rotating machinery analysis; Computational fluid dynamics	Unclassified - unlimited STAR Category 02

19. Security Classif. (of this report)	20. Security Classif. (of this page)	21. No. of Pages	22. Price*
Unclassified	Unclassified	129	A07

* For sale by the National Technical Information Service, Springfield, Virginia 22161

*U.S. GOVERNMENT PRINTING OFFICE: 1977 - 735-078/63